Astron Astrophys Rev (2016) 24:15
DOI 10.1007/s00159-016-0099-5

REVIEW ARTICLE

Mars: a small terrestrial planet

N. Mangold[1] · D. Baratoux[2,3] · O. Witasse[4] · T. Encrenaz[5] · C. Sotin[1,6]

Received: 29 June 2016 / Published online: 16 November 2016

Abstract Mars is characterized by geological landforms familiar to terrestrial geologists. It has a tenuous atmosphere that evolved differently from that of Earth and Venus and a differentiated inner structure. Our knowledge of the structure and evolution of Mars has strongly improved thanks to a huge amount of data of various types (visible and infrared imagery, altimetry, radar, chemistry, etc) acquired by a dozen of missions over the last two decades. In situ data have provided ground truth for remote-sensing data and have opened a new era in the study of Mars geology. While large sections of Mars science have made progress and new topics have emerged, a major question in Mars exploration—the possibility of past or present life—is still unsolved. Without entering into the debate around the presence of life traces, our review develops various topics of Mars science to help the search of life on Mars, building on the most recent discoveries, going from the exosphere to the interior structure, from the magmatic evolution to the currently active processes, including the fate of volatiles and especially liquid water.

Keywords Mars · Geological evolution · Geophysics · Atmosphere

✉ N. Mangold
nicolas.mangold@univ-nantes.fr

1 Laboratoire Planétologie Géodynamique, CNRS and Université de Nantes, 2 rue de la Houssinière, 44322 Nantes, France

2 Geosciences Environnement Toulouse, Université de Toulouse, CNRS and IRD, UMR 5563, 14 Avenue Edouard Belin, 31400 Toulouse, France

3 Institut Fondamental d'Afrique Noire Check Anta Diop, Dakar, Senegal

4 European Space Agency, Science Support Office, 2200 AG Noordwijk, The Netherlands

5 Observatoire Paris-Site de Meudon LESIA 5 Pl Jules Janssen, 92195 Meudon, France

6 NASA/JPL, Pasadena, USA

Contents

1 Introduction

Mars is one of the inner planets, belonging to the family of terrestrial, rock-dominated planets. By being smaller and farther away from the sun, Mars is characterized by a cold, tenuous atmosphere that evolved differently from that of Earth and Venus. Our knowledge of the geological evolution of Mars has strongly improved thanks to the NASA Mars Program and the ESA Mars Express mission in the last two decades. All together, five orbiter missions, four rovers, and one lander (Fig. 1) have acquired a tremendous amount of data of various types (visible and infrared imagery, altimetry, radar, chemistry, etc.). While these data are still under investigation, large sections of Mars science have made progress and new topics have emerged. The present atmospheric composition and H_2O and CO_2 cycles are now well understood. Multiple pieces of geological evidence indicate that its ancient climate was different than its present one with liquid water flowing at the surface, at least episodically. The surface composition and physical properties (mineralogy, chemistry, thermal inertia, and density) have been mapped in great detail by remote-sensing instruments that reveal a diversity of processes close to that observed on Earth. The morphology of the major geological features has been characterized from low- to high-resolution images and topography. In situ data have provided ground truth for remote-sensing data and have opened a new era in Mars surface geology analysis. In parallel, many new martian meteorites have been collected on Earth providing inputs complementary to the space missions.

However, a main goal in Mars exploration is still unsolved: the possibility of past life on Mars has been suggested from the evidence of liquid water 3.5 Gy ago, a period during which life emerged on Earth. As on Earth, ancient sediments may have

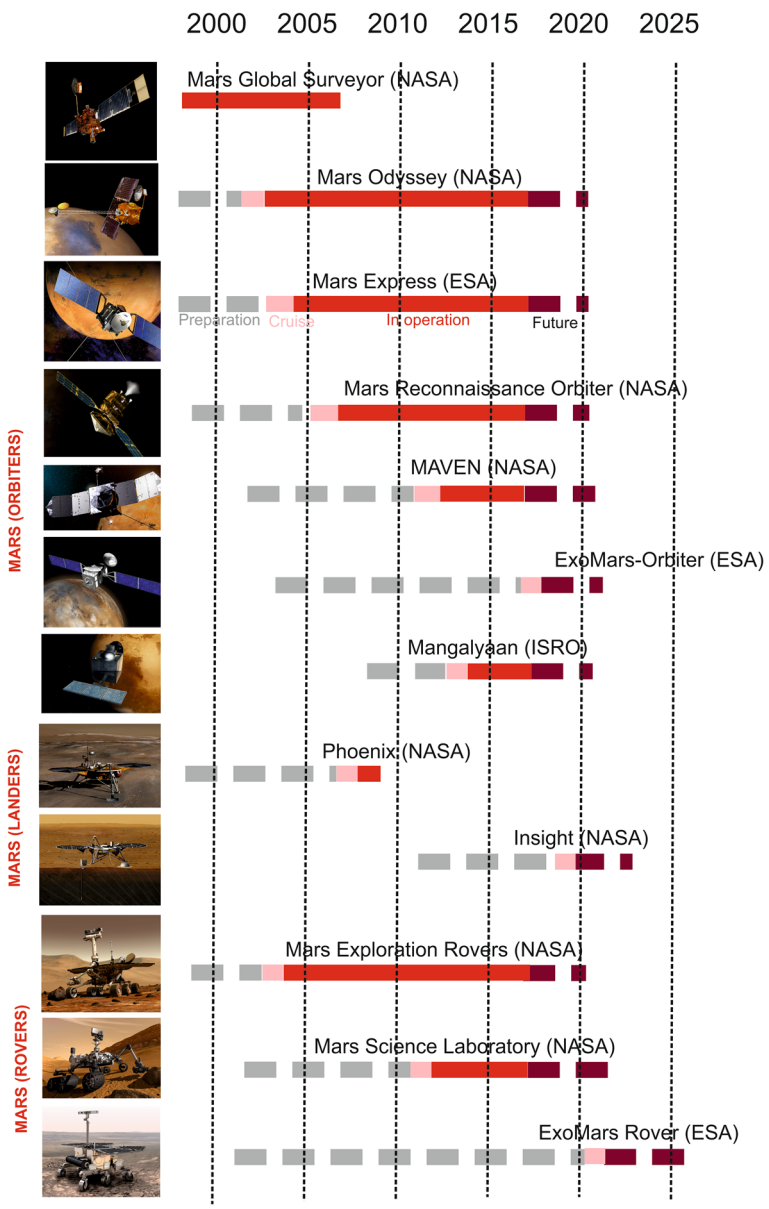

Fig. 1 Orbital and landed missions to Mars in the last two decades (image credits from NASA, ESA, and ISRO)

recorded any possible biological activity in this period. The Curiosity rover has provided evidence for aqueous conditions, past habitability (Grotzinger et al. 2014, 2015; McLennan et al. 2014), and the presence of organics (Fressinet et al. 2015), but the question of the emergence of life remains unsolved. In contrast, the preservation of life

until present time is a more tenuous possibility, given cold temperatures, lack of liquid water, and exposure to UV radiation. However, recent findings (methane detection, putative liquid flows on seasonally warm slopes) re-opened the debate. While exobiology is a central objective of most martian missions, our review does not develop this topic, but aims to set up the context for future exobiological studies by presenting the state-of-the-art of geological, geochemical, geophysical, and atmospheric observations and modeling.

The growing body of literature in Mars research is enabled by the wealth of data that has been provided by recent space missions. A consequence is that the Mars scientific community is becoming increasingly specialized in particular research areas, evidenced by the rising frequency of topical conferences and workshops (e.g., regarding polar caps, eolian landforms, impact craters, recent gullies, etc). However, it is important to place new datasets and findings in a global context that spans Mars' ancient past to its present, to develop our understanding of Mars' evolution and present state as a whole. Thus, our review also aims to emphasize what has changed in the understanding of Mars' evolution in the last decade to provide guidance for scientists interested in this terrestrial planet.

In this synthesis, we first start with a detailed description of the present structure and composition of Mars atmosphere, surface, and interior (Sect. 2), before presenting the current knowledge of its geological (Sect. 3) and climatic evolution (Sect. 4). While all Mars missions have improved our understanding of Mars' evolution, they have also triggered new questions, so we conclude the review by summarizing pertinent remaining questions and suggesting future missions that may help to answer them (Sect. 5).

2 Present composition and structure

2.1 The lower atmosphere

Our knowledge of the lower atmosphere's composition and thermal structure goes back to the 1970s, when two most successful space missions provided us with datasets that are still of use today. The Mariner 9 orbiter, in operation in 1972, revealed Mars' volcanoes and main surface features, but also measured, through its infrared spectroscopic measurements, the surface pressure and the thermal profile (through CO_2 absorption bands) and the abundance of the main minor species (H_2O, CO) as a function of the seasonal cycle. The Viking missions, comprising two orbiters and two landers, produced datasets with unprecedented coverage of Mars' seasons, both in situ and from space, which elucidated the variability in temperature and pressure, and allowed us to observe the martian water vapor cycle.

2.1.1 Thermal structure and dynamics

Datasets

The thermal atmospheric structure of Mars is best retrieved from the inversion of the strong $CO_2 \upsilon 2$ band occurring at 15 μm in Mars' thermal spectrum (Fig. 2). This

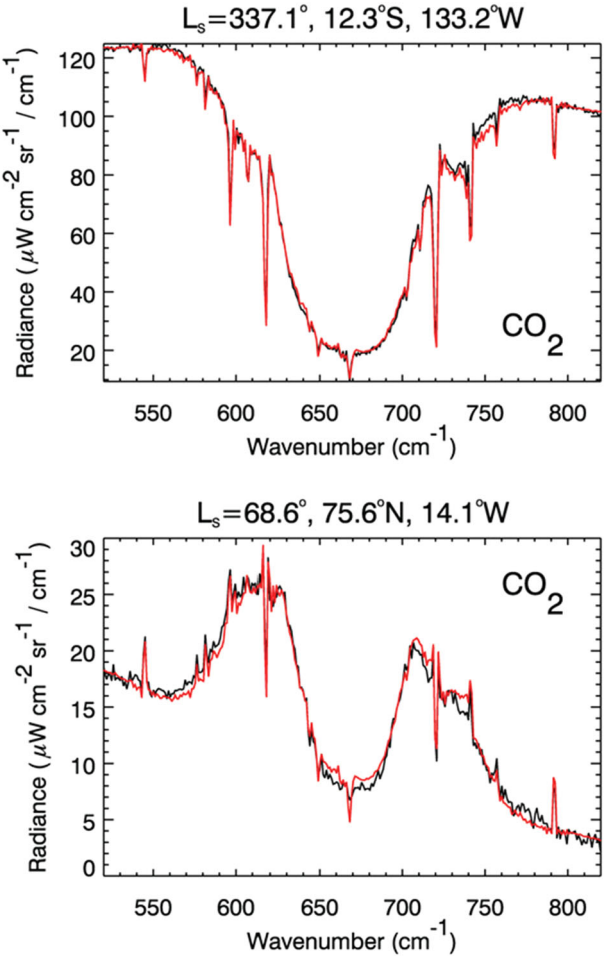

Fig. 2 Infrared spectrum of Mars in the 15-μm CO_2 band. *Top* mid-latitudes; *bottom* high-latitudes, above the polar ice cap. The figure is taken from Fouchet et al. (2007)

method was first used with the InfraRed Imaging Spectrometer (IRIS) instrument aboard Mariner 9 (Hanel et al. 1972), then with the InfraRed Thermal Mapper (IRTM) aboard the Viking orbiters (Martin 1981), which both observed in the nadir mode. In addition, local seasonal variations of the surface pressure were measured by the Viking landers over several Martian years. After the Viking mission, the next important milestone was, in 1999, the infrared dataset recorded by the Thermal Emission Spectrometer (TES) aboard the Mars Global Surveyor (MGS) mission. In addition to nadir measurements, used to study both the surface mineralogy (Christensen et al. 2001) and the thermal structure of the lower atmosphere (Conrath et al. 2000), TES acquired limb data that were used to retrieve the thermal structure up to about 65 km (Smith 2002). The thermal mapping with TES covered almost 3 Martian years (Smith 2004). Later, new atmospheric datasets were obtained with the Thermal Emission Imaging

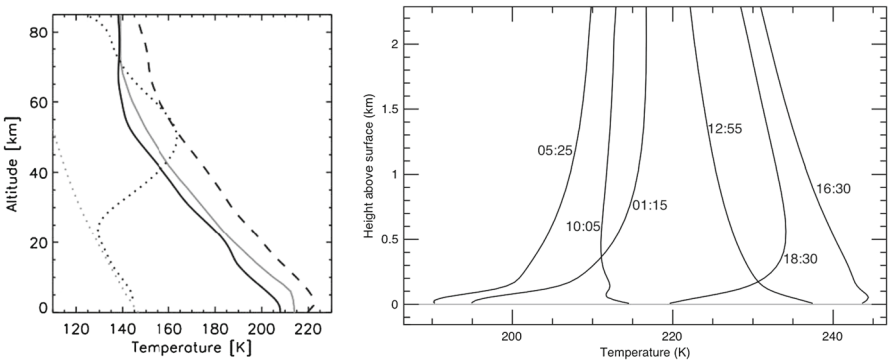

Fig. 3 *Left* averaged temperature profiles as observed by the Mars Reconnaissance Orbiter MCS instrument. The *solid black line* is for the aphelion (Ls = 0°–180°) season. The *dashed line* is for the perihelion (Ls = 180°–360°) season. The *black dotted line* is for conditions during polar night. The *solid grey line* shows the COSPAR reference atmosphere (Seiff 1982) and the *grey dotted line* shows the CO_2 condensation curve. The figure is taken from Smith et al. (2016). *Right* near-surface atmospheric temperatures as a function of height above the surface for different times of day as retrieved from upward-looking observations taken by the Mini-TES instrument onboard the *Spirit* MER rover. The figure is taken from Smith et al. (2016)

System (THEMIS) instrument aboard Mars Odyssey (Christensen et al. 2001), then with Planetary Fourier Spectrometer (PFS) aboard Mars Express (Grassi et al. 2005, 2007). Finally, the Mars Climate Sounder (MCS) aboard the Mars Reconnaissance Orbiter (MRO) mission observed the Martian atmosphere and surface using limb, nadir, and off-nadir geometries, allowing a retrieval of the thermal structure up to an altitude of about 85 km over all seasons (McCleese et al. 2007, 2008).

Information about the thermal structure can also be retrieved from the occultation technique, using either radio signals sent by the spacecraft through the atmosphere or the signal of a star disappearing or reappearing from behind the planet's limb. The first method has been used by all spacecraft since Mariner 9 (Kliore et al. 1973; Lindal et al. 1979; Hinson et al. 1999; Pätzold et al. 2009), and probes the lower atmosphere from the surface to about 45 km. The second method has been used in the UV range by the SPICAM instrument aboard Mars Express and gives information on the upper atmosphere, above about 100 km (Forget et al. 2009).

The thermal structure of the lower atmosphere

Two factors are important to understand the variability of the thermal structure with latitude and season: the obliquity (25°) and the orbital eccentricity (0.0934). The relatively high eccentricity causes an increase of the solar flux by about 40% at perihelion (which, presently, is close to southern summer solstice) as compared with aphelion (close to northern summer solstice). This results in an asymmetry between the two hemispheres and higher temperatures near southern summer solstice (Ls = 270°). Figure 3 (left) shows typical thermal profiles retrieved by the MCS instrument aboard MRO, at aphelion and perihelion. The thermal profile is convective, constrained by the surface temperature. As the surface reacts to solar radiation faster than the atmosphere, a temperature inversion usually occurs in the first 500 m near sunrise and sunset. The atmosphere is, indeed, coolest at night. Soon after sunrise, the surface, heated by solar

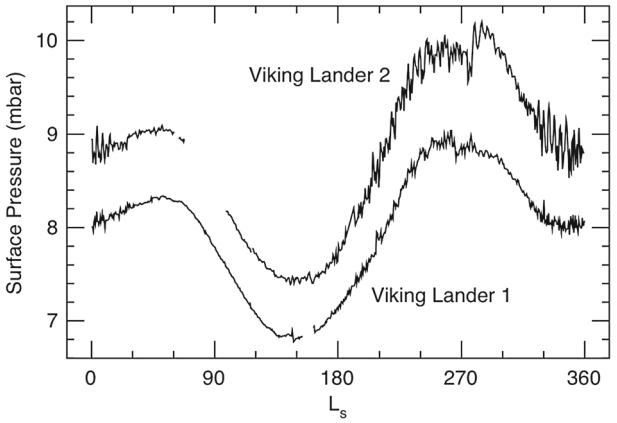

Fig. 4 Daily averages of surface pressures (mbars) as recorded by the two Viking landers spacecrafts during the first martian year of operation. The figure is taken from Smith et al. (2016)

radiation, heats the lower atmosphere from the bottom upward, creating a very steep, and superadiabatic gradient just above the surface. In the late afternoon, the surface cools down faster than the atmosphere and the near-surface temperature gradient is inverted (Smith et al. 2016; Fig. 3, right).

Seasonal variations of the surface pressure

Estimates of the disk-averaged surface pressure have been known since the 1960s using ground-based infrared spectroscopy of CO_2 (Kaplan et al. 1969). From the measurement of the Lorentz broadening of the CO_2 lines, they inferred a surface pressure of 25 ± 15 hPa, implying that carbon dioxide is the major atmospheric constituent. Later, an accurate in situ seasonal monitoring of the surface pressure was achieved at the two sites of the Viking landers over 3 Martian years (Tillman et al. 1993, Fig. 4). The difference between the measurements of Viking 1 and 2 reflects the altitude difference between the two sites. The seasonal variations reflect the condensation of CO_2 in seasonal polar caps at the winter poles: over the martian cycle, the surface pressure decreases at the winter pole and increases again at the summer pole with a total variation amplitude of about 30%. The difference in timing and amplitude between the maxima and minima is an effect of the orbital eccentricity: it reflects the relative phasing of the seasons with respect to the aphelion and perihelion dates (Smith et al. 2016). In addition, the albedo and the emissivity of the seasonal polar cap also play a role (Paige and Wood 1991).

Because hemispheric temperature contrasts are largest near perihelion (between southern spring and summer), strong winds are generated at that time, leading to local or even global storms. Dust is uplifted from the surface and carried as high as 50 km at speeds of up to 100 m s^{-1}. The dust opacity can be monitored through its infrared signature around 10 μm, as was done with the TES instrument (Smith 2004, Fig. 5). At that time, diurnal or semi-diurnal solar thermal tides (increase of surface pressure and thermal expansion of the atmosphere in response to heating) can be observed, as at the Viking 2 lander site at Ls = 279° (Zurek 1981). These storms also induce

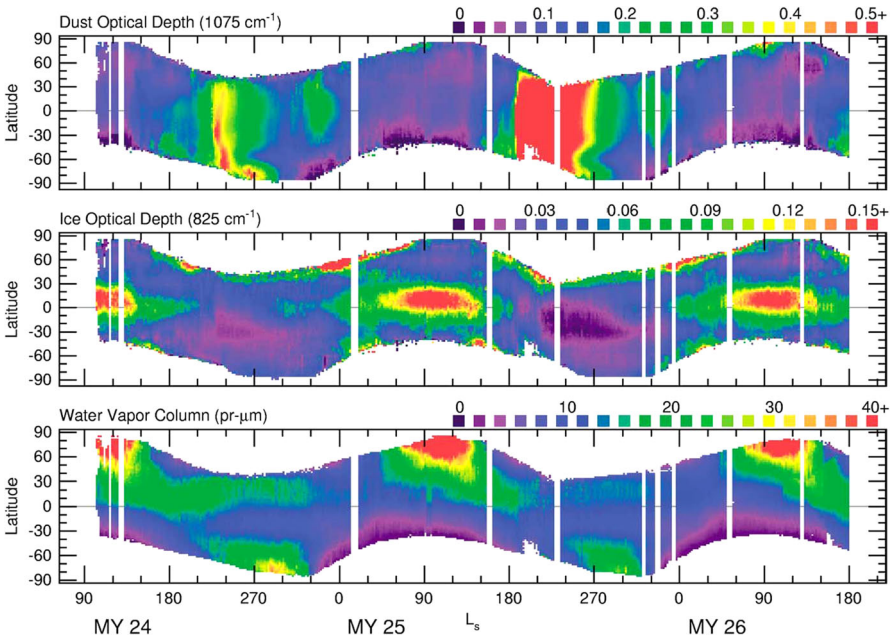

Fig. 5 Evolution of dust optical depth (*top*), water ice (*middle*), and water vapor (*bottom*) as a function of the solar longitude Ls. The figure is taken from Smith (2004)

strong anomalies in the temperature field, as their effect is to make the thermal profile warmer and closer to isothermal over the whole lower atmosphere.

Since 2012, the Rover Environmental Monitoring Station (REMS) aboard Curiosity Gómez-Elvira et al. (2012) has been continuously monitoring the air and ground temperature, pressure, relative humidity, and wind speed. Simultaneous measurements of these parameters were achieved routinely, including during nighttime. In addition, UV solar radiation was monitored in different spectral bands (Martin-Torres et al. 2015a). New results have been obtained on the daily pressure variations and their relation to topographic changes in Gale crater; the sun-synchronous thermal tide (generated by the interaction of the dayside atmosphere with the solar radiation), previously observed by the Viking landers, was monitored by REMS as function of the Sun–Mars distance. Katabatic winds induced by strong topographic variations were observed in the nighttime. Atmospheric ozone was also monitored using the UV sensor. Once completed, the REMS dataset will be a major reference to be used in comparison with data from Viking, thus allowing a variability study of the atmospheric parameters over four decades.

Atmospheric circulation and dynamics

The global circulation of the Martian atmosphere follows the classical Hadley scheme with one single Hadley cell rising in the summer hemisphere and a single subsiding cell in the opposite hemisphere. In contrast with the terrestrial circulation, Hadley cells on Mars can develop and rise up to an altitude above 60 km, i.e., much higher than is observed on Earth, where the convective zone is limited to the tropopause at an altitude

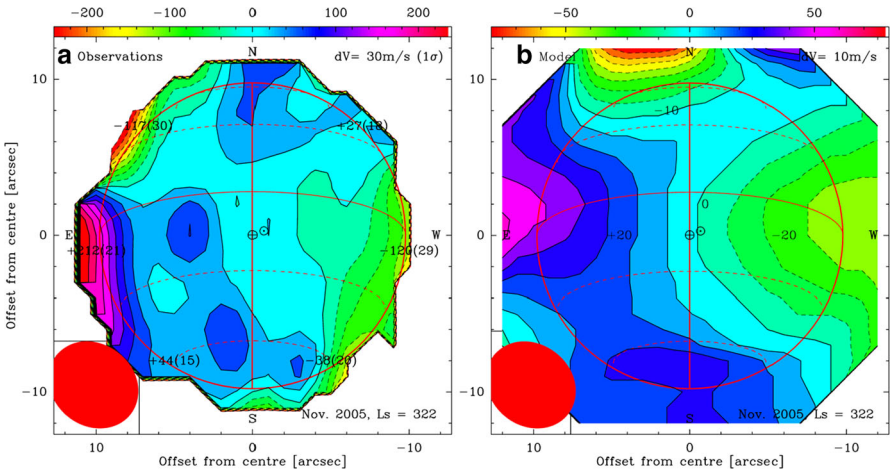

Fig. 6 Maps of mesospheric winds on Mars as measured from millimeter observations at the IRAM Plateau de Bure interferometer. Data were recorded in November 2005 (Southern summer, Ls = 322°). The figure is taken from Moreno et al. (2009)

of about 12 km. This simple scheme reflects the fact that Mars' atmosphere is very tenuous and responds quickly to changes in the incoming solar flux. This behavior is well reproduced by GCMs up to an altitude of about 50 km. Winds at altitudes $\lesssim$50 km can be measured using the heterodyne technique at radio wavelengths, i.e., measuring the Doppler shift of CO transitions in the millimeter range. Using different emission lines of ^{12}CO and its isotope ^{13}CO over millimeter and sub-millimeter wavelengths allows us to probe different atmospheric pressure levels. Using networks of antennas for interferometry, it is possible to map wind fields at different altitudes between 40 and 70 km. The agreement with the GCM is usually satisfactory (Fig. 6). The main zonal circulation is dominated by strong retrograde winds, with velocities ranging between 70 and 170 m s^{-1}, varying with latitude, season, and local time (Moreno et al. 2009).

2.1.2 Atmospheric composition

Ground-based, orbital, and in situ data have progressively improved our knowledge of the atmospheric composition of Mars. The abundances of minor species are listed in Table 1.

Detection of H_2O and variability in abundance

Our understanding of the water cycle on Mars is based on a series of remote-sensing campaigns, achieved first from ground-based telescopes and later from orbiting spacecraft. Since 2012, the relative humidity sensor of the REMS suite aboard Curiosity has been monitoring the water content at the rover site (Martín-Torres et al. 2015b). The first REMS measurements at Gale Crater show evidence for the formation of night-time transient liquid brines in the first 5 cm below the surface which evaporate after sunrise. Changes in the hydration state of salts under the surface also indicate an active atmosphere–surface interaction (Martín-Torres et al. 2015b). This new dataset

Table 1 Composition of the Martian atmosphere

Molecule	Abundance	Method of detection	References
CO_2	95.32%	Viking mass spectrometry	Owen et al. (1977)
CO	0.8%	Ground-based IR & mm spectroscopy, SAM/Curiosity mass spectrometry	Smith et al. (2009), Franz et al. 2015
H_2O	15–1500 ppmv	In-orbit IR spectroscopy	Smith (2004)
N_2	2.7%	SAM Curiosity mass spectrometry	Franz et al. (2015)
^{40}Ar	1.6%	SAM Curiosity mass spectrometry	Franz et al. (2015)
$^{36,38}Ar$	5.3 ppmv	Viking mass spectrometry	Owen et al. (1977)
Ne	2.5 ppmv	Viking mass spectrometry	Owen et al. (1977)
Kr	0.3 ppmv	Viking mass spectrometry	Owen et al. (1977)
Xe	0.08 ppmv	Viking mass spectrometry	Owen et al. (1977)
O_2	0.14%	Ground-based visible + SAM/curiosity mass spectrometry + sub-mm spectroscopy	Hartogh et al. (2010), Franz et al. (2015)
O_3	10–350 ppbv	In-orbit UV spectroscopy	Perrier et al. (2006)
H_2O_2	10–40 ppbv	Ground-based IR and sub-mm spectroscopy	Encrenaz et al. (2015b)
CH_4	0–30 ppbv 0.7 ppbv (background) + 7 ppbv (transient source)	Ground-based IR spectroscopy SAM/curiosity mass spectrometry	Mumma et al. (2009), Webster et al. (2015)

will bring important information on the local H_2O variability and its association with day-night effects and topography.

Water vapor was first detected from Earth at visible wavelengths (0.82 μm, Spinrad and Richardson 1963). Ground-based H_2O and HDO observations followed in the visible (Sprague et al. 1996, 2006) and near-infrared (NIR) (Barker 1972, 1976), in the thermal infrared (Encrenaz et al. 2005) and millimeter/sub-millimeter range (Clancy et al. 1992; Encrenaz et al. 1991; Gurwell et al. 2000, 2005). Water vapor was also detected in far-infrared observations by IRIS aboard Mariner 9 (Hanel et al. 1972), from ground-based IR data (Barker 1976) and in the NIR range with the MAWD experiment aboard the Viking orbiters (Farmer et al. 1977). The data were used to build an understanding of the water vapor cycle on Mars, which is largely governed by water condensation in the polar caps at each polar winter. Due to the orbital eccentricity, the maximum water vapor abundance at the north pole, at northern summer solstice, is significantly more pronounced that its equivalent at the south pole.

In-orbit monitoring of water vapor with IRIS on Mariner 9 and MAWD on Viking has led to the first analysis of the seasonal water cycle on Mars (Jakosky and Haberle 1992). This work was later refined by the TES analysis aboard MGS (Smith 2002, 2004, Fig. 5). Ground-based heterodyne spectroscopy measurements of HDO in the millimeter range (Encrenaz et al. 1991) and H_2O at 22 GHz (Clancy et al. 1992) were

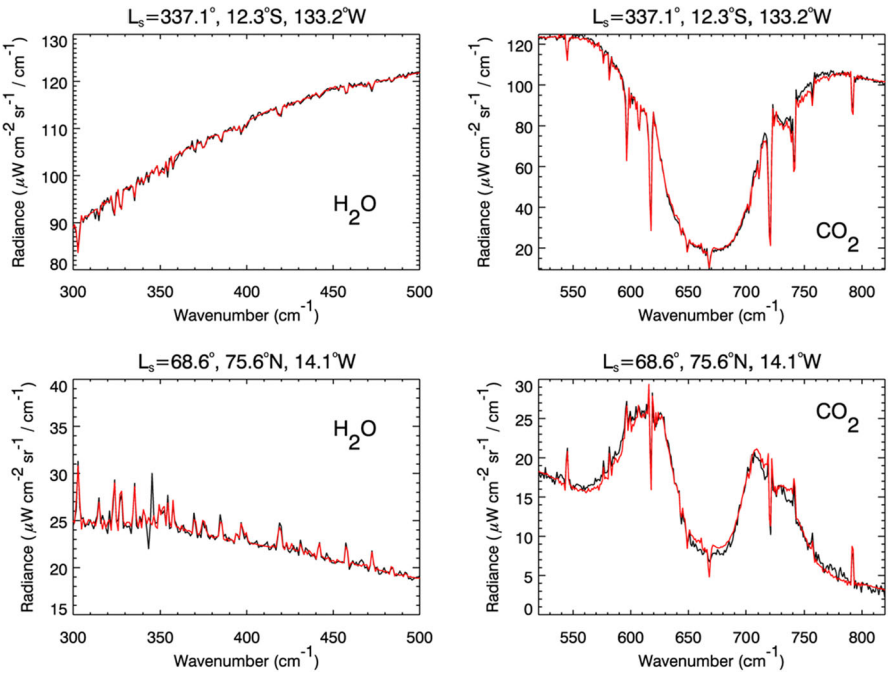

Fig. 7 Examples of retrievals of the thermal structure and the water vapor content in two different regions of Mars, using the long-wavelength channel of the PFS instrument aboard Mars Express. The figure is taken from Fouchet et al. (2007)

used to infer the vertical distribution of water vapor, which condenses at low altitudes near aphelion (Clancy et al. 1996).

Rotational water lines in IRIS/Mariner 9 spectra were first used to retrieve variations of the water vapor content at the North Pole during northern spring (Conrath et al. 1973). The first systematic coverage of the water vapor content as a function of latitude and season was obtained by the Mars Atmospheric Water Detector (MAWD) instrument aboard the two Viking orbiters, from a study of the near-infrared H_2O band at 1.38 μm (Farmer et al. 1977). These data demonstrated the existence of a water cycle driven by sublimation of the north polar cap around the northern summer solstice. These data also explained the asymmetry between the two hemispheres induced by the presence of a permanent CO_2 polar cap at the South Pole, preventing the complete water sublimation near southern summer solstice (Jakosky and Haberle 1992). The next major milestone came with the Thermal Emission Spectrometer instrument aboard the MGS orbiter, which monitored the water vapor content, through its rotational lines around 20–30 μm, as a function of latitude and season for a fixed local time (14:00) over 3 martian years (Smith 2002, 2004, Fig. 5).

These datasets have been complemented with observations performed by several instruments aboard the Mars Express Orbiter: SPICAM-IR in the 1.38 μm band (Fedorova et al. 2006), OMEGA in the 2.65 μm band (Melchiorri et al. 2006), PFS in the rotational lines (Fouchet et al. 2007; Fig. 7), and in the 2.65 μm band (Tschimmel

et al. 2008). The OMEGA and PFS observations were in global agreement with the TES data, although indicating a lower maximum water content at the north pole (close to 70 pr-μm, whereas 100 pr-μm were originally reported by TES), while the water content inferred from SPICAM-IR appeared to be systematically lower. Information on the water vapor vertical distribution was also obtained by PFS. On the basis of an inverse correlation observed between the water column, normalized to a fixed pressure, and surface pressure, Fouchet et al. (2007) inferred a vertical distribution intermediate between saturation and confinement to a surface layer. Tschimmel et al. (2008) also suggested a non-uniform distribution of water with confinement in the few kilometers above the surface at high northern latitudes in summer. Such behavior was previously reported from ground-based heterodyne spectroscopy measurements of HDO that give access to the vertical water distribution (Clancy et al. 1992; Encrenaz et al. 2001).

As a complement to the TES dataset, the Mars Express data were important for observing in detail the polar caps at different local times. In addition, the SPICAM instrument aboard this mission offered new possibilities for constraining the vertical distribution of water vapor using its capability for the observation of solar occultations. The analysis of the 1.38 μm water band in the solar occultation mode demonstrated the presence of supersaturated water (ten times higher than the saturated value) around northern summer solstice at altitudes between 20 and 50 km (Maltagliati et al. 2011). At this season close to aphelion, the hygropause would be expected at about 15 km. The observed supersaturation might be due to a lack of dust nuclei, as suggested by the observed inverse correlation between the saturation ratio and the dust loading. Supersaturation may have important impacts on the present cross-hemispheric transport of water but also on the escape of water from Mars, as it allows much more water to propagate through the hygropause than previously anticipated. Note also that the surface temperature is low enough for water frost or ice clouds to condense occasionally at mid-latitudes.

The present water cycle of Mars is the result of complex interactions between surface and atmosphere, including exchanges between water vapor, ice caps, surface frost, and ice clouds. How do GCMs account for the water vapor seasonal cycle? The first 3D GCMs describing the main characteristics of the observed cycle were developed by Richardson and Wilson (2002), who included water vapor sublimation, condensation, and transport. Montmessin et al. (2004) also obtained a good agreement with the data, and analyzed in more detail the influence of water ice clouds. Following analyses by Haberle et al. (1999) and Colaprete et al. (1999), new models (Hinson and Wilson 2004; Madeleine et al. 2012) have considered the radiative effect of these clouds, which in some cases can generate temperature inversions. A further improved 3D GCM model has been developed by Navarro et al. (2014), including the nucleation on dust particles, ice particle growth in a supersaturated atmosphere, and scavenging of dust particles due to ice condensation. This study illustrates the importance of microphysics in the modeling of the water cycle. Comparison of the results of this GCM with the TES database is quite satisfactory, except for an underestimation of the water vapor content at mid-latitudes after $Ls = 180°$ and a slight overestimation of the maximum content at $Ls = 90°$ at the north pole (Fig. 8). In addition, this model is also able to predict supersaturation above the hygropause, with a good overall agreement in the Northern hemisphere (Fig. 9).

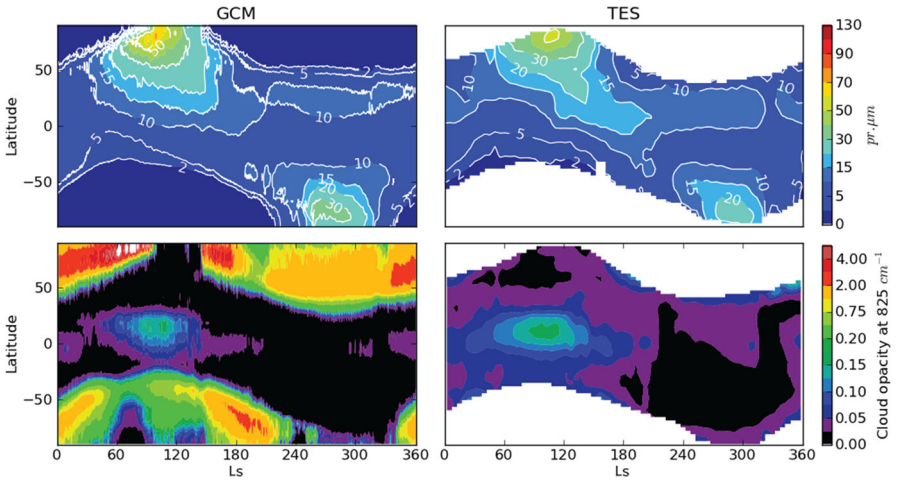

Fig. 8 Water vapor cycle of Mars as predicted by the GCM (Navarro et al. 2014) and observed by the TES instrument aboard MGS. *Top* water vapor column density; *bottom* cloud opacity. The figure is taken from Navarro et al. (2014)

Detection and abundance of CO

Among the minor atmospheric species (H_2O apart), carbon monoxide, CO, was the only one to be unambiguously detected from the ground, first through its near-infrared transitions (Kaplan et al. 1969), then in the millimeter range (Kakar et al. 1977). Since its early ground-based detection in the millimeter range, CO has been used to infer and monitor the thermal structure of Mars; the (1-0) and (2-1) lines of ^{12}CO and ^{13}CO were used to simultaneously retrieve the thermal profile and the CO mixing ratio (Clancy et al. 1996). CO has also been used as a tracer of mesospheric winds, through the measurement of the Doppler shift of CO millimetric and sub-millimetric transitions.

Because CO is a non-condensable species, its mixing ratio is expected to vary with latitude and season, despite the fact that its photochemical lifetime is longer than one martian year. Indeed, the CO_2 column density is subject to change because of the CO_2 condensation/sublimation cycle from one pole to the other, while the CO column density is not, so the CO/CO_2 mixing ratio is expected to vary with latitude and season. Using infrared spectra from OMEGA aboard Mars Express and later CRISM aboard MRO, the local seasonal variations of CO were monitored, and are in agreement with the GCM predictions (Encrenaz et al. 2006; Smith et al. 2009). Local measurements have recently been performed by the Curiosity rover in Gale crater (lat = 5.4 S, lon = 137.7 E); the inferred mixing ratio, measured for two Ls values of 175° and 193° respectively, is $7.49 \pm 0.026 \times 10^{-4}$ (Franz et al. 2015), in the range of previously reported values.

The low abundance of CO (typically less than 0.1%) has been a matter of debate over the past decade. Indeed, CO and O are formed from the photo-dissociation of CO_2

$$CO_2 + h\nu \rightarrow CO = O$$

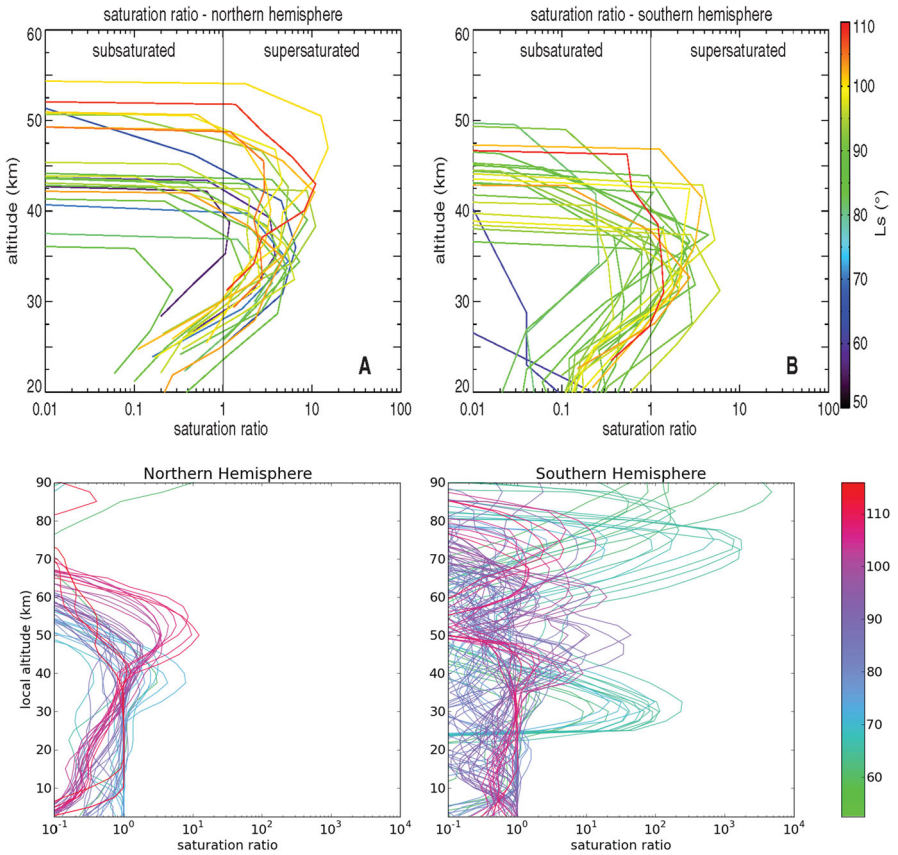

Fig. 9 Supersaturation ratios in the Martian atmosphere. *Top* observations by SPICAM-IR (Maltagliati et al. 2011). *Bottom* GCM predictions (from Navarro et al. 2014)

but the inverse reaction

$$CO + O + M \rightarrow CO_2 + M$$

is spin-forbidden. An accumulation of CO (as well as O_2) would then be expected on a timescale of a few thousand years, but is not observed. McElroy and Donahue (1972) and Parkinson and Hunten (1972) have proposed a photochemical model in which the oxidation of CO into CO_2 is achieved by OH radicals:

$$CO + OH \rightarrow CO_2 + H.$$

In the first case, the source of OH is HO_2, issued from the combination of H and O_2; in the second case, the main source of OH is H_2O_2. However, both models face difficulties. McElroy & Donahue's model requires excessively high values of the eddy diffusion coefficient, while Parkinson & Hunten's model requires too much

water vapor, about three to four times the mean observed water content. Liu and Donahue (1976) also pointed out that the recombination of CO and O into CO_2 through a water catalytic cycle would be expected to regulate the oxygen and hydrogen escape.

Heterogeneous chemistry was proposed by Atreya and Blamont (1990) to account for the recombination of CO and O into CO_2. However, subsequent laboratory measurements of CO_2 reaction rates and extinction cross sections have shown that the CO_2 production rate might exceed its destruction rate even without catalytic recombination (Atreya and Gu 1994; Rosenqvist and Chassefière 1995; Stock et al. 2011).

Detection and abundance of O_2

Oxygen was first measured from the Earth ground, from the high-resolution spectroscopy of weak transitions at 763 nm, with a mixing ratio ranging from 0.11 to 0.13% (Barker 1972; Carleton and Traub 1972). Oxygen was also detected with the mass spectrometers of the Viking landers (Owen et al. 1977). New disk-averaged measurements have been achieved with the Heterodyne Instrument for the Far Infrared (HIFI) aboard the Herschel Space Observatory, leading to a mixing ratio of 0.14% (Hartogh et al. 2010).

As O_2 is (like N_2 and CO) a non-condensable species on Mars, its mixing ratio (measured versus CO_2 which does condense) is expected to exhibit seasonal variations. Local measurements of O_2 have been obtained in the Gale crater by the SAM mass spectrometry experiment aboard the Curiosity rover, leading to a mixing ratio of 0.173 $\pm$ 0.006 % (Franz et al. 2015).

Detection of O_3

Ozone was first detected from the Mariner 9 orbiter through its UV absorption at 250 nm (Barth et al. 1972a, 1973). Later, this UV signature was monitored with the SPICAM instrument aboard Mars Express, leading to a complete monitoring of ozone with latitude and season (Perrier et al. 2006; Lefèvre et al. 2006, Fig. 10). The UV emission of ozone was also mapped with the MARCI camera aboard MRO (Clancy et al. 2010). Ozone was also observed from the ground using heterodyne spectroscopy around 10 μm (Espenak et al. 1991; Fast et al. 2006, 2009). Ozone exhibits local maxima at the winter poles and low abundances at the equinox for all latitudes. Using the solar occultation mode of SPICAM, Lebonnois et al. (2006) have retrieved the vertical profile of ozone, which exhibits two ozone layers, one below 30 km and a second one between 30 and 60 km.

Ozone has been also indirectly monitored from the measurement of the excited band of oxygen at 1.27 μm by PFS (Geminale and Formisano 2009) and OMEGA (Altieri et al. 2009) aboard Mars Express. The O_2 emission results from the O_3 dissociation and traces the O_3 content above an altitude of 25 km, as O_2 is de-excited through CO_2 collisions at lower altitudes. The general behavior of ozone, showing an inverse correlation with water vapor and a maximum reaching 30 μm—atm (8×10^{16} cm^{-2}) at the winter poles, is in agreement with early photochemical models (McElroy and Donahue 1972; Parkinson and Hunten 1972). More recently, using heterogeneous chemistry on water ice clouds, Lefèvre et al. (2008) and Krasnopolsky (2009) have improved the agreement between the models and the data.

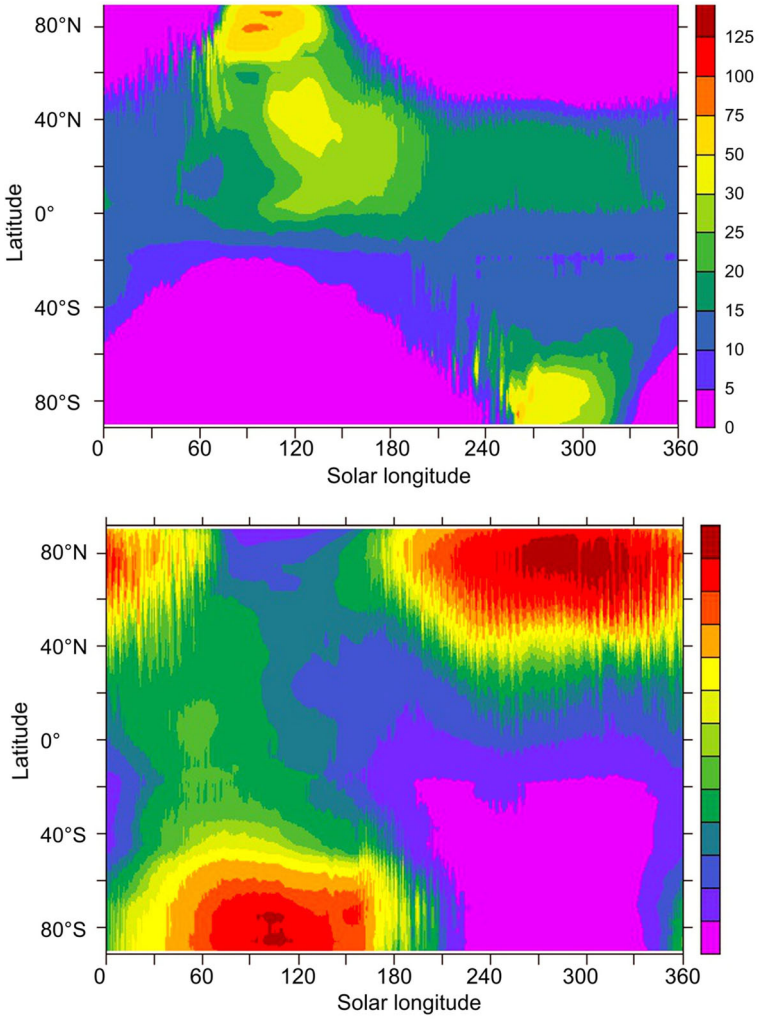

Fig. 10 *Top* zonally averaged water vapor column (pr-μm); *bottom* zonally averaged ozone vapor column (μm-atm), calculated by the GCM as a function of the solar longitude Ls. The figure is taken from Lefèvre et al. (2006)

Detection of H_2O_2

Hydrogen peroxide is an important tracer of the Martian photochemistry. It is also the putative oxidizer invoked as responsible for the apparent lack of organics at the surface of Mars (Oyama and Berdahl 1977). H_2O_2 was first detected by ground-based heterodyne spectroscopy in the sub-millimeter range (Clancy et al. 2004). It was also mapped in the thermal infrared (Encrenaz et al. 2004, Fig. 11) and its seasonal variations were subsequently monitored (Encrenaz et al. 2012, 2015b). As in the case of ozone, these seasonal variations favor photochemical models, including heterogeneous chemistry on water ice grains (Lefèvre et al. 2008).

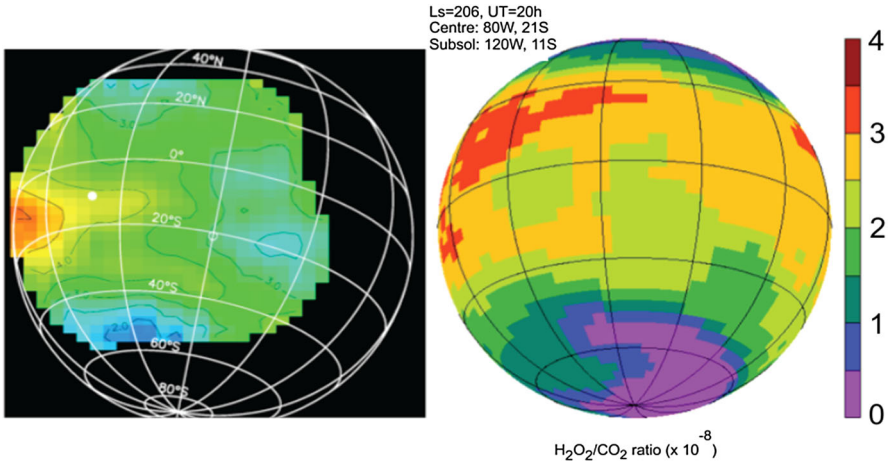

Fig. 11 *Left* map of the H_2O_2/CO_2 mixing ratio, derived from the line depth ratio of weak H_2O_2 and CO_2 transitions near 8 μm, obtained from data recorded by the TEXES imaging spectrometer at the Infrared Telescope facility (IRTF) in June 2003 (MY 26, Ls = 206°). The subsolar point is indicated with a *white dot*. The H_2O_2 mixing ratio is indicated by multiples of 10^{-8}; contours are separated by 0.5×10^{-8}. *Right* map of the H_2O_2 mixing ratio, in the same unit, as modeled by the GCM developed at the Laboratoire de Météorologie Dynamique, under the conditions of the TEXES observations. The figures are taken from Encrenaz et al. (2004)

Detection and abundance of CH_4

For over 10 years, there has been an active debate about the possible presence of methane in the Martian atmosphere. Because the terrestrial methane is mostly of biogenic origin, the possible implications of such a discovery on Mars could be of prime importance for astrobiology. In 2004, several teams, using different experiments, reported the detection of methane on Mars. First, Krasnopolsky et al. (2004), using ground-based high-resolution infrared spectroscopy, reported a tentative detection at a disk-averaged level of 10 ppbv. Using the PFS spectrometer aboard Mars Express, Formisano et al. (2004) and later Geminale et al. (2008, 2011) reported the detection of CH_4 through the Q-branch of its υ_3 band at 3.3 μm, with spatio-temporal variations ranging from 0 to 30 ppbv. The PFS detection, however, was at the limit of detectability. Mumma et al. (2004, 2009), again using ground-based high-resolution spectroscopy in the near-infrared range, reported the detection, in 2003, of a set of three plumes on scales of about 500 km, in the northern hemisphere during northern summer. The main plume contained about 19,000 tons of methane, with an estimated source strength of at least 0.6 kg/s, comparable with a massive hydrocarbon seep on Earth. Within each plume, the maximum local CH_4 mixing ratio was found to be about 35–40 ppbv. Finally, using TES observations of the Q-branch of the υ_4 band at 7.7 μm, Fonti and Marzo (2010) reported the tentative detection of CH_4 with variation with location and season; however, a subsequent analysis by these authors did not confirm this result (Fonti et al. 2015).

The conjunction of several independent detections first led to a general consensus on the existence of a transient source of methane and generated active research about

its possible origin (Atreya et al. 2007, 2011; Lefèvre and Forget 2009). However, there has been considerable debate about the validity of the methane detections. In the case of PFS, the data suffer from low spectral resolution (the whole Q-branch being detected in a single spectral channel) and large summations are needed to compensate the limited signal-to-noise ratio, which is not favorable for detecting transient phenomena. The ground-based observations of Krasnopolsky et al. (2004) have a high spectral resolution, but they suffer from a limited signal-to-noise ratio and from terrestrial contamination. The observations of Mumma et al. (2009) have a very good spectral resolution and a high signal-to-noise ratio, but they also suffer from the terrestrial atmospheric contamination. As pointed out by Zahnle et al. (2011), the two blue-Doppler-shifted methane transitions R(0) and R(1), identified as martian signatures by Mumma et al. (2009) in the wings of the strong methane telluric lines, also coincide with the $^{13}CH_4$ R(0) and R(1) terrestrial lines. An unambiguous detection of methane on Mars would require the observation of these lines when they are red-shifted, but this observation was not possible. In addition, subsequent observations, performed with more sensitive ground-based telescopes and instruments, failed to detect methane (Villanueva et al. 2013). If the detection of the plume in 2003 was real, its destruction mechanism within a lifetime of a few years remains to be identified (Lefèvre and Forget 2009; Zahnle et al. 2011). Indeed, the photo-destruction lifetime of CH_4 on Mars is expected to be about 300 years.

In 2015, the Curiosity rover has introduced a new element to the methane puzzle. While an upper limit of 1.3 ppbv had first been reported after the first year of campaign (Webster et al. 2013), subsequent observations led to the detection of a low background level of 0.7 ppbv with, in addition, the detection of an episodic release at a level of 7 ppbv (Webster et al. 2015). In summary, the question of the methane detection on Mars is still under debate. If its emission is transient and sporadic, and a definitive detection may be difficult to confirm. Hopefully, the NOMAD spectrometer aboard the ExoMars TGO (Trace Gas Orbiter, see Sect. 5.2) and the Methane Sensor for Mars (MSM) instrument aboard the Mangalyaan mission from India will bring new information to this question.

Detection and abundance of N_2 and Argon

These gases have no strong spectral signature from the UV to the radio ranges; hence, their detection was via mass spectroscopy, first by the Viking landers, and more recently by the Curiosity rover. The N_2 mixing ratio was first measured by the Viking mass spectrometers with a value of 2.7% (Owen et al. 1977). N_2 was believed to be the second most abundant species after CO_2, but a recent analysis by Curiosity has revealed that the abundances of ^{40}Ar (0.0207 ± 0.0002) and N_2 (0.0203 ± 0.0003) are actually equal (Mahaffy et al. 2013; Franz et al. 2015). Surprisingly, this result implies a $^{40}Ar/N$ ratio of 0.5 ± 0.01, significantly greater that the previous Viking value of 0.35 ± 0.08 (Owen et al. 1977; Oyama and Berdahl 1977). This result is puzzling, because the Viking measurement, coupled with the $^{14}N/^{15}N$ martian ratio (see Sect. 4.4.1), is in much better agreement with the mixing lines obtained for martian meteorites (Wong et al. 2013). As both the ^{40}Ar and N_2 abundances are expected to be constant over time, there is presently no explanation for the discrepancy between the Viking and Curiosity results.

Table 2 Upper limits of trace species

Molecule	Upper limit ($3\,\sigma$) ppbv	Method of detection	References
C_2H_2	3	IRIS-Mariner 9	Maguire (1977)
C_2H_4	4	Ground-based IR spectroscopy	Villanueva et al. (2013)
C_2H_6	0.2	Ground-based IR spectroscopy	Villanueva et al. (2013)
N_2O	65	Ground-based IR spectroscopy	Villanueva et al. (2013)
NO_2	10	IRIS-Mariner 9	Maguire (1977)
NH_3	8	IRIS-Mariner 9	Maguire (1977)
PH_3	100	IRIS-Mariner 9	Maguire (1977)
SO_2	0.3	Ground-based IR spectroscopy	Encrenaz et al. (2011)
OCS	70	Ground-based millimeter spectroscopy	Encrenaz et al. (1991)
H_2S	20	Ground-based millimeter spectroscopy	Encrenaz et al. (1991)
H_2CO	4	Ground-based IR spectroscopy	Villanueva et al. (2013)
HCl	0.2	HIFI/Herschel sub-mm. Spectroscopy	Hartogh et al. (2010)
HCN	2	Ground-based IR spectroscopy	Villanueva et al. (2013)
CH_3Cl	14	Ground-based IR spectroscopy	Villanueva et al. (2013)
CH_3OH	7	Ground-based IR spectroscopy	Villanueva et al. (2013)
HO_2	200	Ground-based IR spectroscopy	Villanueva et al. (2013)

Upper limits of trace species

A number of Martian atmospheric trace species have been reported in the literature, using the IRIS infrared spectrometer aboard Mariner 9 (Maguire 1977), ground-based infrared spectroscopy (Beer et al. 1971; Villanueva et al. 2013), ground-based millimeter spectroscopy (Encrenaz et al. 1991), and HIFI/Herschel sub-millimeter spectroscopy (Hartogh et al. 2010). Table 2, updated from Villanueva et al. (2013) and Smith et al. (2016), summarizes the most sensitive upper limits presently achieved.

Of particular interest are the upper limits obtained on H_2CO (Krasnopolsky et al. 1997), in contradiction with an earlier tentative detection by the Phobos spacecraft (Korablev et al. 1993), and on HCl (Hartogh et al. 2010), which implies a negligible role of chlorine chemistry on Mars. Sulfur gaseous species are also remarkably absent. By analogy with the Earth, sulfur dioxide SO_2 appears as a good tracer of volcanic activity; however, its upper limit is especially stringent (Encrenaz et al. 2011). On Earth, the SO_2/CH_4 ratio in the volcanic plumes is typically 10^3–10^4. This implies that the methane plumes of Mars, if confirmed, are not expected to be of volcanic origin.

2.2 The upper atmosphere

Mars' upper atmosphere is considered to be that above ~80 km. The related science investigations are called "aeronomy", a term suggested by Sydney Chapman in the 1940s. Our knowledge of Mars' upper atmosphere started with the first radio-occultation profiles acquired in the 60/70s by Soviet Mars and US Mariner spacecraft.

In 1976, the two Viking landers provided in situ measurements of the thermosphere and ionosphere, which established a reference point in terms of plasma composition and temperature during their descent in the Mars' atmosphere. The Viking orbiters provided many more radio-occultation profiles, a rich dataset later augmented by Mars Global Surveyor (1998–2005) and by Mars Express since 2004. Mars Global Surveyor also provided a useful dataset on energetic electrons and mapped the peculiar crustal magnetic field. In addition to the radio-science data (Pätzold et al. 2005; Peter et al. 2014), Mars Express continuously measures since January 2004 plasma properties of energetic ions, electrons, and neutrals above 250 km altitude with the ASPERA3 package (Lundin et al. 2004), vertical electron density profile, and magnetic field magnitude with the MARSIS radar since June 2005 (Gurnett et al. 2005, 2008; Morgan et al. 2013), and routinely measures the total electron content (Mouginot et al. 2008). The Mars Atmosphere and Volatile Evolution (MAVEN) spacecraft (Jakosky et al. 2015a, b) arrived at Mars in September 2014, opening a new era in the "exploration of the thin air". Atmospheric escape which takes place in this region is addressed in Sect. 4.4.

2.2.1 The vertical structure of the upper atmosphere of Mars

The upper atmosphere extends typically from 80 km up to 1000 km. Different atmospheric layers can be identified, as for any other planetary atmospheres: the ionosphere, thermosphere, and exosphere.

The ionosphere extends from about 80 km up to typically 500–600 km. Its vertical structure has been revealed mainly with two in situ measurements, thousands of radio-occultation profiles, and hundreds of thousands of radar soundings. On the dayside, the main layer created by solar extreme ultraviolet photoionization peaks at 120–140 km altitude, while a secondary layer created by soft X-ray photoionization is often detected around 110–115 km (Peter et al. 2014). A third layer can sometimes appear around 80–90 km (Pätzold et al. 2005; Withers et al. 2013), due to incoming dust particles depositing metallic species in the atmosphere (Pesnell and Grebowsky 2000; Molina-Cuberos et al. 2003). Above the main peak, additional layers or edges can be present (Kopf et al. 2008), most likely due to the interaction with the solar wind. At higher altitudes, above 400 km, an ionopause can sometimes be identified (Duru et al. 2009), although the concept of an ionopause at Mars is still a matter of debate.

Concerning the ionospheric composition, three ions were detected in 1976 (Fig. 12), by the retarding potential analyzers aboard the two Viking landers during the first in situ measurements of ions performed in another planetary ionosphere (Hanson et al. 1977). The main ionospheric layer peaks at an ion concentration of approximately 10^5 cm^{-3} just below 130-km altitude, and consists of 90% of O_2^+ and 10% of CO_2^+ ions. At higher altitudes, an O^+ ion layer reaches a maximum near 225 km. Known photochemical reactions in the ionosphere explain well this composition (Fox and Dalgarno 1979; Nagy and Gregobowsky 2015). New ions have been discovered by the Neutral Gas and Ion Mass Spectrometer aboard MAVEN: H_2^+, H_3^+, He^+, C^+, CH^+, N^+, NH^+, OH^+, H_2O+, H_3O^+, N_2^+/CO^+, $HCO^+/HOC^+/N_2H^+$, NO^+, HNO^+, HO_2^+, Ar+, ArH+. Ne^+, CO_2^{++}, and HCO_2^+ (Benna 2015; Benna et al. 2015).

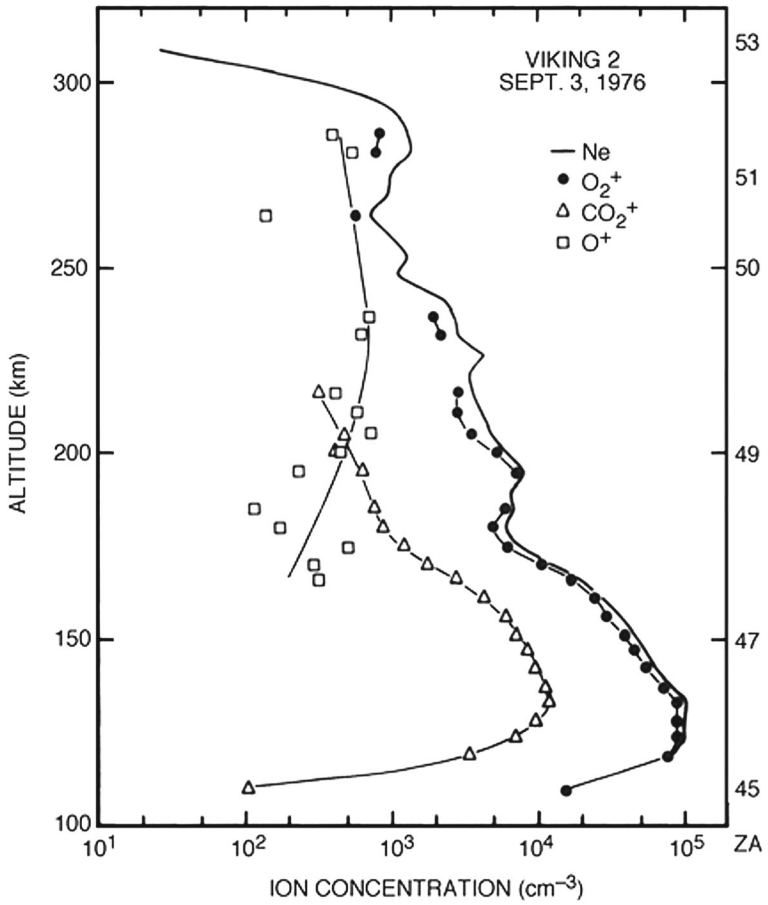

Fig. 12 Ion profile in the Mars' atmosphere, measured by the Viking 2 lander during its descent in 1976. The figures are taken from Hanson et al. (1977)

Information about plasma temperatures also comes from the Viking landers. Viking 1 measured ion temperatures of approximately 150 K near the main ionospheric peak increasing to an apparent exospheric temperature of 210 K near 175 km. Above this altitude, departures from thermal equilibrium with neutral gas occur, and the ion temperature increases rapidly to 1000 K at 250 km (Hanson et al. 1977). It is interesting to note that given the complexity of the data analysis, electron temperatures were published only 10 years after data acquisition (Hanson and Mantas 1988). This analysis shows that electron temperatures are several thousand degrees K. In addition, three different energetic electron populations were identified, characterized by three distinct temperature profiles. The high-temperature profiles can be interpreted with the presence of a magnetic field in the ionosphere. Analysis of Mars Global Surveyor radio-occultation measurements reveals a clear trend of elevated electron temperature with increasing solar zenith angle, as well as a putative asymmetry in electron temperature between the northern

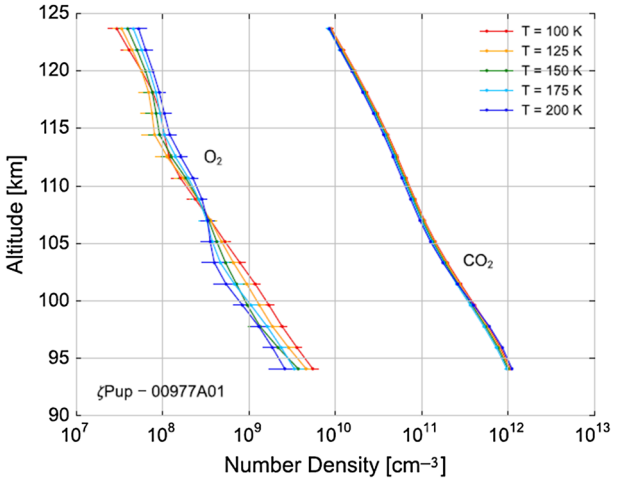

Fig. 13 CO_2 and O_2 abundances retrieved from stellar occultations. Over the range of 90–130 km, the altitude-averaged mixing ratio of O_2 relative to the major constituent CO_2 varies in space and time in the range of 3.1×10^{-3}–5.8×10^{-3}, with a mean value of 4.0×10^{-3}. This mean value exceeds by a factor of 3–4 those reported earlier for the lower atmosphere. However, some of the O_2 abundance and mixing ratio profiles determined here are similar to those measured by Viking in 1976 in the upper atmosphere. The figures are taken from Sandel et al. (2015)

and southern hemispheres, possibly linked to the crustal magnetic fields (Cui et al. 2015).

The thermosphere extends from 100 to 200 km. Carbon dioxide is the main component, followed by N_2, O, CO, O_2, and NO (Nier and McElroy 1977; Nagy and Gregobowsky 2015). Atomic oxygen was never measured until MAVEN arrived at Mars, and was usually obtained via theoretical/numerical modeling. In situ measurements by MAVEN provide reliable atomic oxygen densities down to 150 km, with densities at 200 km close to 5–6 10^7 cm^{-3} (Bougher et al. 2015). O_2 altitude profiles were recently retrieved below 130 km, for the first time, from stellar occultation profiles (Sandel et al. 2015, Fig. 13). The neutral temperature increases with altitude to an overall maximum value (200–350 K) and then becomes constant. The thermosphere is subject to in situ forcing due to gravity/planetary waves and solar thermal tides (Keating et al. 1998; Bougher et al. 2014). The dynamics of the thermosphere are still poorly constrained by data.

The upper limit of the thermosphere is the exobase, around 200–230 km (Boqueho and Blelly 2005; Feldman et al. 2011), above which the exosphere expands. In this region, collisions no longer dominate, the neutrals can be considered as individual ballistic particles. A corona is composed of light species, hydrogen, carbon, and oxygen, which can escape to space. A population of exothermal species originates from photochemical reactions occurring in the ionosphere below (Bougher et al. 2014). A typical reaction is the dissociative recombination of O_2^+ ions with electrons.

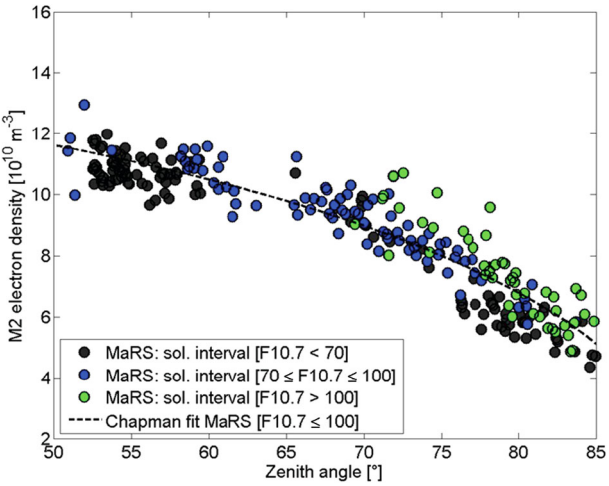

Fig. 14 Observed (*circles*) and modeled (*dashed line*) peak densities for the main ionospheric layer, as a function of the solar zenith angle. The *color of the circles* indicates the interval of solar activity. The density varies as cos0.44 (SZA), while a pure photochemical layer would follow a cos0.5 expression. The figures are adapted from Peter et al. (2014)

2.2.2 Variability of the upper atmosphere

The thermosphere/ionosphere coupled atmospheric layers are very variable in nature. To understand this system, it is important to list all possible sources of variability, in particular temporal, and to quantify their effects. This is essential for the study of atmospheric loss, as the upper atmosphere is the reservoir available for escape. A significant progress has been achieved in the last 10 years. The temporal variations are due to diurnal, seasonal, and solar cycles, and to episodic events. The external drivers are the solar extreme ultraviolet and X-ray photons, solar energetic particles, solar wind events, and interplanetary dust. The diurnal cycle is relatively well understood, with the main properties of the upper atmosphere varying with the solar zenith angle (e.g., Fox and Dalgarno 1979). Figure 14 shows the variation of the electron density as a function of solar zenith angle, as deduced from Mars Express radio-occultation data.

Seasonal influence is important to consider, given the planet tilt angle and the orbit eccentricity. These effects, difficult to distinguish in the data, are best addressed by 3D modeling work (e.g. Valeille et al. 2009), and indicate that they are important for the spatial distribution of neutral species, moderate for altitude variations of atmospheric boundaries and for neutral thermospheric densities. One issue is that the Mars orbit eccentricity demands that both the solar cycle and seasonal variations in upper atmosphere be considered together (Bougher et al. 2014). Concerning the solar cycle, the relevant dataset in term of minimum temporal coverage is just being completed; therefore, many studies are expected from now on. Withers (2014) analyzed Mars Global Surveyor radio-occultation and Mars Express radar data and confirmed the expected trend that the ionospheric peak electron density increases smoothly with

increasing solar activity represented by the F10.7 space weather proxy, named from the solar radio flux at 10.7 cm (2800 MHz). This trend is not obviously identified in the Mars Express radio-occultation data alone (Peter et al. 2014). What is more evident in this dataset is the increase of the peak altitude with solar activity, especially at high solar zenith angle. Girazian and Withers (2013) propose an empirical relationship, with the maximum electron density varying as the square of F10.7. Sanchez-Cano et al. (2015) used Mars Express radar data covering almost one solar cycle and analyzed differences in the shape of the topside electron density profiles. These variations seem to be linked to changes in the ionospheric temperature due to the solar cycle variation. In particular, Mars' ionospheric response to the extreme solar minimum between end-2007 and end-2009 followed a similar pattern to the response observed in the Earth's ionosphere, despite the large differences related to internal origin of the magnetic field between both planets. More work is needed to fully characterize solar cycle effects on the upper atmosphere.

The most complex sources of variability of the upper atmosphere are the transient events, because of their unpredictability, and varying strength, duration, and repetition rate. In addition, these events are diverse by nature, and can be mixed with each other. Their effects on the upper atmosphere are, therefore, difficult to assess in detail, and for now, we only have a collection of events, but the overall interpretation is still lacking. Co-rotating interaction regions and coronal mass ejections induce solar wind dynamic pressure variations, whose effect is to compress considerably the magnetosphere and ionosphere (Opgenoorth et al. 2013). At the same time, increased plasma transport occur over the terminator, which extends the ionosphere on the nightside, while elevated ionization is produced in the lower ionosphere due to solar energetic particle impact (Morgan et al. 2010, 2014). These effects can last for a few days. Enhanced X-rays and EUV solar fluxed during a solar flare can cause up to 200% enhancements to the electron densities (Mendillo et al. 2006). Withers et al. (2012) published Mars Express radio-occultation measurements of vertical ionospheric profiles, revealing a rich and complex range of features, which are not explained: single, double, or triple scale heights are observed, as well as sharply pointed, flat-topped, and wavy shapes in the main ionospheric layer. Finally, ionospheric layers meteoritic in origin appear sporadically below 100 km altitude (Molina-Cuberos et al. 2003). So far, 89 events have been identified in the Mariner 7/Mariner 9/Mars Global Surveyor/Mars Express datasets (Withers et al. 2013; Pätzold et al. 2005). One of the proposed causes of temporal variations in the occurrence rate of meteoric layers is meteor showers.

Regarding spatial variability, the upper atmosphere is also affected by the crustal magnetic field, discovered by Mars Global Surveyor (Acuna et al. 1999). Elevated ionospheric densities and localized spatial structures are seen above magnetic anomalies (Andrews et al. 2014, 2015; Matta et al. 2015; Ma et al. 2014; Dubinin et al. 2012; Safaeinili et al. 2007), and can be explained to first order by a larger ionization due to higher energetic particle fluxes spiraling along the magnetic field lines (Lillis and Fang 2015).

It is very important to mention that the upper atmosphere is affected by the lower atmosphere. Upward propagating atmospheric waves and tides, possibly due to Mars topography, can have a significant influence on thermospheric structure and dynamics (Bougher et al. 2014 and reference therein), and thus on the ionosphere, e.g., a variable

maximum altitude for the ionosphere. One of the most intriguing effects is due to dust storms: during these events, the atmospheric opacity increases, and the lower atmosphere is heated, and expands. The density of the thermosphere increases (Keating et al. 1998), and the altitude of the peak electron density can increase by up to about 30 km (Wang and Nielsen 2003). Withers and Pratt (2013) have shown that the upper atmospheric regions can be affected globally, and at altitudes as high as 160 km. The response of the upper atmosphere to storms can be a few days, while the decay takes much longer (a few months). Thermospheric density can vary by an order of magnitude. Another example of communication between lower and upper atmospheric layers is the recent discovery that the lower atmosphere is supersatured with water vapor (Maltagliati et al. 2011). The implication is that there is much more water vapor in the atmosphere than was generally accepted, which can be photo-dissociated into lighter components H and O. This can increase the density of the exosphere and the water loss.

2.2.3 Airglow and auroras

Optical emissions, in particular in the ultraviolet range, are a useful diagnostic of processes at work in the upper atmosphere. They are referred to as airglow if EUV solar radiation is the initial source of energy causing the excitation and as aurora if the source is energetic particle impact (e.g., Schunk and Nagy 2009). Data are from the NASA Mariner missions in the 1970s (e.g., Stewart 1972; Barth et al. 1972b; Conway 1981), from the ESA Mars Express mission (e.g., Bertaux et al. 2005a, 2006; Leblanc et al. 2006, 2007; Cox et al. 2008; Simon et al. 2009), and more recently from MAVEN (Jain et al. 2015). These observations allowed the detection of species in the upper atmosphere and their abundances to be constrained. In addition, the atmospheric scale height can be estimated from the emission profile, and the corresponding exospheric temperature can be evaluated, and values are typically in the range 200 to 400 K, depending on the solar activity. The study of airglow can also be used to track and quantify the day-to-night atmospheric circulation, as in the case of the γ and δ bands of nitric oxide night emissions (Bertaux et al. 2005a; Cox et al. 2008). The challenging identification of hot atomic oxygen from airglow observations, in particular at 130.4 nm, is a very important discovery being used to understand the behavior of exospheres and coronas (Paxton and Vervack 2001; Chaufray et al. 2008, 2009; Feldman et al. 2011). The presence of hot hydrogen at high altitude is still an open question.

Auroras have been first detected by the UV spectrometer SPICAM aboard Mars Express (Bertaux et al. 2005b), as illustrated in Fig. 15. They correspond to a distinct type of auroras not seen elsewhere in the Solar System: a martian aurora is a highly concentrated and localized emission controlled by crustal magnetic field anomalies. It is believed to be produced by energetic electron impact, with a kinetic energy of a few tens of eV up to 300 eV, channeled by magnetic field lines organized into cusp-like structure (Leblanc et al. 2006, 2008; Liemohn et al. 2007; Lundin et al. 2006; Brain 2006; Gerard et al. 2015). All in all, about ten events have been identified so far, all near regions of crustal magnetic fields. Strong correlations have been found between the UV observations of auroras, precipitating electron flux measured by the ASPERA-3/Electron

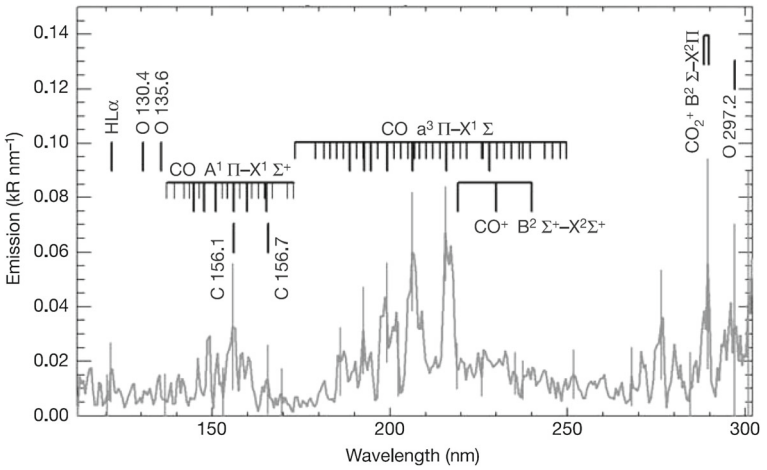

Fig. 15 Ultraviolet spectrum of an aurora emission (from Bertaux et al. 2005a). The CO Cameron band is clearly seen. Other main emissions are emitted from CO_2+ and atomic oxygen

Spectrometer, and increase of total electron content measured by the MARSIS radar data (Leblanc et al. 2008). In some cases, the Mars Express/ASPERA measurements show the existence of long-lived and active aurora-type magnetic flux tubes with a width of 20–150 km. This aurora activity has an influence on the atmospheric escape (Dubinin et al. 2009). The analysis of MAVEN data (Schneider et al. 2015) has shown a new kind of martian aurora, called diffuse aurora, observed at low altitudes, over areas not characterized by a crustal fields, and likely due to the penetration in the atmosphere of very energetic particles of ∼200 keV energy.

2.2.4 Additional observations and concluding comments

On 19 October 2014, the Oort-cloud comet Siding Spring made a close encounter with Mars, at a distance of 140,000 km (or 41 martian radii), and at a relative velocity of 56 km/s. That was the first time that any effects of cometary material penetrating into the Mars' atmosphere could be investigated. Predictions have been published by Yelle et al. (2014), Withers (2014), and Gronoff et al. (2014). A major effect was the deposition of metallic species in the upper atmosphere and the associated increase in ionization. Measurements by different instruments onboard the three spacecraft Mars Reconnaissance Orbiter, Mars Express, and MAVEN have provided a complementary view: the SHARAD radar recorded high values of the total electron content on the nightside (Restano et al. 2015), while the MARSIS radar detected a strong ionospheric layer just below 100-km altitude, consistent with the ablation of dust particles in the atmosphere (Gurnett et al. 2015), see Fig. 16. These observations were complemented by MAVEN data, in which metallic ions, such as Mg+ and Fe+, were identified for the first time in the Mars' atmosphere, both from the ion mass spectrometer and the UV spectrometer (Benna et al. 2015; Schneider et al. 2015). These new data represent a new field of study on how the upper atmosphere reacts to strong and short-duration

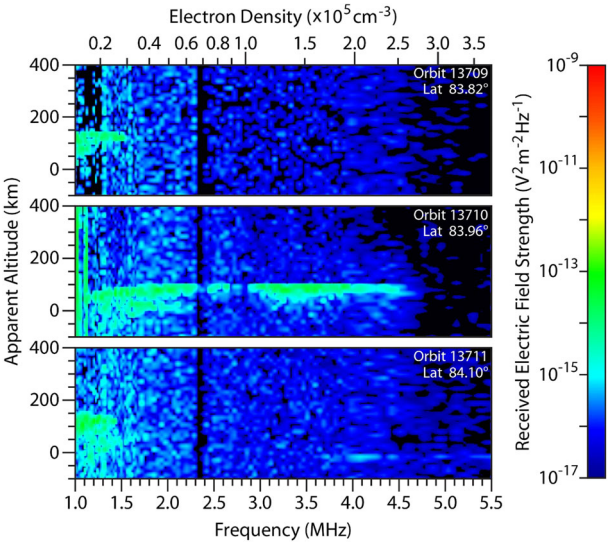

Fig. 16 Ionograms for three Mars Express passes around the time of closest approach of the siding spring comet to Mars, over the northern nightside polar region showing the *color-coded* intensities of the received radar echoes. The frequency of the transmitted radar pulse is on the *horizontal axis of each ionogram*, and the apparent altitude of the resulting echoes is on the *vertical axis*. The apparent altitude assumes that the radar pulse propagates vertically at the speed of light, with no correction for plasma dispersion. Note the strong radar echoes from an ionized layer due to meteor ablation at an altitude of about 100 km extending up to about 4.6 MHz in the second row (Mars Express orbit 13710). The figures are taken from Gurnett et al. (2015)

events that occur at well-constrained times. It is too early to discuss the overall effects of cometary particles in the evolution of the red planet. Wang et al. (2016) and Yung-Ching et al. (2016) predicted that the cometary sputtering may have played a non-negligible role in Mars atmospheric evolution. This would need to be addressed further, as this kind of cometary encounter should have occurred more frequently in the early Mars' history.

Finally, Sánchez-Lavega et al. (2015) recently reported very intriguing observations of the upper atmosphere of Mars. Extremely high-altitude plumes at the terminator at 200–250 km or more above the surface were spotted in March and April 2012, from ground-based telescopes. The lifetime of these features was about 10 days. They could be ice particles reflecting sunlight, or related to a solar wind event, however, until now, no clear explanation has been given to explain these observations, although it is interesting to note that this period was characterized by an active solar period, during which coronal mass ejections hit Mars (Andrews et al. 2015).

In summary, the upper atmosphere of Mars is the highest altitude envelope of the planet, is in direct interaction with the interplanetary environment, and strongly coupled with the lower atmosphere. This region is essential in the interpretation of the overall system, in particular to understand the past and future evolution of Mars and its climate. Two prevailing challenges affect study of the Mars upper atmosphere: (1) the multifaceted couplings between different layers and (2) the extreme variability due to many external and internal controlling factors.

2.3 Cryosphere

The *cryosphere* includes all reservoirs containing frozen volatiles (H_2O and CO_2), including polar caps, glaciers, and any form of ground ice. While polar caps are the most obvious landforms to link with the cryosphere, the search sub-surface-ice in crustal pores requires more indirect observations, measurements, and models.

2.3.1 Polar caps

The polar caps are the largest visible reservoir of surface-ice on Mars and their study is important for the understanding of the history and fate of H_2O and CO_2 as well as of the current and recent climate. Ground-based observations from the Earth first showed the polar caps and spectroscopic observations suggested that the northern cap consisted mostly of water ice, whereas the southern cap was dominated by CO_2 ice (Kieffer 1979; Paige et al. 1990). High-resolution images display well-developed pits, typically 100 m in diameter and 10 m in thickness, that were interpreted as the effect of CO_2 sublimation (e.g., Piqueux et al. 2003). These landforms are specific to the southern residual cap; they are not present on the northern residual cap. The OMEGA spectrometer onboard Mars Express later confirmed that the southern CO_2 ice was only a thin section underlain by a 1–2-km-thick water ice cap (Bibring et al. 2004). The polar terrains are among the youngest surfaces on Mars. High-resolution images of the northern cap surface fail to reveal any craters with diameters >300 m within the $\sim 10^6$ km^2 covered by the deposits (Herkenhoff et al. 1997), proving a recent age of the ice deposits (<1 My).

Recent information about the sub-surface water content has been provided by the radar instruments, Mars Advanced Radar for Sub-surface Analysis (MARSIS) aboard Mars Express, and SHAllow RADar (SHARAD) aboard Mars Reconnaissance Orbiter. Figure 17 shows the structure of the south-polar layered deposits sounded by the MARSIS radar (Plaut et al. 2009). The polar layered deposits extend beyond and beneath a polar cap of bright-white frozen carbon dioxide and water. For most of the area, a reflection is detected at a time delay that is consistent with an interface between the deposits and the underlying lithic substrate. The ice is almost pure frozen water. Radar signals penetrate deep into the deposits and indicate a maximum thickness of 3.7 km. Maps of the thickness show an asymmetric distribution of the deposits and regions of anomalous thickness. The total volume is estimated to be 1.6×10^6 km^3, which is equivalent to a Global Equivalent Water (GEL) layer approximately 11 m thick (Plaut et al. 2009; Orosei et al. 2015). Radar soundings of the North Polar Layered Deposits by MARSIS (Plaut et al. 2012) are illustrated in Fig. 17. The observations indicate that the ice is nearly pure, a result that has been confirmed by the SHARAD data (Phillips et al. 2008; Grima et al. 2009). Regarding the internal stratigraphy of the north polar layered deposits, radar reflections within the deposits have revealed a clear periodic layering patterns, which can be explained by approximately million-year periodicities in Mars' obliquity or orbital eccentricity (Phillips et al. 2008). The lower section of the north polar plateau consists of a distinct, complex, layered unit commonly called the basal unit that can be fully mapped by MARSIS. The total volumes of the polar deposits and the basal unit are estimated to be 7.8×10^5 and 4.5×10^5 cubic

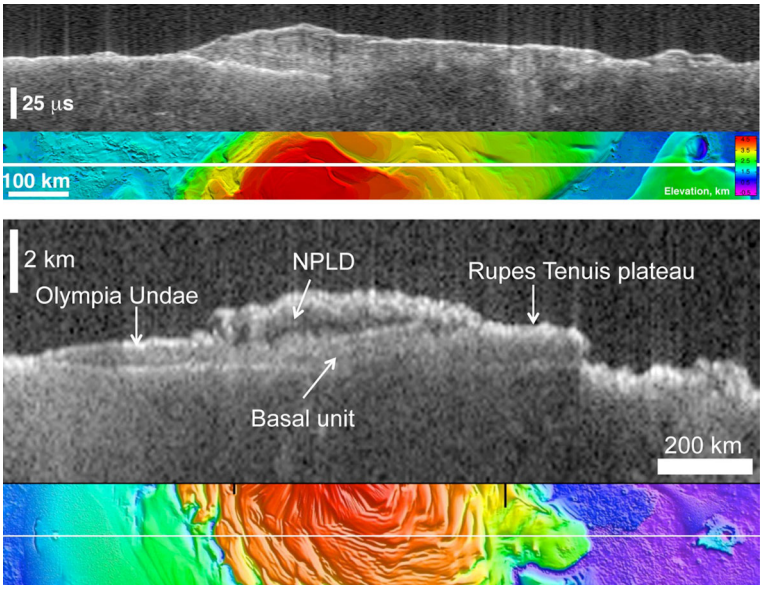

Fig. 17 *Top* bright lower echo from Mars' south-polar layered deposits (Plaut et al. 2009). The *upper image* of this composite is a 'radargram' from the MARSIS radar on board Mars Express. The *lower image* shows the position of the ground track of the spacecraft (indicated by a *white line*) on an topographic map of the area based on data from the MOLA Laser Altimeter on board Mars Global Surveyor. The images are 1250 km wide. The MARSIS radar echo trace splits into two traces on the *left* side of the image, at the point where the ground track crosses from the surrounding plains onto elevated layered deposits. The upper trace is the echo from the surface of the deposits, while the lower trace is interpreted to be the boundary between the lower surface of the deposits and the underlying material. The strength of the lower echo suggests that the intervening material is nearly pure water ice (NASA/JPL/ASI/ESA/Univ.of Rome/MOLA Science Team). *Bottom* MARSIS observation of the north polar plateau. The *vertical dimension* has been converted from time to distance. The basal unit is marked by a diffuse echo signature, with a relatively sharp upper boundary and a generally reflective lower contact. This lower contact, presumably with the underlying Vastitas Borealis formation, is approximately flat-lying in this profile, and extends across the entire plateau, from beneath the Olympia Undae dunes at *left* to the base of the Rupes Tenuis scarp at right. The figures are taken from Plaut et al. (2012)

kilometers, respectively (Selvans et al. 2010). The data analysis suggested that the composition of the basal unit is half ice and half dust (Plaut et al. 2012).

2.3.2 Mid-latitude glaciers

Evidence for the distribution of ice on Mars has been presented through interpretation of Viking images (e.g., Squyres 1978; Lucchitta 1984). Glacial tongues are present in abundance in the mid-latitudes (30°–50°) in both hemispheres. They have been named *lobate debris aprons* from a purely morphological point of view (Squyres 1978; Squyres and Carr 1986), because they consist of tongues extending over 10–30 km with a lobate shape typical of viscous flows. MOLA topography shows that the thickness of aprons is on the order of several hundreds of meters and that their topographic profiles are typical of the flow and rheology of rocky glaciers with an ice volume fraction

Fig. 18 Glacial tongues with lateral moraines in Greg Crater, Mars (113°E, 38°S; CTX image, P03_002320_1413_XI_38S246W). Note that the pitted texture in the bottom of the image is a result of ice sublimation

>30% in volume (Mangold and Allemand 2001; Mangold et al. 2002; Li et al. 2005). Later, SHARAD radar detected an ice content of 80% showing that these tongues are nearly pure water ice glaciers (Holt et al. 2008; Plaut et al. 2009). Lobate aprons do not display ice at their surface: they are classified as debris-covered glaciers with a dust blanket protecting ice from ablation (Mangold 2003; Head et al. 2003; Chuang and Crown 2005; Levy et al. 2010; Head et al. 2010) which explains the lack of H_2O detection using spectroscopy. Thick lobate aprons (>100 m) are frequently located at the dichotomy boundary, especially around buttes from the so-called fretted terrains in Deuteronilus Mensae and East of Hellas Planitia where a large variety of glacial landforms have been observed, including moraine-bounded glacial tongues (Fig. 18) (e.g., Arfstrom and Hartmann 2005; Levy et al. 2007; Hartmann et al. 2014).

2.3.3 Near-surface ground ice

P*ermafrost* is defined as the location where the ground is permanently below 0 °C, independently of the presence, or the absence, of water ice. Nevertheless, *periglacial landforms* are closely connected to the presence of ice in the permafrost (and independently of the presence of glaciers).

Thermal contraction polygons are one of the most characteristic landforms involving ground ice on Earth (e.g., French 1996) and their existence on Mars was theoretically predicted by Mellon (1997). Water ice has a thermal expansion coef-

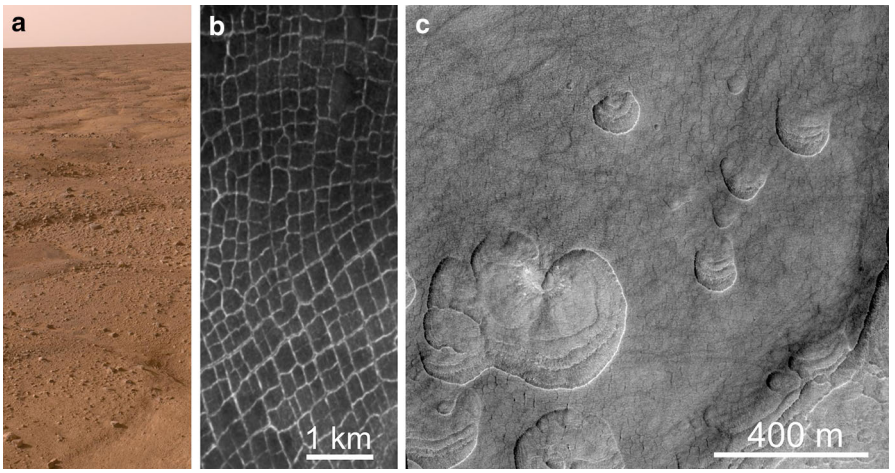

Fig. 19 **a** In situ image of thermal contraction polygons at Phoenix landing site (NASA/MRO/MSSS/CTX). **b** Orbital image of thermal contraction polygons in polar regions (MOC image #E1900409, 70.1°N, 65°E) (NASA/MGS/MSSS/MOC). **c** Scalloped terrains formed by sublimation of an ice-rich layer (46N, 90E, HiRISE image ESP_025831_2260) (NASA/MRO/UA/LPL/HiRISE)

ficient one or two orders of magnitude larger than sediments. Recurrent variations in temperatures create a thermal stress in the ground that produces polygonal networks of cracks (Fig. 19). Large polygons were observed by Viking images and later observed at kilometer scale, but their link with thermal contraction processes are unclear, and they are, perhaps, better related to shrinkage from sediments in ancient periods (Oehler and Allen 2012). The high-resolution imagery of the Mars Global Surveyor orbiter has revealed thousands of images in the high-latitudes with polygons, with widths from few meters to 500 m, that are similar in shape and size to polygonal contraction cracks observed on Earth (Seibert and Kargel 2001; Mangold 2005; Levy et al. 2010).

Additional evidence for sub-surface-ice came in parallel to these morphological observations with the discovery by the Gamma Ray Spectrometer (GRS) experiment aboard the Mars Odyssey orbiter, of the presence of hydrogen atoms in large abundances around the polar caps, soon interpreted as the signature of water molecules (Boynton et al. 2002; Feldman et al. 2002). The concentration of water ice may reach 70% at latitudes higher than 60°, corresponding to an ice-rich layer located a few centimeters to tens of centimeters below the surface, with detection limited to the first meter. It has been shown that contraction crack polygons are especially abundant where near-surface water ice has been detected by neutron spectroscopy (Feldman et al. 2004; Mangold et al. 2004a).

An important observation was performed by the Phoenix lander, which verified the presence of water ice in the martian sub-surface, inferred from morphological observations, ice stability modeling, and Mars Odyssey Neutron Spectrometer (Mellon and Jakosky 1993; Mellon et al. 2004). The Phoenix team, using the robotic arm and scoop, excavated 12 trench complexes into the soil surface, exposing various deposits of ice-rich material at the ice table beneath a layer of relatively dry and weakly cohesive soil with a mean depth of 4.6 cm (Mellon et al. 2009). Figure 20 shows the sublimation

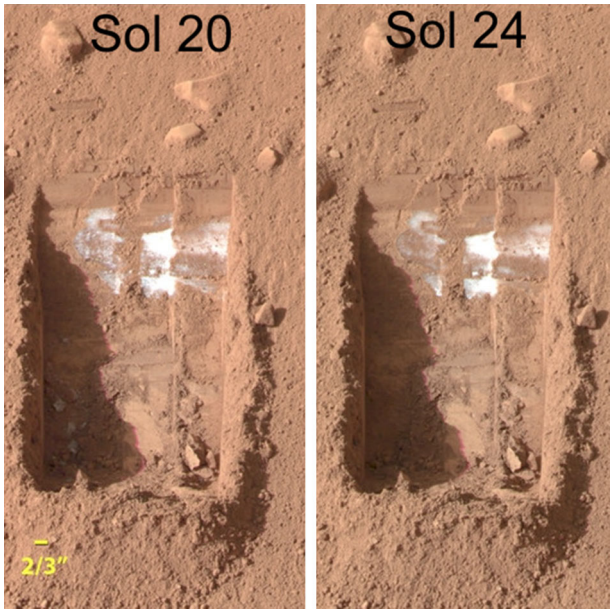

Fig. 20 *Color images* acquired by Phoenix Lander's Surface Stereo Imager on the 21st and 25th days of the mission, or Sols 20 and 24 (June 15 and 19, 2008). These *images* show sublimation of ice in the trench informally called "Dodo-Goldilocks" over the course of 4 days. In the *lower left corner of the left image*, a group of lumps is visible. In the *right image*, the lumps have disappeared, similar to the process of evaporation (NASA/JPL-Caltech/University of Arizona/Texas A & M University)

of ice as imaged by the lander. Indeed, ice is currently not stable at the surface of Mars above 200 K due to the low partial pressure of water vapor in the atmosphere. A significant ice heterogeneity was observed, with two major forms: ice-cemented soil and relatively pure light-toned ice. Ice-cemented soils, which comprised about 90% of the icy material exposed by trenching, are best explained as vapor deposited as pore ice in a matrix supported porous soil. The origin of these relatively pure ice deposits appears most consistent with the formation of excess ice by soil ice segregation, such as would occur by thin film migration and the formation of ice lenses, needle ice, or similar ice structures (Mellon et al. 2009).

Water transport in the ice-rich near-surface regolith occurs primarily via vapor diffusion (Chevrier et al. 2008; Hudson et al. 2009; Sizemore 2010). Water vapor diffusion has direct implications in shaping specific landforms (e.g., Mellon et al. 2004). Landforms due to sublimation of ground ice are ubiquitous in mid- and high-latitudes where ice is unstable through time. Sublimation landforms are especially developed between 30° and 60° of latitude in both hemispheres (e.g., Kreslavsky and Head 2002). Sublimation-related landforms include more or less regular patterns of networks of pits and knobs, coalescent troughs, usually at the 10- to 100-m scale. Preexisting fractures, such as thermal contraction cracks or glacier cracks, can enlarge to generate a regular network of troughs by differential sublimation rates (Mangold 2003; Levy et al. 2009). Scalloped terrains (Fig. 19c) represent asymmetric depressions

likely formed during a higher obliquity regime in a region of high ground ice content (Séjourné et al. 2011). Two regions where scalloped terrains are found, Utopia Planitia and Malea Planum, are expected to be the host of near-surface-thick ice-rich deposits (Lefort et al. 2009). Interpreting landforms as the result of sublimation of ice from the ground is of strong interest for detecting buried ice not visible from geophysical instruments or inferred the past–present of near-surface-ice that has been partially or totally removed by sublimation.

2.3.4 Deep cryosphere and deep hydrosphere?

Early on from Viking images, it was proposed that a specific class of impact craters possessing a continuous and lobate ejecta blanket extending up to >3 times, the crater radius were linked to the latitudinal-dependent presence of sub-surface ground ice (Carr et al. 1977; Mouginis-Mark 1979; Schultz and Gault 1979; Costard 1989; Barlow 2004; Meresse et al. 2006) responsible for the fluidization and development of instabilities during a ground-hugging flow (Barlow 1994, Baratoux et al. 2002; Barnouin-Jha et al. 2005). This interpretation was then supported by the observation of similar ejecta morphologies on Ganymede and Europa, the icy satellites of Jupiter (Boyce et al. 2010). However, lobate ejecta are also observed on Venus and form in association with vortex-ring instabilities in the thick atmosphere (Barnouin-Jha and Schultz 1996; Barnouin-Jha 1998), suggesting that morphological observations alone are ambiguous. Evidence of grain-sorting mechanism from thermal observations (Baratoux et al. 2005; Mouginis-Mark and Baloga 2006) is additional key observations that have been discussed against hypotheses of emplacement, but do not lead to definitive conclusion regarding the respective role of sub-surface or atmospheric volatiles.

Geophysical models suggest that the permafrost would transition from ground ice to liquid water at about ∼2 to 8 km depending on latitude, geothermal heat flux, and rock properties (Clifford 1993). Study of martian meteorites and mineralogical observations supports the hypothesis of sub-surface water in the past (Chen et al. 2015; Filiberto et al. 2016), but no direct evidence exists of its persistence until the present. The sub-surface sounding radar MARSIS was designed to detect liquid water below the surface (Picardi et al. 2005); however, no positive detection has been claimed so far (Orosei et al. 2015), though it should be noted that data coverage is not global. Furthermore, the lack of radar detection does not uniquely rule out the presence of water, as a radar echo from an aquifer could be sufficiently attenuated by the intervening medium to prevent its detection (Farrell et al. 2009). For this reason, the development of accurate methods for the inversion of the radar signal remains the main priority for the MARSIS team (Orosei et al. 2015).

2.3.5 Global water ice content

The depth of the polar layered deposits has been measured, and water ice in the deposits corresponds to a global equivalent layer (GEL) of water of ∼10–12 m at the south and ∼8–10 m at the north (Plaut et al. 2009; Selvans et al. 2010). MARSIS has produced unique data about the presence of water ice down to depths of several tens of meters in Vastitas Borealis, with an inferred volume equivalent to a polar cap (Mouginot 2010).

Estimations show that ice present in all glacial landforms and in the porosity of the permafrost may correspond to the equivalent of a 50–200-m-thick GEL (Mangold et al. 2002; Durham et al. 2009; Lasue et al. 2013). This result may still be too low to account for a larger initial water content, as estimated from erosional features to be >500-m GEL (Carr 1986). These estimates suggest a decrease of sub-surface water content with time (see Sect. 4).

2.4 Crustal composition and structure

The crust is the upper layer of the solid part of the planet, in contact with the atmosphere and lying above the mantle. It is chemically distinct from the mantle. With the exception of surface material of some asteroids that may escape melting (Weiss and Elkins-Tanton 2013), the term applies to the continuously extracted solid or liquid materials from the underlying mantle source. The density contrast between the extracted material and mantle source drives the solid-liquid segregation and mass flux. Knowledge on the present composition and structure of the martian crust comes from different sources of information: orbital and in situ data, martian meteorites, and geophysical constraints (e.g., topography, field of gravity, and moment of inertia).

2.4.1 Crustal composition from mineralogical analyses

Remote-sensing data in visible, near-infrared (e.g., Mustard et al. 2005; Bibring et al. 2005), and thermal infrared domains (Bandfield et al. 2000) provide constraints on the surface occurrences and concentrations of several groups of minerals (e.g., silicates, sulfates, carbonates, and oxides/hydroxides) at the tens of meters to kilometer scale. Gamma ray or neutron spectroscopy was used to map concentration of several chemical species (e.g., H, Si, Cl, K, Fe, and Th in Boynton et al. 2007, S in King and McLennan 2010) from orbit at the ~500-km scale. Analytical tools sent to Mars on Rovers or landers and analyses of samples naturally brought naturally to Earth by impacts (i.e., martian meteorites) provide additional constraints on crustal chemistry and mineralogy (e.g., Rieder et al. 1997 for Mars Pathfinder; Squyres et al. 2006 and Arvidson et al. (2006) for the Mars Exploration Rovers; Boynton et al. 2009 for the Phoenix lander, McLennan et al. 2014 for the Curiosity Rover; Lodders 1998; Grott et al. 2013 for a review of martian meteorites chemistry and mineralogy). However, this source of information is not necessarily representative of the bulk crust, and in particular, there is an obvious sampling bias when the young age of most of the Martian meteorites is compared with the distribution of ages of the rocks exposed at the surface. None of these surface or near-surface data may be representative of deep crustal material that is not accessible to remote-sensing spectroscopic imaging or sampling.

2.4.2 Constraints from geophysical data

Inversion of geodetic and geophysical data (mean density, gravity field, moment of inertia factor, tidal love number, and tidal dissipation factor) provides constraints on the crustal structure and composition, and insights into the portion of the crust that

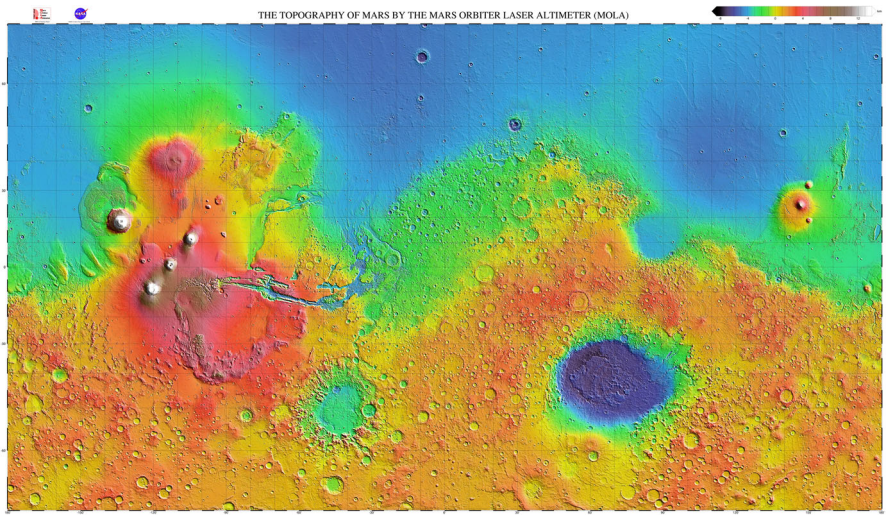

Fig. 21 MOLA altimetry data with main related surface topography (Zuber 2001)

are not exposed at the surface (Fig. 21, Sohl and Spohn 1997; Zuber 2001; Wieczorek and Zuber 2004; Sohl et al. 2005; Khan and Connolly 2008; Rivoldini et al. 2011; Baratoux et al. 2014). Models of crustal thickness, assuming a constant crust-mantle density contrast, produce a crustal volume corresponding to 4.4% of the planet (average thickness of ∼50 km) and a north–south dichotomy in the crustal structure. The crustal dichotomy does not entirely correlate with the geological boundary of the hemispheric dichotomy (Fig. 21). The crust is thinned at impact basins and along the central axis of Valles Marineris. Major volcanic provinces are characterized by a thicker crust (e.g., Tharsis and Elysium), suggesting that the accumulation of volcanic products largely contributes to their topography (Zuber 2001).

Geophysical inversions do not provide a unique solution. There is, for instance, a well-known trade-off between crustal density and crustal thickness. Surface imagery indicates prolonged geological activity (e.g., Greeley and Schneid 1991a; Grott et al. 2013, see Sect. 3.2), like on the Earth, but unlike the Moon or Mercury. Numerical models of evolution of the interiors are used to predict the crustal growth rate as a function of the time and suggest that most of the crust were produced in the early history, with episodic additions of material. Therefore, the present crust is the result of the long-term evolution of the crust-mantle system and is a complex and heterogeneous component of the planet. This implies that it is challenging to combine surface observations obtained at various scales with geophysical inversions into a self-consistent average model of crustal composition and structure.

2.4.3 Integrating geophysical and geochemical approaches

Some robust observations and facts may be stated combining chemical, mineralogical, and geophysical data released over the last 20 years. On one hand, the surface of Mars is dominated by tholeiitic basalts composed of pyroxene, feldspar and olivine

(McSween et al. 2009; Grott et al. 2013). Isotopic data on Martian meteorites suggest that crustal recycling, in contrast with the Earth, has been very limited on Mars (Halliday et al. 2001). The detection of olivine at the surface (Hamilton and Christensen 2005; Koeppen and Hamilton 2008; Ody et al. 2013), the Mg number (defined as Mg/(Mg + Fe) in molar abundance and written Mg#) of olivine in the Martian meteorite (Baratoux et al. 2011), and the composition of spatially dominant olivine-rich basalt at Gusev crater (McSween et al. 2006) suggests that primitive magmas are common at the surface of Mars. The martian basalts are relatively enriched in iron, in comparison with terrestrial basalts, which are direct consequence of the low Mg# of the mantle and smaller core. The grain (pore-free) density of these basalts is about 3100–3300 kg/m^3 (Baratoux et al. 2014). An average crustal thickness of ~50 km was derived from Mars Orbiter Laser Altimeter data assuming a range of crustal density of 2700–3100 kg/m^3 and considering that the young basaltic shergottites were not representative of the igneous crust (Wieczorek and Zuber 2004). However, the density of martian basalts, irrespective of their age, would be comparable to that of the basaltic shergottites (Baratoux et al. 2014). This leaves us with two possible alternatives: a thick (>100 km) and non-porous basaltic crust, or a thin (~50 km) stratified crust with a non-basaltic and/or porous component (Nimmo and Tanaka 2005; Baratoux et al. 2014). The present-day average crustal thickness is poorly constrained by numerical simulations, with values ranging from several tens of kilometers to more than 100 km, depending on hypotheses made on the heat budget, water content, and mantle rheology (Hauck and Phillips 2002; Breuer and Spohn 2006; Fraeman and Korenaga 2010; Morschhauser et al. 2011). A thick basaltic crust could also match with the moment of inertia factor (Baratoux et al. 2014). However, geoid-topography ratios (Wieczorek and Zuber 2004), rheological constraints (Nimmo and Stevenson 2001), mass balance models based on U–Th and K concentrations (McLennan 2001) or Nd isotopic compositions (Norman 1999), and the early separation of geochemical reservoirs, suggesting the absence of crustal recycling (Mezger et al. 2012) place upper bounds on the crustal thickness that is all below 100 km.

On the other hand, various pieces of evidence for magmatic diversity (e.g., granitoids, anorthosites) have also been offered from remote sensing in small outcrops of the ancient crust, such as central peaks of impact craters (Fig. 22) (Foley et al. 2003; Christensen et al. 2005; Bandfield 2006; Carter and Poulet 2013; Wray et al. 2013). Felsic and alkali-rich igneous rocks (including mugearite, granodiorite, and trachyte) have been identified on float rocks and conglomerate clasts by the Curiosity rover at Gale crater (Stolper et al. 2013; Schmidt et al. 2014; Sautter et al. 2014, 2015). The meteorite breccia NWA 7034 (paired with NWA 7533 and NWA 7475 of similar origin) is a unique piece of ancient crust with zircon crystals dated at 4.43 Gy and contains differentiated felsic rocks with abundant feldspars showing a more complex mineralogy than any other martian meteorites (Agee et al. 2013; Humayun et al. 2013; Wittmann et al. 2015). The significance and representativeness of these samples and remote-sensing observations for the average structure of the crust and their contexts of formation are debated, but it is of note that the existence of a voluminous evolved silica-rich continental-like component, mostly buried below most recent basalts, would offer a simple way to satisfy geophysical observations with other arguments in favor of a relatively thin (~50 km) crust (Baratoux et al. 2014; Sautter et al. 2015, 2016).

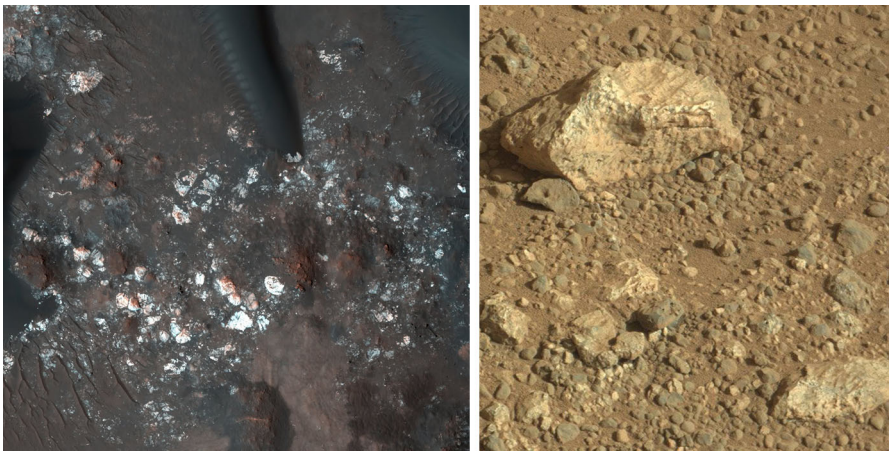

Fig. 22 *Left* HiRISE image of a megabreccia of the central peak of Stokes crater, showing light-toned blocks of excavated crust (NASA/MRO/UA/LPL/HiRISE). *Right* image of leucocratic rocks in the hummocky plains analyzed by the Curiosity rover (NASA/JPL/MSSS/Mastcam)

2.4.4 A magnetized crust

Localized but intense magnetic anomalies have been detected in the southern hemisphere by the magnetic field experiment (MAG/ER) onboard Mars Global Surveyor (Fig. 23) (e.g., Acuna et al. 1999; Connerney et al. 1999, 2001; Purucker et al. 2000; Langlais et al. 2010). The most prominent crustal sources are E–W trending features in Terra Cimmeria and Terra Sirenum, two regions of the southern highlands centered around 180°W. These anomalies present locally stripes, quasi-parallel bands of magnetized crustal rocks somewhat similar, but much larger than those associated with oceanic spreading due to plate tectonics on Earth in the presence of a reversing dipole (Connerney et al. 1999). However, further modeling showed that the anomaly distribution is more complex and may not fit to this simple view. In contrast, a number of isolated anomalies have been interpreted in terms of magnetic source bodies, such as magmatic intrusions, volcanic edifices, or accretion or terranes (e.g., Nimmo 2000; Arkani-Hamed and Olson 2010; Hood and Zakharian 2001; Hood et al. 2003, 2005, 2010; Boutin and Arkani-Hamed 2006; Langlais and Purucker 2007; Lillis et al. 2006, 2008). The lack of current magnetic field and the ancient age of the crust where anomalies were detected point for a cessation of the magnetic field ca. 3.7–4.0 Gy (see Sect. 3.1.7).

These magnetic anomalies are about an order of magnitude larger than those of the Earth crust (obtained at comparable altitude,) suggesting that Mars crust is highly magnetic compared with Earth. Magnetite, ilmenite, and hematite are Fe-rich magnetic minerals that have been proposed to be present in the crust in an abundance sufficient to explain the anomalies (e.g., Kletetschka et al. 2000; Dunlop and Arkani-Hamed 2005), although hematite would require specific oxidizing conditions to exist at depth. An interesting scenario of magnetic mineral enrichment has built on the detection of serpentine in the southern crust by orbital spectrometers (e.g., Murchie et al. 2009).

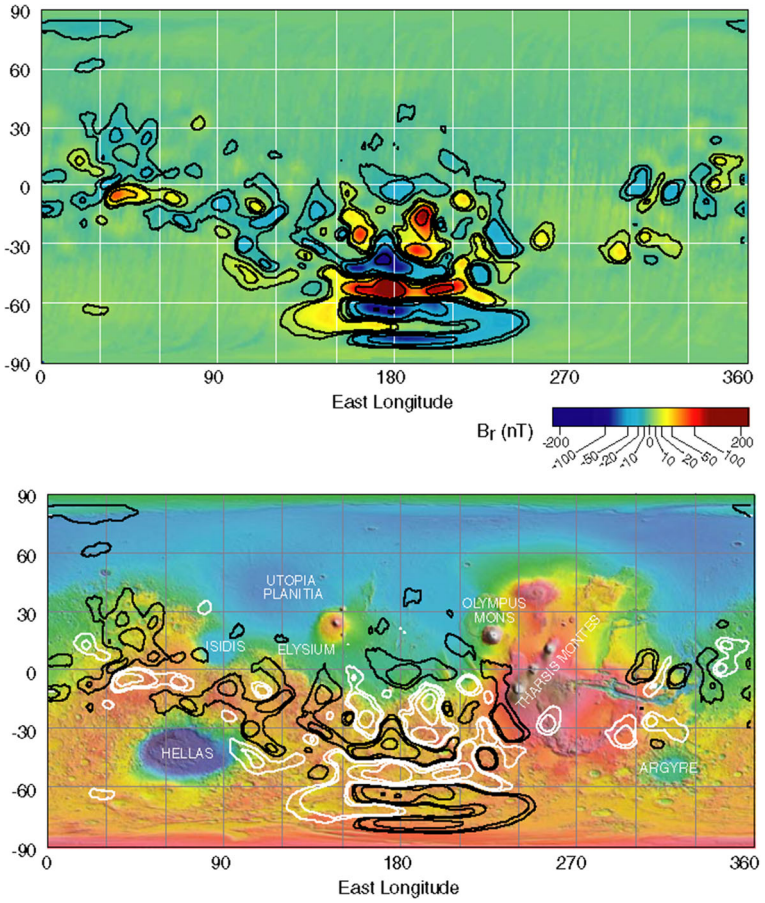

Fig. 23 *Top* the radial component of the field is shown with a *colorbar* scaled to ±220 nT(d) Comparison of radial field contours with MOLA topography. Isomagnetic contours are drawn for $B = \pm 10, 20, 50, 100, 200$ nT. The figures are taken from Connerney et al. (2001)

Indeed, serpentinization is a process of alteration by water that forms magnetite as a by-product. Magnetite, if present in sufficient proportion, may then generate the anomalies observed (Quesnel et al. 2009). Alternatively, pyrrhotite (a Fe-sulfide) has been proposed because of its presence in several martian meteorites (Rochette et al. 2001).

2.5 Deep interior composition and structure

Our knowledge of the interior structure of Mars derives from the geochemical analyses of crustal rock samples, high-pressure experiments exploring the stability of mineral assemblages in the mantle, and from geodetic and geophysical measurements (average density, the moment of inertia, the tidal Love numbers, and tidal dissipation factor, see

Table 3 Main physical parameters of Mars and a range of possible internal structures that satisfy these constraints (values from Rivoldini et al. 2011, and references therein)

Mass (m 10^{23} kg)	6.41855 ± 0.0008
Equatorial radius (R_e km)	3396.2 ± 0.1
Polar radius (R_p km)	3376.2 ± 0.1
Mean radius (R km)	3389.5 ± 0.2
Mean density (kg/m^3)	3934.97 ± 1.2
Polar moment of inertia factor	0.3644 ± 0.0005
Mean moment of inertia factor	0.3645 ± 0.0005
Elastic tidal love number (k_2)	0.159 ± 0.009
Crustal thickness (km)	39–77
Core radius (km)	1729–1859

Table 3), which may be used to constraint the distribution of mass and state of matter (liquid and solid) in the interior (Fig. 24).

2.5.1 Interior composition from martian meteorites and cosmochemical arguments

Following the conclusive evidence of the Martian origin of the Shergottites–Nakhlites–Chassignites (SNC) group of meteorites from isotopic ratio of rare gas trapped in the EETA7901 component matching that of the Martian atmosphere (Bogard and Johnson 1983), Dreibus and Wänke (1985) were the first to use bulk major, minor, and trace elements concentrations in these samples to produce a model of the composition of the primitive martian mantle (i.e., the composition of the mantle before the extraction of the crust corresponds to the average composition of the present mantle + crust system). The model was built based on the assumption that Mn concentration and the bulk concentrations of lithophile elements (e.g., Ca, Al, Cr, and Mg) match the chondritic value when normalized to Si. The concentrations of other elements, which are not in chondritic abundance and are fractionated during magmatic differentiation, are derived from one-to-one correlations of concentrations with elements in chondritic abundance (e.g., K–La and Na–Ga). The mass of the core and its composition were then determined by mass balance, assuming that all Ni, S, and remaining metal Fe enter the composition of the core. This approach suggests that the Mars mantle is enriched in moderately volatile elements (K, Na, and P) and in iron relative to the Earth mantle: the Mg# would be of ~0.75 for Mars, in comparison of 0.9 for the Earth. This difference in partitioning of iron between the silicate mantle and metallic core implies that mass of the martian core is proportionally smaller than that of the Earth. This important characteristic of the martian mantle is actually based on the Fe/Mn ratio in basaltic rocks, which is thought to diagnostic for Mars and on the assumption that Mn concentration in the mantle is chondritic, in contrast with the terrestrial mantle (Dreibus and Wänke 1985). The most recent survey of analyses of Martian meteorites confirms that the Mn/Fe is relatively constant in basaltic Shergottites (Baratoux et al. 2014). However, different values have been reported from in situ analyses of Gusev rocks and soils (McSween et al. 2009), though variations of Fe/Mn ratio in surface rocks may

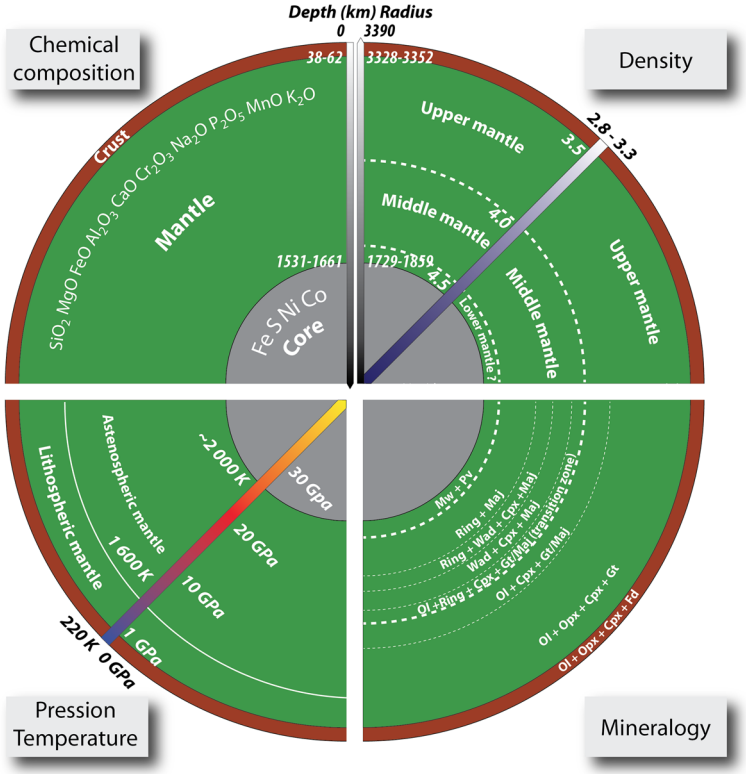

Fig. 24 Internal structure of Mars. *From upper left and counterclockwise*, the chemical composition panel lists the major elements in mantle + crust and core, order by their relative abundance; P–T structure panel with lithosphere/astenosphere boundary; mineralogical structure panel adapted from Bertka and Fei (1997) (*Ol* Olivine, *Opx* Orthopyroxene, *Cpx* Clinopyroxene, *Gt* Garnet, *Maj* Majorite, *Wad* Wadsleyite, *Ring* Ringwoodite, *Mw* Magnetowüstite, *Pv* Perovskite); density structure panel; and main divisions of the mantle, based on its mineralogical structure. Note that the size of the core and its composition are not precisely known, and that the existence of a lower mantle is currently debated

be the result of secondary processes, such as aqueous alteration and oxidation (Lanza et al. 2014).

Sanloup et al. (1999) has produced another class of model based on the assumption that Mars is a mixture of two chondritic components (ordinary chondrites and the EH-chondrites). Their model is constrained by the oxygen isotopic ratio of the SNC meteorites, which is reproduced by a mixture of the two groups of chondrites. It also suggests an iron-rich mantle, with differences regarding the Mg/Si ratio that has consequences on the mantle mineralogy. The validity of the geochemical models was also addressed from laboratory experiments to determine if the elements abundances of martian basalts can be formed through the magmatic differentiation of parent magma derived from mantle partial melting at high pressure (Agee and Draper 2004; Collinet et al. 2015). For instance, Agee and Draper (2004) have shown that it is possible to reproduce the super-chondritic CaO/Al_2O_3 ratio of martian basalts from partial

melting at ∼5 GPa, but find it difficult to match their FeO content. Therefore, they have suggested a lower Fe/Mg ratio for the source of shergottites in comparison with Dreibus and Wänke (1985). Collinet et al. (2015) demonstrated that the parental melt of Adirondack-class basalts of Gusev crater may be produced by ∼25 wt% partial melting of the mantle at 1.5 GPa using Dreibus and Wänke (1985) composition. Despite admitted sources of uncertainties and unknowns, the model of Dreibus and Wänke (1985) still serves as a reference model until today.

2.5.2 Geophysical constraints

The determination of geophysical parameters and, in particular, the first estimation of the moment of inertia factor (MOI) from Earth-based radio tracking observation of the Mars Pathfinder lander (Folkner et al. 1997) were pivotal in the exploration of the martian interior. Geochemical models of the interior were subsequently examined against the geophysical parameters (Sanloup et al. 1999; Longhi et al. 1992; Zharkov and Gudkova 2005). The Monday, October 17, 2016 at 5:11 pm, the initial MOI value of 0.3662 ± 0.0017 of Folkner et al. 1997 was revised by Yoder et al (2003) from the analysis of Mars Global Surveyor radio tracking. The new value of 0.3650 ± 0.0012 is the most accurate value of the MOI of Mars and constrains that at least the outer core is liquid (Yoder et al 2003). The evaluation of geochemical models against geophysical observations requires an assumption for the aerotherm (temperature profile in the mantle and core) and some knowledge of stable mineral assemblages and their thermodynamic properties, which was the objective of high-pressure laboratory experiments (e.g., Bertka and Fei 1997; Spohn et al. 2000). According to such experiments, the upper mantle is composed of olivine + clinopyroxene + orthopyroxene + garnet at pressures up to 9 GPa, with differences on the relative abundance of orthopyroxene and olivine depending on the Mg/Si ratio (Sanloup et al. 1999). Above 9 Pa, the transition zone is characterized by the disappearance of orthopyroxene, the appearance of γ-spinel, and then β-phase. Above 17 GPa, the mantle is dominated by γ-spinel and majorite. The existence of a lower mantle and associated pressure conditions for the stability of perovskite and magnesiowüstite is not certain, and depends on the mantle composition and position of the core-mantle boundary. Several studies have attempted to introduce both geochemical and geophysical constraints to explore the range of possible solutions. For instance, Sohl et al. (2005) have explored the range of acceptable crust thickness, crust density, core thickness, and core density using geophysical constraints and a parameterized iron-dependent average density for the mantle. Their conclusion was in favor of smaller mantle iron content than previously proposed by Dreibus and Wänke (1985). However, Baratoux et al. (2014) have shown that this conclusion is not valid if one considers the density gradient in the mantle, which was neglected by Sohl et al. (2005). Khan and Connolly (2008) has explored a global inversion of the mantle structure, chemical composition, and mineralogy based on geophysical parameters and thermodynamic modeling of stable assemblage in the CaO–FeO–MgO–Al_2O_3–SiO_2 system. This approach confirms the low Mg# of the martian mantle and suggests a (liquid) core radius of ∼1680 km, with a density of 6700 kg/m^3 implying a large S content (>20%) in the core, but concluded that pressure and temperature conditions are insufficient to stabilize perovskite

and magnesiowüstite. Rivoldini et al. (2011) revisited the geodetic and geophysical constraints and have explored the range of plausible internal structure based on the various geochemical models published since the pioneering work of Dreibus and Wänke (1985). Their conclusion favors a liquid core with a radius of 1794 ± 65 km, with a sulfur concentration of 16 ± 2 wt% and a thin layer of perovskite at the bottom of the mantle for the hot mantle scenario. This study also concluded that geophysical/geodetic data alone cannot constrain the chemistry and mineralogy of the mantle.

3 Mars formation and interior evolution

Mars history has been divided in periods and subdivided in epochs useful for geological mapping of its surface. The Noachian (>3.7 Gy) corresponds to the early period coeval to the heavy bombardment, and is divided in three epochs (late, middle, and early). The pre-Noachian has recently been defined as the period before ~4.1 Gy for which no surface observation can provide information (similarly to the Hadean on Earth). The Hesperian (3.0–3.7 Gy divided in the early and late epochs) is a transition in terms of impact crater rate of formation and has been defined as a relatively short time interval because of the large diversity of surface landforms that belong to this period (Tanaka 1986). The most recent period (Amazonian, <3 Gy) is divided in three epochs (late, middle, and early). All these periods are constrained in relative ages (or crater densities) by crater counts and absolute ages are given using models that are extrapolated from the lunar chronology obtained from lunar meteorites (Table 4, Hartmann and Neukum 2001; Werner and Tanaka 2010). While the absolute ages are still under debate (e.g., Werner and Tanaka 2010), crater densities are obtained from statistically meaningful surfaces and act as good stratigraphic markers that are used thoroughly in the literature.

Table 4 Stratigraphic periods of Mars history with ages obtained from crater frequencies (see Werner and Tanaka 2010 for details)

Epochs	Start age of the epoch (Gy, derived from Ivanov 2001 model)	Start age of the epoch (Gy, derived from Hartmann 2005 model)
Late Amazonian	0.39	0.23
Middle Amazonian	1.45	0.88
Early Amazonian	3.46	3.00
Late Hesperian	3.65	3.40
Early Hesperian	3.74	3.57
Late Noachian	3.86	3.85
Middle Noachian	3.97	3.96
Early Noachian	>3.97	>3.96

3.1 From accretion to differentiation and the early crust evolution

3.1.1 Accretion and core-mantle differentiation

The accretion of Mars, as for the other terrestrial planets, started with the condensation of tiny solid particles (dust) from a cooling gas of near-solar composition. Dust agglomerates coalesced into rapidly growing planetesimals (1–1000 km in diameter). Subsequent growth of planetesimals led to the formation of planetary embryos. Heat transfer from the surface to interior occurred from conversation of the kinetic energy of the accreted material (Tonks and Melosh 1993). In addition, internal heating by short-lived isotopes (e.g., ^{26}Al, ^{60}Fe) was possible if accretion took place during a period comparable with the half-lives of these isotopes (∼1–2 Myrs, e.g., Nimmo and Kleine 2007; Dauphas and Pourmand 2011). The segregation of a metallic core took place when the planet was at least partially molten to allow for a segregation of a heavy metallic liquid from a lighter silicate melt. Mars is considered to be representative of this early stage of planetary accretion (Chambers and Wetherill 1998; Harper et al. 1995; Lee and Halliday 1997), whereas the Earth (and the moon) resulted from multiple collisions between these planetary embryos and a protracted accretion over more than 50 My (Canup and Asphaug 2001; Touboul et al. 2007). The early migration of Jupiter and Saturn may have been involved in limiting further growth of Mars (Walsh et al. 2011; Brasser 2012). Using the ^{182}Hf-^{182}W system (half-life of 9 My), Dauphas and Pourmand (2011) were able to place the tightest constraint on the timing of Mars accretion and core formation. They have produced a more precise estimate of the bulk silicate Hf/W with respect to the previous studies (Nimmo and Kleine 2007) from the observations that the Th/W ratio is constant in Martian meteorites. Armed with this information, they have determined that the metallic core of Mars formed in 2–4 My after the Solar system began to form. This age implies that both kinetic energy from impact and decay of ^{26}Al contributed to the initial heating of the planet. It appears, therefore, inescapable that silicate and metal melting temperatures were globally achieved (magma ocean) before the end of accretion. The depletion of highly siderophile elements (HSE) with respect to chondritic abundance in the Martian mantle as recorded in the Martian meteorites is another piece of evidence for the existence of a magma ocean (Birck and Allègre 1994; Jones et al. 2003; Treiman et al. 1986; Brandon et al. 2000). Indeed, efficient separation of a metallic melt from molten silicate is only possible if Mars had a large-scale magma ocean.

3.1.2 The late veneer

As for the Earth mantle, the depletion of HSE appears to be not as marked as one would expect from their respective metal-silicate partition coefficient (Jones et al. 2003; Walker 2009; Brandon et al. 2012). In addition, their respective concentration follows a near chondritic signature suggesting that they have not been fractionated from each other. Several hypotheses have been explored to explain this apparent excess of HSE on the Earth, including inefficient core formation, metal-silicate equilibration at high pressures and temperatures, and the addition of material with chondritic bulk compositions (late veneer) (e.g., Rubie et al. 2007). Synthesis of the large database

now available for HSE in the terrestrial mantle (including also lunar samples) reveals that each of the main hypotheses has flaws. For instance, the relatively high HSE abundances in both planets' mantles cannot be accounted for by high pressure–temperature metal–silicate partitioning at the bases of magma oceans (Brandon et al. 2012). The late veneer hypothesis is more widely accepted, though hybrid models may be necessary to account for all the observed HSE characteristics (Walker 2009). On Mars, the late veneer event should take place in a restricted time window after the formation of the core and before the crystallization of the magma ocean (Brandon et al. 2012).

3.1.3 Magma ocean crystallization and silicate differentiation

The subsequent scenario of the evolution of the martian magma ocean is based on theoretical and geochemical grounds. The solidification of the convecting magma ocean on large planets starts at the bottom and progresses upward, because the solidus and adiabat intersect at depth (Walker et al. 1975; Solomatov 2000). Its crystallization history and subsequent evolution would appear to mainly depend on planet's size (Elkins-Tanton 2012). On the moon, the crystallization of light plagioclase is thought to have formed a floatation crust, which is today exposed as the lunar highlands (Wood et al. 1970; Smith et al. 1970). However, this mechanism only operates if plagioclase appears early enough in the crystallization sequence of the magma ocean to be able to move upward. On Mars, unlike on the moon, the presence of water and the higher lithostatic pressure gradient would inhibit the crystallization of plagioclase and the formation of a floatation crust (Elkins-Tanton et al. 2005). Simple models for fractional magma ocean crystallization neglecting the complexity of crystal growth and entrainment of suspended solids predict a solid cumulate stratigraphy (Elkins-Tanton et al. 2003, 2005). Since the Fe–Mg exchange coefficients in dominant mineral species are lower than one, late materials to crystallize have high Mg# number and are denser than the early cumulates. This cumulate stratigraphy is unstable and should naturally overturn via solid-state Rayleigh Taylor instabilities (Hess and Parmentier 1995; Elkins-Tanton et al. 2005). Partial melts could have been also extracted during this mantle overturn (Elkins-Tanton et al. 2005) and have contributed to crustal extraction, though it is not clear if such crustal products have been preserved until present.

The solidification of the magma ocean, according to the fractional crystallization scenario, created a stable stratified mantle and chemical heterogeneities manifested in the heterogeneous $^{182}W/^{184}W$ and $^{142}Nd/^{144}Nd$ isotopic composition observed in different groups of martian meteorites. These isotope anomalies imply major chemical fractionation within the Martian mantle during the lifetime of the short-lived isotopes ^{146}Sm and ^{182}Hf, i.e., within approximately the first 100 My of Solar System history (Harper et al. 1995; Kleine et al. 2004; Debaille et al. 2007, 2009). In contrast to Earth (e.g., Hofmann et al. 1986), the early formed chemical heterogeneities are still preserved on Mars, albeit slightly modified by mixing processes. The preservation of such ancient chemical differences is possible if Mars did not undergo efficient whole mantle convection or vigorous plate tectonic style processes after the first few tens of millions of years of its history. Tosi et al. (2013) explore the consequence of the fractional crystallization and mantle overturn scenario proposed by Elkins-Tanton et al. (2005) and found that no thermal or chemical mantle convection is likely to

have occurred throughout most of Mars' history, providing a suitable explanation for the long-term preservation of isotopic heterogeneities. However, this scenario is not consistent with the surface record of volcanic activity, and in particular with the evidence for the early volcanism (Xiao et al. 2012; Baratoux et al. 2013) and late volcanism (e.g., Plescia 1990; Neukum et al. 2004; Vaucher et al. 2009) and for igneous diversity during the early Mars (Wray et al. 2013; Carter and Poulet 2013; Baratoux et al. 2014; Sautter et al. 2014, 2015). Indeed, the evidence for a long-term evolution of the crust-mantle system suggests mantle or crust melting events associated with thermal anomalies or adiabatic decompression. Absence or limited convection would be also difficult to reconcile with evidence for progressive cooling of the interior (Ruiz et al. 2011; Baratoux et al. 2011; Grott et al. 2013; Filiberto and Dasgupta 2015). Further work is, therefore, needed to reconcile the preservation of geochemical reservoirs with multiple pieces of evidence for the early and prolonged volcanic activity, involving large-scale convection in the mantle.

3.1.4 The fate of volatiles

Mars is thought to have incorporated more volatiles than the earth during accretion. The orbital exploration of Mars has also repeatedly identified compelling evidence for a volatile-rich crust. Formation and early evolution of the crust likely involve significant degassing of the martian mantle (Jaskosky and Jones 1997; Filiberto et al. 2016). In the absence of a mechanism for replenishment of the mantle in volatile species, it is usually considered that the present-day mantle is essentially dry, though even minor volatile concentration may have important consequences on the subsequent evolution (e.g., mantle rheology is sensitive to water levels at the level of ∼100 ppm, Morschhauser et al. 2011)

3.1.5 Crustal dichotomy

A major and one of the most ancient features of the martian crust is its hemispheric dichotomy (Fig. 21). It corresponds to a change in crustal thickness and average elevation between the southern (highland crust) and northern hemisphere (lowland crust) that was likely acquired short after the crystallization of the magma ocean. Buried impact basins in the northern lowlands suggest that the lowland crust formed more or less contemporaneously with the highland crust (Frey 2006). This difference in crustal thickness appears to be isostatically compensated. The origin of the hemispheric dichotomy is unclear and could have involved either a giant impact (Wilhelms and Squyres 1984; Frey and Schultz 1988; Andrews-Hanna et al. 2008) or mantle convection (Zhong and Zuber 2001; Roberts and Zhong 2006; Elkins-Tanton et al. 2005; Debaille et al. 2009).

3.1.6 Late heavy bombardment (LHB)

Subsequent evolution of the crust between end of accretion and the Noachian period (>4 Gy) is poorly documented, since no exposure of surfaces older than 4.15 Ga exists, based on crater count statistics (Werner 2008, see also Sect. 3.2). Nevertheless, this

period is likely characterized by intense and global volcanism and impact cratering. Major impact basins have been formed around 4 Gy ago, and analyses of impact basins suggest a similar evolution of the heavy bombardment period on the Moon and Mars, whereas the oldest martian basins may have been erased by endogenic processes (Frey 2008; Werner 2008).

3.1.7 What does the remnant magnetic field tell us about Mars interior evolution?

The presence of crustal magnetic anomalies (Sect. 2.4.4, Fig. 23) proves that a dynamo was active in the liquid core, once in the past. The northern lowlands, as well as several the giant basins, are devoid of significant anomalies, suggesting an early magnetic field cessation on in the Noachian before the last giant impacts that would have reset the crust (e.g., Shahnas and Arkani-Hamed 2007). However, the exact timing of the cessation remains debated because of the presence of anomalies related to post-Noachian volcanism, such as the volcano Apollinaris Patera (Langlais and Purucker 2007; Milbury and Schubert 2010). Another explanation for the lack of anomalies in the northern plains invokes an asymmetry in the dynamo itself (Amit et al. 2011). Such a past hemispherical dynamo could be the result of the giant impact that formed the dichotomy earlier (Monteux et al. 2013; Monteux and Arkani-Hamed 2014). In general, the giant impacts may have had a strong effect on the dynamo by creating a thermal stratification interrupting the dynamo for a 100–200-My period, before it may have started again (Arkani-Hamed and Olson 2010; Monteux and Arkani-Hamed 2014). Thus, no definitive consensus exists with respect to the cessation of the dynamo or even its continuous activity during the first billion years of Mars existence.

3.2 Volcanic and tectonic evolution

3.2.1 Volcanic activity through time from surface imagery and topography

Crustal production as a function of time, and more generally the timing of growth of major volcanic provinces are difficult to constrain, as new volcanic products cover ancient surfaces. Volcanism is observed both as flat plains and infilled basins (formed by effusive volcanism) and local edifices, historically classed as *Montes*, *Tholii*, and *Paterae* from their overall shape. Montes (such as Olympus Mons or Elysium Mons) are larger and higher than Tholii (such as Hecates Tholus), whereas Paterae (such as Nili Patera or Alba Patera) are large but shallow volcanoes (Patera means flat saucer in latin). While Tholii and Montes have overall shape consistent with a predominance of effusive volcanism, Paterae display a large diversity of volcanic processes, including pyroclastic activity (e.g., Wilson and Head 1994; Plescia 2004; Williams et al. 2009), so these classes of volcanoes should not been necessarily assimilated with given volcanic processes.

Noachian period

The Tharsis volcanic province, 3000 × 3000 km in extent and at 5–10 km in average elevation, is the major volcanic province on Mars. It is estimated that 3×10^8 km^3 of volcanic rocks were emplaced, beginning in the Noachian (Phillips et al. 2001). Outside

of the Tharsis bulge, ancient edifices (Noachian age >3.7 Gy) have been found in the ancient highlands using topography and morphology (Xiao et al. 2012), but a little is known about their origin and mineralogy. The apparent paucity of recognizable volcanic landforms of Noachian age most likely reflects the difficulty in identifying them due to high erosion rates in this period and the destruction or burial of these surfaces by subsequent impact craters, tectonic, and volcanic activity.

Hesperian period
Estimates for crustal growth from surface exposure ages (inferred from crater counts) suggest that volcanic activity peaked in the Hesperian (Greeley and Schneid 1991b; Grott et al. 2013), but the existence of such a peak should be taken with caution in light of the inherent difficulty in estimating the crustal production rate during the Noachian. The ubiquitous Hesperian volcanism (3–3.7 Gy) is manifested predominantly as broad plains (Syrtis Major Planum, Hesperia Planum and other Circum-Hellas volcanic provinces, typically reaching 10^6 km^2 in area) likely due to flood volcanism (analogous to lunar mare). Plain-style volcanism has affected both the topographic lows of the northern hemisphere and the highlands south of the hemispheric dichotomy (Carr 1973; Greeley and Spudis 1981; Head et al. 2002; Salvatore et al. 2010; Hiesinger and Head 2004; Williams et al. 2009).

Amazonian period
The Amazonian era (<3 Gy) appears to be dominated by effusive volcanism geographically limited to several regions, including Tharsis, Elysium, and Amazonis Planitia (Fig. 25). This period is marked by activity of giant shield volcanoes (Olympus Mons, Elysium Mons, Arsia Mons) that are up to 500 km in diameter and 25 km in height, and formation of numerous smaller shield volcanoes (Plescia 1990; Hauber et al. 2009, 2011; Vaucher et al. 2009; Baratoux et al. 2009; Platz and Michael 2011) and local explosive activity (e.g., Hauber et al. 2005). Shield volcanoes (typically 5-10° in average slope) have been fed by continuous magmatism over millions of years, providing evidence for static lithosphere (e.g., Carr 1973). Evidence for episodic volcanic activity until recent time (<100 My) at Olympus Mons, Amazonis Planitia, and South Elysium Planitia (Plescia 1990; Jaeger et al. 2007; Neukum et al. 2004; Vaucher et al. 2009) suggests that Mars may be still volcanically and tectonically active. This morphology of lava flows observed in the Amazonian era is generally consistent with the rheological properties of iron-rich tholeiitic to alkaline basalts (Chevrel et al. 2013a, b).

3.2.2 Tectonic activity

Although plate tectonics has been proposed to explain some characteristics of the Tharsis bulge (Courtillot et al. 1975; Sleep 1994), it is now admitted that the crust-mantle system has evolved in a stagnant-lid regime (one-plate planet) over most of its history (Golombek and Phillips 2009; Grott et al. 2013), whereas the earliest period of Mars (<4.1 Gy) is still open to debate. The consequence is that the style of deformation observed at the surface is far different from those observed on Earth due to plate tectonics, with the Tharsis bulge playing a major role on the global shape and

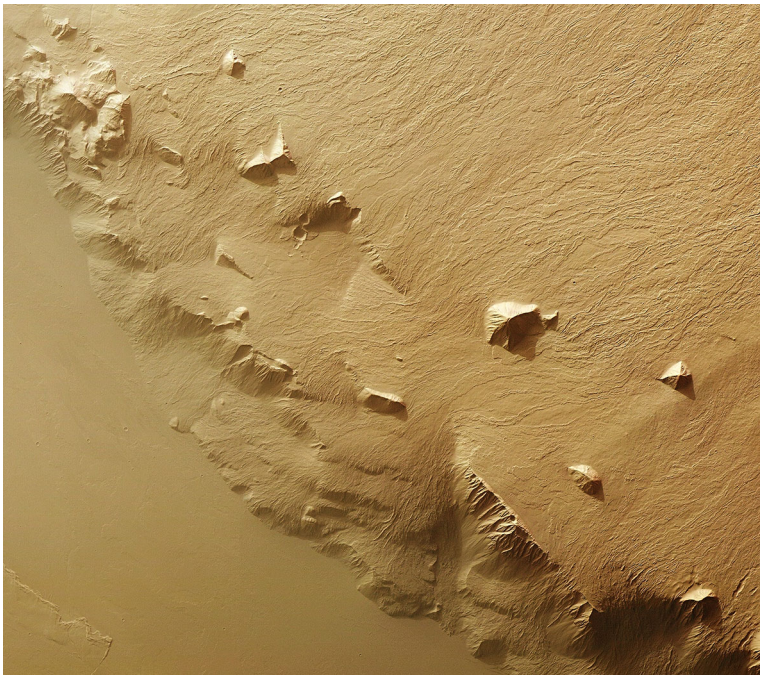

Fig. 25 Accumulation of lava flows at the foot of the Olympus Mons 25-km-high volcano (ESA/HRSC/Mars Express/Neukum)

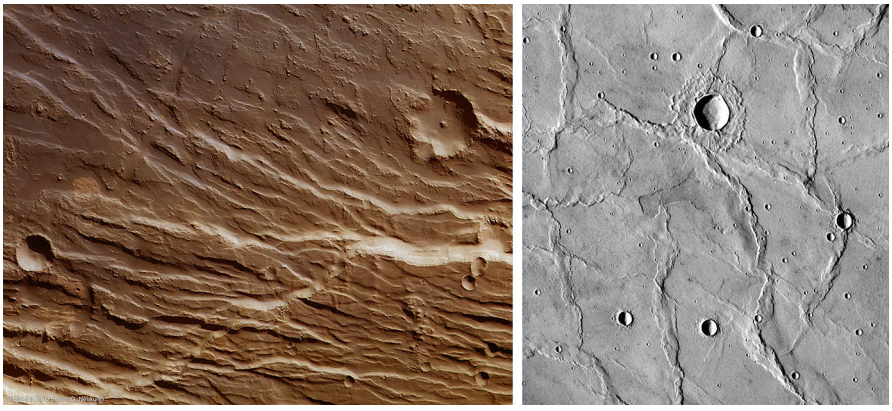

Fig. 26 *Left* series of normal faults (grabens) radial to Tharsis bulge. *Right* wrinkle ridges in Hesperia Planum formed by isotropic compressive stress (ESA/HRSC/Mars Express/Neukum)

deformation observed, enabling large volcanoes to form in the absence of moving plates (e.g., Carr 1973).

At local scale, however, normal and thrust faults typical of brittle deformation reveal the presence of stresses induced by some kind of tectonic activity (Fig. 26). Normal faults develop as grabens and horsts (1–10 km in width and 10–500 km in length) that

are present uniquely on the Tharsis bulge, with directions radial to the bulge center. Cross-cutting relationships show that they formed according to a minimum of six episodes, with intense activity in the Noachian and more local episodes around major volcanoes in the Amazonian (Tanaka et al. 1991; Banerdt et al. 1992; Golombek et al. 1996; Anderson et al. 2001). The Valles Marineris canyon (3000 km long, 8 km in depth) is a major feature inside the Tharsis bulge. It was likely initiated by similar normal faulting in the Early Hesperian. Valles Marineris has been interpreted as an aborted rift by analogy to African rift systems on Earth (Masson 1977; Mège and Masson 1996). Nevertheless, the full depth may be explained only by episodes of collapse and mass wasting that enlarged the initial faults into canyons rather than pure fault displacement (Lucchitta et al. 1992; Schultz 1998; Andrews-Hanna 2012).

Wrinkle ridges are elongated, sinuous structures of 100–500 m in height and several tens of kilometers in length (Fig. 26, right). They have been interpreted as the result of compressive stresses (Golombek et al. 2001; Golombek and Phillips 2009). A variety of mechanical models have been proposed to explain their specific shape, including crustal thrust faults, buckling of the crust, shallow detachments, and fold-propagation thrust faults (Watters 1993, 2003; Mangold et al. 1998; Schultz 2000; Golombek et al. 2001). Wrinkle ridges are present around the Tharsis bulge in a circumferential orientation, thus in a direction consistent with the main stress that produces normal faults that are oriented orthogonally (radial to Tharsis). However, these structures formed mainly during a single phase at the end of the Hesperian (Mangold et al. 2000). They are also present across the whole planet, in most Hesperian plains, and in Noachian highlands. Their ubiquity and coeval formation period for many of them (Late Hesperian) suggests a relationship with a global stress that may be related to the secular cooling of the planet and not only the presence of Tharsis bulge (Chicarro et al. 1985; Mangold et al. 2000; Nahm and Schultz 2010; Beuthe 2010).

At a planetary scale, the excess of mass of the Tharsis volcanism was also capable to globally deforming the lithosphere (Banerdt et al. 1992), as observed from the huge density of radial faults. Tharsis activity has influenced the surface topography (Phillips et al. 2001) and could have induced true-polar wander if it formed outside of its present near-equatorial location (Grimm and Solomon 1986; Zhong 2009). Phillips et al. (2001) concluded that the growth of Tharsis in the Noachian has influenced the direction of valley networks (see Sect. 4.1.1). However, Bouley et al. (2016) have shown that the load of Tharsis is not required to explain the direction of valley networks. In contrast, this study reveals that valley networks are distributed along a circle tilted with respect to the equator, and proposes that this distribution is best explained if they formed before the true-polar wander driven by the growth of Tharsis (Bouley et al. 2016). The revised chronology of Tharsis suggests that a significant crustal growth extended into the Hesperian eras. Arguments in favor of significant post-Noachian crustal additions and associated true-polar wander were also proposed by Perron et al. (2007) and Kite et al. (2009). The latter study suggests a movement significantly smaller in amplitude than described in Bouley et al. (2016) as a result of the eruption of late Hesperian and Amazonian lavas in the northern hemisphere of Mars.

3.2.3 Constraints on volcanism from chemistry and mineralogy

Volcanic and tectonic activities are surface expressions of heat and mass transfer in the crust-mantle system, and are essentially controlled by the abundance and distribution of three naturally radioactive isotopes (^{40}K, ^{232}Th, and ^{238}U) usually called heat-producing elements (HPE). Present surface heat flow depends on the initial energy budget, history of crust-mantle partitioning of HPE, and of the mantle heat production divided by heat losses (Urey ratio, representing efficiency of heat transfer to the surface). On the Earth, the evolution of the planetary interior is constrained by present heat-flow measurements and petrologic constraints on the thermal evolution of the mantle (e.g., Herzberg et al. 2010). In the absence of direct heat-flow measurements on Mars, the present surface heat flow is unknown and the partitioning of HPE in the crust and mantle is poorly constrained. Surface heat-flow maps have been produced assuming that (1) observed surface concentrations K and Th are representative of the crust, (2) a chondritic Th/U ratio of 3.8 and (3) a chondritic abundance of HPE in the primitive mantle, and (4) a present Urey ratio of 0.7. Such calculations produce a surface heat flow in the 20–30 mW/m^3 range, with a crustal contribution of ∼6–7 mW/m^3 (Hahn et al. 2007; Grott et al. 2013). However, these values may be taken with caution, as the current degree of imbalance between heat production and heat losses is not known, whereas the new pieces of evidence for igneous diversity on the early Mars may invalidate the idea that surface HPE concentrations (in basalts) are representative of a ∼50-km-thick crust, not necessarily basaltic in composition (see Sect. 2.4).

The evolution of the thermal state of the martian mantle may be deciphered from analysis of the deformation associated with lithospheric loads or from the depth of the brittle-ductile transition beneath large faults (e.g., Schultz and Watters 2001; McGovern et al. 2002; Grott 2005; Belleguic et al. 2005; Ruiz et al. 2008, 2009, 2011). This approach provides an indirect estimate of surface heat flow at the time of loading or faulting of the elastic lithosphere, but their interpretation is also hampered by the possible existence of large heterogeneities (e.g., Grott and Breuer 2010; Phillips et al. 2008). Together, these results indicate that Mars has been losing heat (heat loss > heat production) for a substantial part of its history, especially in the Hesperian and to a lesser extent in the Amazonian periods. Although the last volcanic phases are recent and indicate a warm interior, the thickness of the present lithosphere (100–300 km) and the existence of felsic crustal components may represent a significant obstacle for the ascent of partial melts.

Systematic evolution of surface concentrations of K, Th, and Fe with time was noticed in global analyses of Gamma Ray Spectrometer data (Hahn et al. 2007; Karunatillake et al. 2009), but these studies fail to decipher the respective role of primary and secondary processes in explaining these variations. Baratoux et al. (2011) revisited this dataset and have provided evidence that systematic variations with time on Si, Fe, and Th concentrations on volcanic provinces were compatible with globally evolving conditions of partial melting related to the cooling of the mantle and to the thickening of the lithosphere. Estimates for the mantle potential temperatures from in situ chemical analyses at Gusev and Meridiani (Filiberto and Dasgupta 2011, 2015) are also consistent with convective cooling of the interior of Mars. The predominance

of pyroxene-rich olivine-bearing volcanic rocks in the Hesperian (Ody et al. 2013; Musselwhite et al. 2006) and the evolution of pyroxene composition with time, characterized by a relative increase of the Ca-rich species relative to Ca-poor species, can be also interpreted in this framework (Baratoux et al. 2013). However, the comparison of mantle potential temperature from in situ analyses, martian meteorite, and remote-sensing data is not straightforward. In addition, the mantle is assumed to be dry and chemically homogeneous in these studies, whereas the mantle is known to be chemically heterogeneous (Halliday et al. 2001; Mezger et al. 2012), and volatiles (water, F, and Cl in particular) are known to affect melting reactions and solidus temperature (Médard and Grove 2006; Balta and McSween 2013; Tuff et al. 2013; Filiberto et al. 2016). In this respect, morphologic characteristics of Amazonian basaltic shield volcanoes are consistent with effusive volcanism (Plescia 2004; Schumacher and Breuer 2007), whereas highland edifices and the thermophysical properties of ancient crust indicate large presence of volcaniclastic rocks formed by explosive activity linked to higher volatile content in the mantle (Bandfield et al. 2013). Furthermore, it is not clear in which cases the inferred mantle potential temperatures reflect thermal anomalies (hot spots) or the ambient mantle, which complicates the identification and quantification of the global cooling of the martian interior using the petrological approach.

The recent finding of alkaline Noachian rocks and granodiorite at Gale crater (Sautter et al. 2014, 2015) as well as the felsic clasts in the newly found meteorite breccia NWA 7034/7533/7475 (Humayun et al. 2013) suggest that the simple scenario of extraction of a basaltic crust associated with simple convective cooling of the mantle over time may not be extrapolated back to the Noachian era. Orbital and in situ data provide evidence for more magmatic diversity in the Noachian era than in more recent times (Christensen et al. 2005; Rogers and Fergason 2011; Flahaut et al. 2012; Wray et al. 2013; Carter and Poulet 2013; Pan et al. 2015; Sautter et al. 2015). This may include lithologies close to the terrestrial continental crust suggesting geodynamical contexts favorable to partial melting of the basaltic crust (Baratoux et al. 2014; Sautter et al. 2015, 2016). It is also not yet clear if all these early crust components are characteristic products of the Noachian volcanic activity or if some of them may be attributed to preserved remnants of the crystallization of the magma ocean and/or of the melting induced by the expected mantle overturn (e.g., Elkins-Tanton et al. 2005).

3.3 Implications of the interior evolution to the atmosphere and surface evolution

Coupling between atmosphere, crust, mantle, and core evolution has been well documented for the Earth, as a system, and is an important feature of all rocky planets (Foley and Driscoll 2016). The volatile concentrations of the mantle source and the volume of magma reaching the surface (effusion rate) determine the amount of volatile species that have been released in the atmosphere as a function of time. In the absence of plate tectonics, the convecting mantle below the stagnant lid depletes continuously with time, as there is no mechanism to replenish the mantle with volatiles (Morschhauser et al. 2011). Intense degassing likely took place during the formation and crystallization of the magma ocean. The composition and pressure of this primitive atmosphere are

determined by the degassing of the primitive mantle, the input of volatiles associated with bombardement, the partial removal of this atmosphere by large impacts (Melosh and Vickery 1989), and the thermodynamic equilibrium between the atmosphere and the surface of the magma ocean with volatiles dissolved up to the saturation limits of the magma. Modeling of atmospheric growth linked to magma ocean solidification on Mars leads to a CO_2–H_2O dominated atmosphere, with water oceans and surface pressure in excess of 100 bars (Elkins-Tanton 2008).

Various causes of atmospheric espaces make it difficult to preserve the primordial atmosphere, especially after the cessation of the internal magnetic field (Lammer 2013). In this respect, the timing of the cessation of the dynamo is a fundamental question linked to the early evolution of the atmosphere and to the fate of liquid water at the surface (see Sect. 4). Noachian and Hesperian volcanism have likely contributed atmospheric composition and surface pressure (up to 0.8 bar, Craddock and Greeley 2009). In this respect, the timing of the massive release of volatiles association with the growth of volcanic provinces, such as Tharsis, has been linked to global change in surface conditions with precipitation of sulfates (Bibring et al. 2006), or to stability of liquid water during valley networks incision (Brakenridge et al. 1985; Gulick and Baker 1990; Gulick 1993; Gulick et al. 1997; Baker et al. 2007; Bouley et al. 2016). This period is characterized by the formation and evolution of a secondary atmosphere as the results of a complex interplay between non-thermal escape processes, volcanic degassing, impact processes, and surface precipitation of volatiles-bearing phases. Mass transfer associated with internal movement, tectonic, or volcanic activities has affected the inertia tensor of Mars throughout its interior history, and has likely induced several episodes of True Polar Wander resulting in profound modification of local surface conditions, topography (Perron et al. 2007; Matsuyama and Manga 2010) climate, and the stability of surface-ice or water reservoirs (Kite et al. 2009; Bouley et al. 2016). The present 6 mbars atmosphere may have been influenced by prolonged volcanic activity and CO_2 release during the Amazonian (Gillmann et al. 2011), though such calculations are hampered by limited constraints on the concentration of volatiles in martian basalts (Filiberto et al. 2016).

4 Climate evolution and surface processes

4.1 Early Mars aqueous history

4.1.1 Fluvial landforms

In 1972, images from the Mariner 9 spacecraft revealed the existence of dried valley networks, mostly located in the old cratered terrains. Most of them are strongly ramified and some extend over a 1000 km (Milton 1973). This was the first indication that abundant water might have flooded on the surface in the early history of Mars. Other possible sources (aeolian erosion and liquid CO_2 flooding) were also envisaged at that time, but were later discarded. At the same time, outflow channels were discovered in more recent terrains, like Chryse Planitia, east of Valles Marineris. They were interpreted as the signature of violent, episodic floods, possibly due to the rupture

of sub-surface reservoirs under high artesian pressure (Carr 1995, 1996). These two types of landforms still define two end-members in martian fluvial activity.

Detailed analyses of fluvial landforms on Mars have been achieved thanks to recent data, especially topography and high-resolution imagery. Fluvial valleys incising into the martian highlands >3.5 Gy ago display the most developed networks (Hynek and Phillips 2001; Craddock and Howard 2002; Ansan and Mangold 2006; Fassett and Head 2008). These valley networks are often >1000 km in length and present drainage densities up to 0.1–1 km^{-1} similar to those found on Earth in semi-arid regions (e.g., Carr and Chuang 1997; Stepinski and Stepinski 2005; Barnhart et al. 2009; Hynek et al. 2010; Ansan et al. 2008). Dense valley networks have a Hack exponent ca. 0.5–0.7 (Ansan and Mangold 2013) similar to values found on Earth for this parameter, which link watershed area and river geometry (Dietrich and Montgomery 1998). Morphometric parameters demonstrate that dendritic valleys were formed by precipitation, either from rainfall or from snow deposition and subsequent melting (Fig. 27a). In contrast, elongated valleys observed on volcanic plateaus with much less dendritic geometry (e.g., Nanedi Vallis, Fig. 27b) have a shape similar to sapping valleys interpreted on Earth by sub-surface flows rather than precipitation (Carr and Chuang 1997). However, it has been shown that sapping valleys (both on Earth and Mars) require surface flows and a recharge of aquifers (Howard 1988; Grant 2000; Williams and Phillips 2001). These valleys are interpreted to be controlled by a distinct lithology of permeable lava plateaus (e.g., Harrison and Grimm 2005; Mangold et al. 2008a).

On Earth, the time needed for the development of dendritic valleys varies from 10^4 to 10^7 years depending on the lithology of the bedrock (Leopold et al. 1972). More understanding of the hydrology of these former streams is limited by the identification of preserved inner channels—the location where the water flowed—because of the thick aeolian blanket that fill most valleys. When visible, the geometry of the 100–200-m-wide channels identified indicates flow discharge rates of the order of 10^3–10^4 $m^3\,s^{-1}$; a magnitude similar to rivers in this size ranges on Earth (Carr and Malin 2000; Irwin et al. 2005; Jaumann et al. 2005).

While valley networks are widespread in the ancient highlands of Mars, (e.g., Craddock and Howard 2002; Fassett and Head 2008), several valleys cut into Hesperian terrains reactivating older valleys or forming new ones showing that the fluvial activity extended into the Hesperian period (~3.7–3.0 Gy) (e.g., Mangold et al. 2004b; Bouley et al. 2010). A few more valleys can be found in the Amazonian terrains (<3 Gy). However, the latter are much shallower (<50 m deep) and less developed (<100 km long) (e.g., Gulick and Baker 1990; Ansan and Mangold 2013). They are also more patchy and located around specific features, such as volcanoes (Alba Patera, Ceraunius Tholus) or impact craters (e.g., Cerulli, Lyot, Hale craters) suggesting relationships with these heat sources (Fig. 27c, d) (Gulick and Baker 1990; Dickson et al. 2009; Jones et al. 2011). In addition, many of these relatively young features are found in the mid-latitude bands, typically 30°–50° of latitude in both hemispheres, where massive ice deposits have been interpreted to have formed (e.g., Kreslavsky and Head 2002; Head and Marchant 2003), suggesting that these valleys developed through local/transient melting of ice (Fassett et al. 2010; Mangold 2012; Mangold et al. 2012b).

Outflow channels were defined as "channels", because the overall shape of the fluvial valley is dominated by landforms typical of channel erosion, such as grooves,

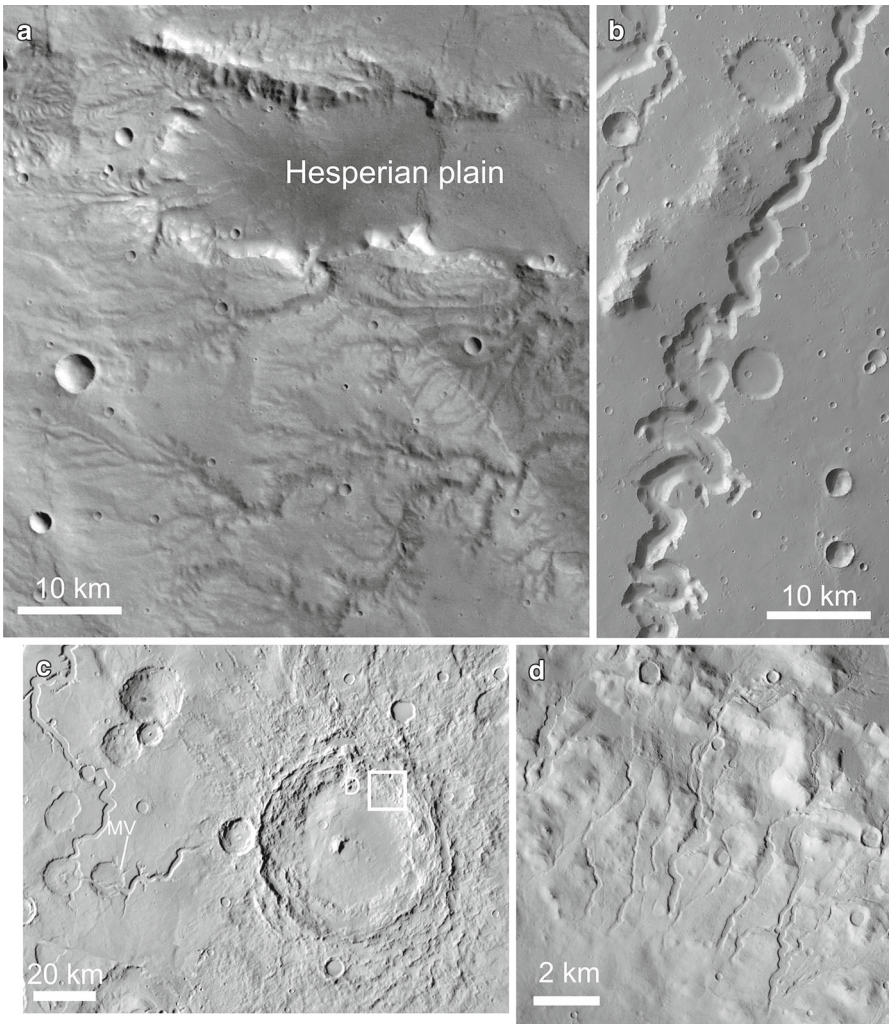

Fig. 27 Image of three different types of valleys at the same scale. **a** Image (HRSC/Mars Express orbit 532) of well-developed valley networks in the Noachian highlands. The volcanic Hesperian plain embays the lower part of these valleys as often observed on Mars. **b** Nanedi Vallis (HRSC/Mars Express image 642) incises through a thick volcanic plateau. The sinuous shape and the presence of inner channels visible on higher resolution image indicate a sustained flow rather than a catastrophic flow. **c** Image (HRSC Mars Express orbit) of Cerulli crater. The *crater* shows fresh ejecta which bury the older Mamers Vallis (MV, a valley similar to Nanedi Valles). Local flows postdating the formation of the crater can be observed on the inner rim of this crater (**d**)

bars, terraces, etc. (Fig. 28). For classical rivers, the valley is an order of magnitude larger than the channel itself. Outflow channels have thus been carved by gigantic flows that occupied their entire floor, reaching up to tens of kilometers in width and tens of meters in thickness over several hundreds of kilometers in length (e.g., Baker and Kochel 1979; Komar 1979; Komatsu and Baker 1997). While a large series of

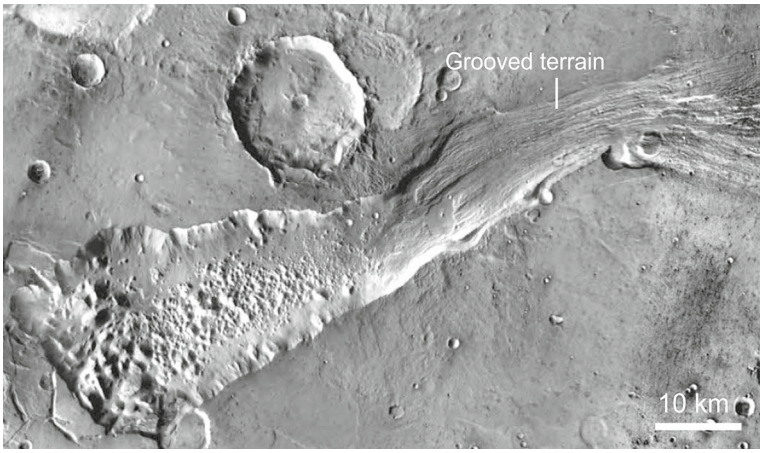

Fig. 28 Ravi Vallis, east of the Valles Marineris region, is an outflow channel with a chaotic source region and grooved terrains indicating strong erosion and quick discharges of particles-laden flows (NASA/Mars Odyssey/ASU/THEMIS)

outflows is present in Xanthe Terra east of the Tharsis bulge, where they are dated to the Late Hesperian epoch, outflows have also been identified in various Amazonian terrains, especially in close connection with volcanoes (Dao Valles near Hadriarca Patera, Hrad Vallis near Elysium Mons) or dikes (Mangala Valles, Athabasca Valles) (Burr et al. 2002; Chapman et al. 2010). Athabasca Valles is a fascinating example, because it is connected to one of the most recent volcanically active areas, Cerberus Fossae, that is dated to have been active within a few tens of millions years (Plescia 1990; Burr et al. 2002; Vaucher et al. 2009). This example, in particular, has been used to propose that outflow channels were not related to aqueous processes but to low-viscosity volcanic floods. Indeed, Venus and some locations on Mars, Mercury, and the Moon display volcanic flows with local patterns similar to outflows (e.g., Leverington 2004). However, the presence of fluvial bars and deltaic deposits observed in some outflow channels, such as Okavango Valles (Mangold and Howard 2013), is typical of deposits formed by water flows and not lava accumulations.

The formation of outflow channels has been debated for decades, especially in the case of the Xanthe Terra outflows, where the putative source area is comprised of chaotic terrains. It is generally admitted that overpressurized aquifers is the most common explanation, or a sudden melting of an ice-rich permafrost, perhaps, in relation with magmatic activity (e.g., Carr 1979; Manga 2004; Hanna and Phillips 2006; Andrews-Hanna and Phillips 2007; Komatsu et al. 2009; Rodriguez et al. 2005, 2015; Jaumann et al. 2015). Given the variety of outflow channels source areas (chaotic terrains, volcanoes, fractures, etc), the formation of outflow channels may have involved multiple processes. For instance, lake overflows have been proposed for the ancient Ma'adim Vallis (Irwin and Howard 2002). The climatic significance of outflows is probably low given the fact that their estimated formation timescale (with flows during days or weeks, at most) does not imply stable liquid water at the surface.

Overall, only the Noachian and, in a lesser extent, Hesperian valleys are linked to a climate significantly different from the current cold and dry climate. This interpretation is still debated, because climate models fail to reproduce conditions enabling sustained liquid water at the surface (e.g., Wordsworth et al. 2013). As a consequence, snow (or ice melting) is currently a more popular process than rainfall. Scenarios with glacial melt in a cold and wet climate try to combine observations and modeling (Squyres and Kasting 1994; Head and Marchant 2014). However, ancient valleys have a dendritic geometry different from supraglacial or subglacial glacial drainages usually characterized by a lack of organization, braiding and occurrence of point-source discharges, which are characteristics closer to those observed for outflow channels than valley networks, leaving pervasive snowmelt as the current best compromise.

4.1.2 The sedimentary record

Alluvial fans consist of subaerial deposits (no lake needed) formed by intense erosion upstream. They have been observed in dozens of impact craters, especially in the southern hemisphere (Moore and Howard 2005; Kraal et al. 2008). Observed alluvial fans appear to have formed relatively late in Mars history (Hesperian to the Early Amazonian in age, Mangold et al. 2012a; Grant et al. 2014) based on the relatively well-preserved morphology of their host craters (frequently Hesperian in age) compared with strongly degraded Noachian craters. At Gale crater, the Curiosity rover has analyzed conglomerates that were deposited by streams inside an alluvial fan, providing in situ evidence for martian fluvial activity in the Hesperian (Williams et al. 2013; Grant et al. 2014). The paucity of Noachian alluvial fans is not fully understood, although it may be simply linked to an issue of preservation.

Paleolakes have been identified through the presence of deltaic deposits in several tens of locations (including many impact craters, Cabrol and Grin 1999, 2010; Goudge et al. 2016) acting either as closed basins (such as Eberswalde crater, Malin and Edgett 2003) or open system lakes (Fig. 29) (such as Jezero crater, Goudge et al. 2012, or Ismenius Cavus, Dehouck et al. 2010). Many of these delta fans were found to be of Hesperian ages, including the famous Holden and Eberswalde craters (Quantin et al. 2005; Mangold and Ansan 2006; Mangold 2012; Hauber et al. 2014), with some pristine examples extending into the Early Amazonian period (Cabrol and Grin 1999; Hauber et al. 2014). The most recent, smaller deltas, especially stepped deltas, may have formed by ephemeral ponding (Kraal et al. 2008). These deltas have volumes of several km^3, requiring aqueous activity for durations on the order of 100–100,000 years. In contrast, Noachian deltas display much larger volumes. In the case of Terby crater, for instance, the volume of deposits is two orders of magnitude larger than the younger deltas, consistent with sustained aqueous activity at that period (Ansan et al. 2011). The low number of Noachian deltas may be related to a problem of preservation—the oldest landforms deposited in lowlands are buried beneath younger lava flows (e.g., Fassett and Head 2008), and Noachian paleolakes are mostly open-depressions rather than closed lakes in impact craters (Goudge et al. 2016). In summary, the most recent and fresh examples of deltas may not be representative of the most intense period of fluvial activity, whereas the sedimentary deposits from the ancient valleys are poorly preserved. Therefore, using deltaic deposits on

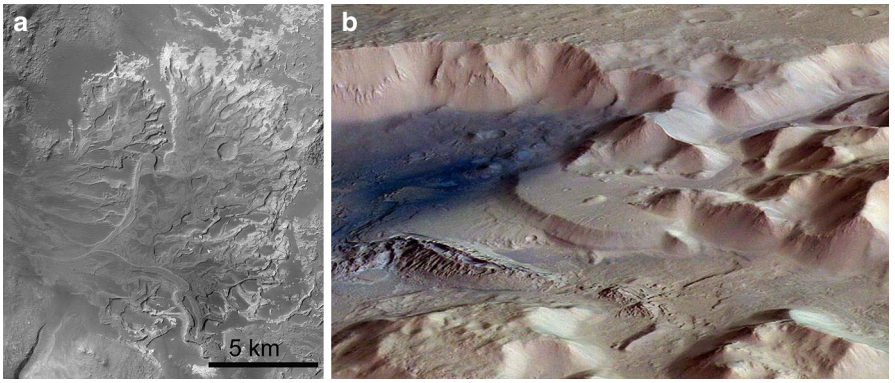

Fig. 29 **a** Delta fans with sinuous inverted channels (Eberswalde crater, NASA/MSSS/CTX image mosaic). **b** Delta fan with flat delta plain at Nepenthes Mensae (ESA/HRSC/Mars Express)

Mars as climatic indicators requires a clear understanding of the stratigraphy, context and geometry of deposition before valid interpretations can be made regarding climate evolution.

As observed in orbital data, sedimentary rocks often do not have an obvious depositional context, as the so-called light-toned deposits observed mostly in Noachian and Hesperian terrains (Nedell et al. 1987; Malin and Edgett 2000a; Stack et al. 2013). While the sedimentary facies can be assessed locally with rovers (see Sects. 4.1.4 and 4.3.2), facies can usually not be interpreted from orbital data (Grotzinger and Milliken 2012; Stack et al. 2013). In this case, layered deposits can be interpreted as aeolian, glacial, fluvial, and lacustrine of even pyroclastic deposits, leaving a large range of possible implications in terms of climatic implications. Several sequences of stratas observed from orbit display interesting cyclicity, as observed in Becquerel crater (Lewis et al. 2008; Lewis and Aharonson 2014), which have been linked to astronomical cycles, rather than volcanic deposition. The geometry of layers in central mounds could indicate a control from aeolian processes (Kite et al. 2013). However, some large deposits, such as the Medusae Fossae Formation, remain poorly explained. The most popular explanation for Medusae Fossae Formation is currently pyroclastic deposition (Kerber et al. 2012). Assessment of the bulk mineralogy of sedimentary deposits that lack depositional context (e.g., interior layered deposits in Valles Marineris) has been a major contributor to the understanding of these sedimentary rocks (see next section).

4.1.3 Hydrous minerals and alteration

The surface mineralogy provides numerous pieces of evidence that rocks were in contact with abundant liquid water in the past. Infrared imaging spectrometers (OMEGA aboard Mars Express and CRISM aboard MRO) have led to unprecedented analyses of the history of water on Mars (Bibring et al. 2005, 2006; Poulet et al. 2005; Mustard et al. 2008; Murchie et al. 2009). Two main types of hydrated minerals have been identified, clay minerals and sulfates, with local observations of other mineral types,

such as carbonates, opaline silica, and zeolites (Ehlmann et al. 2008, 2013; Michalski and Niles 2010; Carter et al. 2013; Ehlmann and Edwards 2014).

Clay minerals, technically belong to phyllosilicates, or sheet silicates, constitute a group of minerals that contain water as OH- or H_2O-molecular bonds. They form due to the intense alteration of primary minerals by leaching of mobile elements by liquid water. Clays were first detected by OMEGA in ancient terrains, mostly in outcrops of the Noachian crust. Lack of clay mineral detections in Hesperian and Amazonian volcanic regions at the kilometer scale of the OMEGA spectrometer (Poulet et al. 2005; Mangold et al. 2007; Loizeau et al. 2007). This observation led to refer as the *phyllosian* for the early period of clay formation (Bibring et al. 2006). The global distribution of clay mineral has been confirmed with higher resolution CRISM data, although limited occurrences of clay minerals in Hesperian and Amazonian terrains have been reported (Murchie et al. 2009; Ehlmann et al. 2011; Weitz et al. 2011; Thollot 2012; Carter et al. 2013; Sun and Milliken 2014). Formation of clays (and other minerals) via alteration can be due to (1) hydrothermal alteration subsequent to an impact, volcanic, or geothermal heating, (2) diagenetic alteration (during burial of sediments), and (3) supergene alteration (weathering by surface water). All these processes have been proposed and recent reviews suggest that these three types of processes have occurred on Mars (Wray et al. 2009; Milliken et al. 2010a; Carter et al. 2013; Ehlmann et al. 2013).

Evidence for hydrothermal processes was first recognized from the local proximity between phyllosilicate detections and volcanic and/or impact landforms (Poulet et al. 2008; Mangold et al. 2007; Ehlmann et al. 2008; Murchie et al. 2009; Marzo et al. 2010; Michalski et al. 2013; Viviano-Beck 2015). Clay exposures can be interpreted as formed by hydrothermal activity when they are characterized by a variety of minerals, including some formed only at relatively high-T (non-ambient, $>50\,^{\circ}C$), such as chlorite, prehnite, or serpentine (Ehlmann et al. 2011; Loizeau et al. 2012a; Viviano et al. 2013; Bultel et al. 2015). It is difficult to distinguish hydrous minerals related to excavation of buried clays and observed both in ejecta or central peaks (e.g., Mangold et al. 2007; Loizeau et al. 2012b) from minerals formed in situ by an impact-generated hydrothermal system (e.g., Schwenzer and Kring 2009). Nevertheless, several craters display complex mineralogical assemblages typical of impact-related hydrothermal activities (e.g., Toro crater, Marzo et al. 2010), as illustrated by impact-related hydrothermal systems in basalts on Earth (Yokoyama et al. 2015). Clay exposures exhumed from impact craters are ubiquitous suggesting that they are the result of the interaction of heated groundwater with rocks at depth (Ehlmann et al. 2011, Quantin et al. 2012). Clay minerals found in martian meteorites such as iddingsite—an alteration phase of olivine—were attributed to hydrothermal circulation as well, but in the Amazonian period (e.g., Gooding et al. 1991), suggesting that this form of alteration is not limited to the Noachian period. When alteration is strong or acidic, leaching can also lead to the formation of silica-rich fluids, as observed by the Spirit rover and likely corresponding to fumarolic environment (Ruff et al. 2011). Other hydrous silica outcrops (usually referred as opaline silica) have been observed close to volcanoes (Skok et al. 2010) or inside deltaic environment (Carter et al. 2013) revealing either heat sources or the presence of water.

A strong difference between clays formed by weathering and clays formed by hydrothermal activity is the much smaller number of alteration minerals found. Phyllosilicates interpreted as formed by weathering are limited to the smectite and kaolinite group that can form at low temperatures (0–50 °C). Weathering was first proposed to explain the huge exposure (300 × 300 km) of the Mawrth Vallis (Fig. 30) plateau region where Al-rich clays are superimposed on Fe-rich clays (Loizeau et al. 2007, 2010, 2012a; Chevrier et al. 2007; Wray et al. 2008; McKeown et al. 2009; Bishop et al. 2013). Such a stratigraphy is typical of terrestrial alteration profiles where Al-rich clays (usually kaolinite) are systematically superimposed over other clays, because aluminum is the least mobile cation among those present in basaltic primary rocks (Ca, Mg, Fe, and Na) and remains part of the hydrous silicate structure. Several other locations on Mars were found with a similar stratigraphy, i.e., Al-clays over Fe–Mg clays (Gaudin et al. 2011; Le Deit et al. 2012; Carter et al. 2015). These outcrops are only observed in the late Noachian epoch (3.7–3.8 Gy), suggesting that weathering was a planet-wide process at that time.

Diagenetic alteration is related to the burial of sediment in the presence of fluids that cement the initially loose sediments. Diagenetic clays have been proposed based on the orbital observations of sedimentary deposits (Milliken and Bish 2010b), although it remains difficult to distinguish diagenetic clays (also named authigenic clays) from detrital clays, which were deposited by fluvial flows that have eroded an altered bedrock (e.g., at Ismenius Cavus, Dehouck et al. 2010). Diagenetic processes were also recognized from the presence of ferroan saponite—a type of clay mineral part of the smectite group—in the lacustrine sediments analyzed by the Curiosity rover (McLennan et al. 2014, see Sect. 4.1.4).

Diagenesis is better viewed at rover scale where it can be identified from the observation of cements, fracture fills, and veins, concretions/nodules. Identification of hydrated calcium sulfate veins (such as gypsum and bassanite) is typical of fluid circulation and later precipitation in relatively mild, neutral pH conditions, as observed by both Opportunity and Curiosity (Fig. 31) (Squyres et al. 2012; Nachon et al. 2014). Various Mg-rich or Fe-rich concretions have been observed by both Opportunity and Curiosity due to diverse types of fluid circulation (Squyres and Knoll 2005; Léveillé 2014). Mn-rich fracture fills and Si-rich halos around fractures were recently observed in Curiosity data, showing that Gale Crater was submitted to a rich diversity of digenetic episodes. Both diagenetic and pedogenetic clay minerals indicate that the surface/near-surface of Mars was exposed to intense aqueous activity over significant durations ($>10^5$–10^6 years)

Sulfate deposits, in the form of Mg-, Ca-, and Fe-types of sulfates (e.g., kieserite, epsomite, gypsum, bassanite, etc.), were observed almost coevally by the Opportunity rover (Squyres et al. 2004, see Sect. 4.1.4) and the OMEGA orbiter (Langevin et al. 2005; Gendrin et al. 2005). Whereas clay minerals are observed in various geological contexts (sediments, crustal outcrops, impact craters, etc), sulfates are observed almost solely as layered sedimentary deposits, suggesting a specific environment of formation. They are distributed in an equatorial band from Valles Marineris and Meridiani Planum, including chaotic terrains from Xanthe Terra (Gendrin et al. 2005; Chojnacki and Hynek 2008; Mangold et al. 2008b; Massé et al. 2008; Flahaut et al. 2010; Sefton-Nash et al. 2012), some crater fills, including Gale crater (Milliken et al. 2010a) and

eolian deposits along the northern polar cap (Langevin et al. 2005; Massé et al. 2010). The origin of sulfate deposits has been debated, requiring the common presence of liquid water and sulfur from either volcanic outgassing or sulfide alteration, or both (e.g., King and McLennan 2010; Dehouck et al. 2012).

The most detailed observation of sulfate deposits has been made by the Opportunity rover at Meridiani Planum. Meridiani Planum sediments display layered deposits corresponding to cemented sandstones of eolian origin with local fluvial deposits and cemented by a sulfur-rich fluid that leads to a 30% abundance of Mg–Fe sulfates in these sediments (Squyres et al. 2004). These sediments also include abundant Fe-oxides, occurring as concretions and cements, and local observation of jarosite (a K/Na–Fe sulfate forming at pH of 2–4). A cemented by an acidic fluid circulation is the scenario that best fitted these observations, although alternative scenarios have been proposed (Squyres et al. 2004). These sediments are present over the 30 km traverse of Opportunity in these plains and form layer up to 1 km thick. These observations may be extended using orbital data to a 500 km × 500 km region. Meridiani Planum still serves as ground truth for many sulfate-rich deposits detected from orbital data. Their relatively late stage deposition (mostly in the Hesperian) leads to the conclusion that they formed during an acidic stage postdating the earlier clay-rich phase (Bibring et al. 2006). It remains unclear if the acid groundwater alteration scenario favored for Opportunity observations can be applied to all sulfate deposits.

Apart from clay and sulfate minerals, carbonates have been locally observed as hydromagnesite, an Mg-rich carbonate is probably coeval with the formation of serpentine and linked to the alteration of olivine-rich bedrock in the Nili Fossae region (Ehlmann et al. 2008). Local outcrops of magnesite or calcite have also been reported from central peaks of impact craters (Michalski and Niles 2010; Wray et al. 2016), and siderite (Fe-carbonate) has been detected on the Columbia Hills by the Spirit rover (Morris et al. 2010). Martian meteorite ALH84001 contains carbonates formed as a result of fluid circulation at depth, tough the oxygen isotopic ratio suggests a meteoric origin for the water (e.g., Halevy et al. 2011; Shaheen et al. 2015). The presence of carbonates is fundamental as it is potentially a significant sink for CO_2 which has broad implications for evolution of Mars' atmosphere. Nevertheless, the number of detections of carbonates is limited and would only explain a very small fraction of the missing CO_2 suspected to have sustained a warmer climate in the past (see Sect. 4.4, Edwards and Ehlmann 2015).

4.1.4 Past oceans?

The presence of hydrological systems during the Noachian and the intense weathering indicated by the presence of clay minerals suggest that standing bodies of water were present in the main topographic lows, the Hellas basin, and the northern plains. While evidence for a large "sea" in the 2000 km in diameter Hellas Planum has been provided relatively recently (Wilson et al. 2007), the question of an "ocean" in the broader northern plains area has been debated for more than three decades. Shorelines were suggested from the interpretation of Viking images (Baker et al. 1991; Parker et al. 1993). These shorelines were observed at two distinct levels; they correspond to faint landforms similar to what is observed on Earth for lakeshores with varying levels.

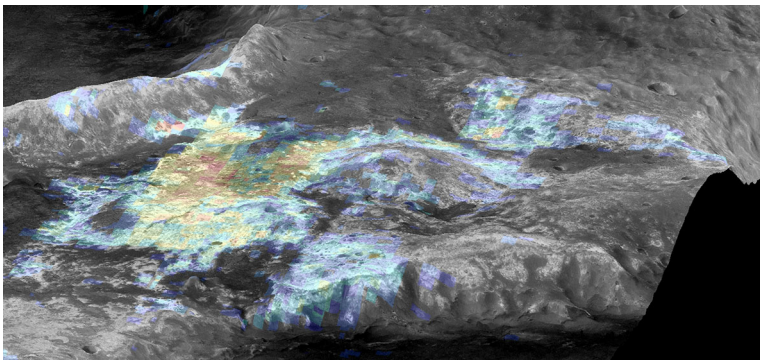

Fig. 30 Mawrth Vallis ancient plateau covered by clay-rich deposits mapped here in false-color by the OMEGA spectrometer on a visible image in relief (ESA/HRSC/OMEGA/Mars Express)

Topographic evidence from MOLA does not support the theory that the highest elevation features are shorelines, but the lowest feature, at −4 km, was shown to closely follow an equipotential surface, supporting its origin as a shoreline (Head et al. 1999). Later, this interpretation was challenged, because detailed analysis of these putative shorelines in high-resolution images did not sufficiently support their formation by a northern ocean.

Clues regarding possible oceans in the northern plains are buried beneath thick sedimentary and volcanic terrains (Baker et al. 1991; Tanaka et al. 2014). Locally, impact craters enable the detection of clay minerals showing that hydrated minerals are, indeed, present at depth (Carter et al. 2010), but surface terrains are Late Hesperian or Amazonian in age (Tanaka et al. 2014) and, therefore, postdate the clay-forming early period. Consequently, the existence (or lack) of a Noachian ocean is difficult to demonstrate. In contrast, evidence for a Late Hesperian body of water has been proposed from various observations. Deltas in open basins may require the presence of an ocean in the northern plains (Di Achille and Hynek 2010; Di Biase et al. 2013). Most of these fans formed over Hesperian terrains, suggesting that they could be associated with such a late ocean. The low measured values of the dielectric constant measured from MARSIS radar data in northern plains are also consistent with the presence of low-density sedimentary deposits, which would support the hypothesis of a putative Late Hesperian ocean (Mouginot et al. 2012). A late Hesperian northern ocean could have been fed by outflow channels (Head et al. 1999; Carr and Head 2015) through episodic fillings. Its deposits could be separated from the Noachian deposits by the emplacement of Hesperian effusive volcanic plains deduced from buried structures (Head et al. 2002). The presence of water-rich sediments would agree with the occurrence of mudflows (Jöns 1984) and with channels occurring on bordering terrains and interpreted as the result of tsunami (Rodriguez et al. 2016). The latter study implies a much longer duration of episodic outflow channel activity than previously thought. While the debate on the northern plains ocean is ongoing, the timing of events and age of landforms considered are fundamental to address its relevance to the past climate.

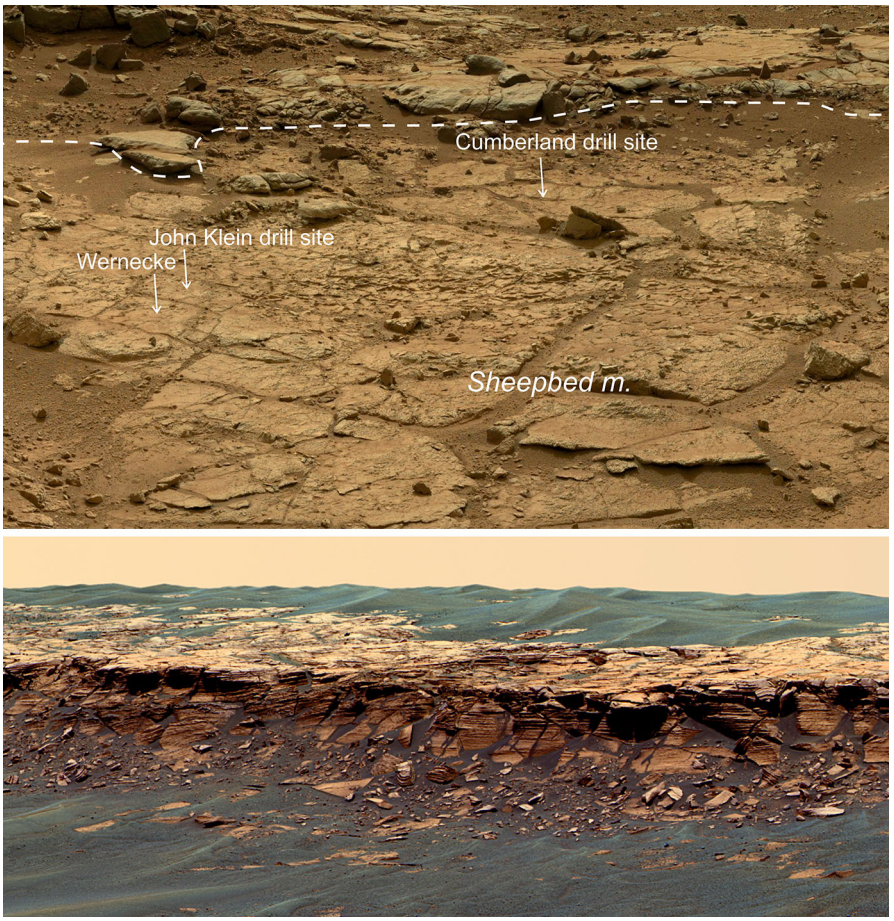

Fig. 31 *Top* lacustrine mudstones (Sheepbed) containing 20% of clay minerals as observed by the Curiosity rover (NASA/JPL/MSSS). The *dotted line* indicates the boundary with the fluvial sandstones above mudstones. *Bottom* eroded scarp of Meridiani Planum sulfate-bearing sediments analyzed by the Opportunity rover (NASA/JPL/MSSS)

4.2 From past to modern Mars

4.2.1 Obliquity variations and past glacial landforms

Presently, the obliquity of Mars is 25.2°, close to that of the Earth. However, it has not always been the case. Numerical simulations have shown that, over the 20 past million years, the inclination of Mars' rotation axis has oscillated with considerable amplitude. Laskar et al. (2004) have shown that the evolution of Mars' obliquity is chaotic over long timescales (>10 My) in contrast with the Earth's obliquity which is stabilized by the presence of the Moon. A solution for the orbital parameters of Mars can be only inferred over a period of a few million years. Over the past 20 My, the

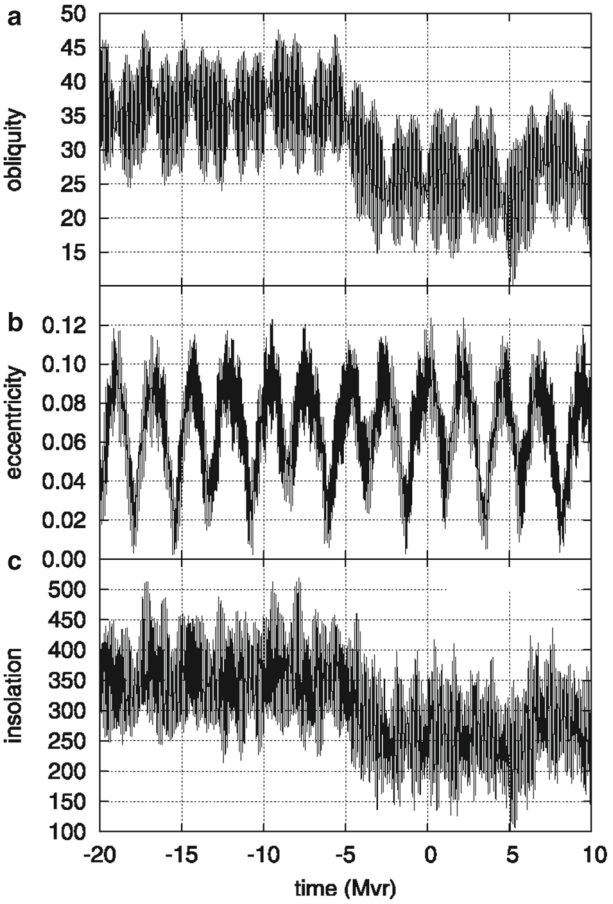

Fig. 32 Evolution of the inclination, the eccentricity, and the insolation at the North Pole as a function of time. The figure is taken from Laskar et al. 2004

inclination and the eccentricity have been oscillating with a pseudo-period of about 2 My between extreme values of 15°–45° for the inclination and 0.02–0.12 for the eccentricity (Fig. 32). They also infer that, over the past 5 Gy, the mean inclination and the mean eccentricity might have been $37.6° \pm 13.8°$ and 0.069 ± 0.03, respectively. These theoretical scenarios seem confirmed for the last few million years from the observations of the pseudo-cyclicity of layered deposits of the northern polar cap (Laskar et al. 2002; Levrard et al. 2007).

Such variations of the inclination must have had drastic consequences on the martian climate. At low inclination (below 20°), seasonal effects are moderate. The poles receive less energy than the low latitudes. In contrast, for inclinations higher than about 30°, seasonal effects are very strong. As a consequence of the strong polar insolation in this context, the CO_2 trapped in the sub-surface at the poles is released and the atmosphere becomes denser. Strong temperature contrasts, inducing strong winds and dust storms, would have occurred. The H_2O ice cap surface sublimates in summer

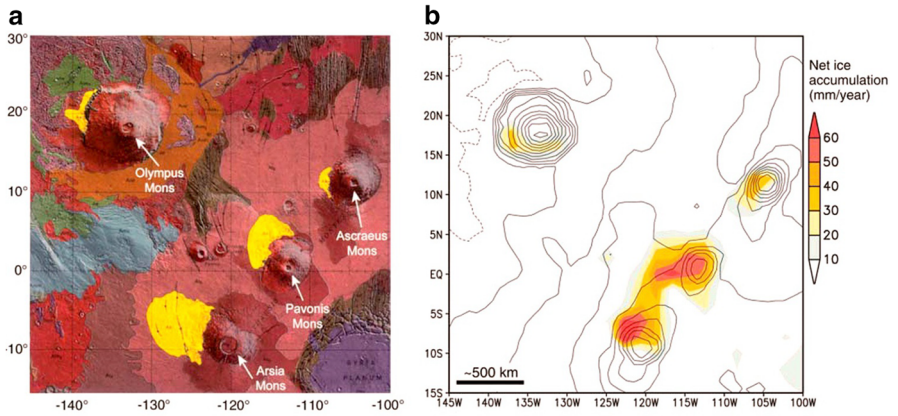

Fig. 33 Comparison between observed glacier deposits detected by Mars Express on the west flank of the Tharsis volcanoes (Head and Marchant 2003, *left*) and predictions by the Global Climate Model (Forget et al. 2006, *right*)

leading to an active seasonal water cycle. In the case of a high inclination (above 40°), models predict that H_2O released from the poles condense at mid-latitudes and locally form glaciers. Traces of past glaciers would be found on the west side of the big volcanoes, resulting from the accumulation of ice driven by the winds coming from the west (Forget et al. 2006). Actually, such features were identified by geologists before they were predicted by global climate models, both on the west flanks of the Tharsis volcanoes glaciers (Lucchitta 1984; Head and Marchant 2003; Head et al. 2005) and on the east side of Hellas basin (Head et al. 2005; Chuang and Crown 2005). These findings are remarkably consistent with the GCM predictions (Forget et al. 2006; Levrard et al. 2007; Fastook et al. 2008; Hartmann et al. 2014, Fig. 33). In addition, other locations, such as Valles Marineris, have been proposed to have hosted glaciers and residue of lobate aprons, i.e., debris-covered glaciers from the mid-latitude regions (see Sect. 2.3) have been found more equatorward than their present-day occurrence (e.g., Hauber et al. 2008; Mège and Bourgeois 2011).

Current and recent glaciers are mainly cold-based glaciers, i.e., glaciers without melting at their base. They develop only poor residual debris known as ablation till. Unlike cold-based glaciers, wet-based glaciers are subject to basal slip, which increase the basal velocities and the capacity of glaciers to erode landscapes, producing moraines, and other landforms associated with glacial melt or subglacial flows. The past presence of wet-based glaciers with basal melt has been reported from the identification of eskers similar to those formed during Pleistocene glaciations in Northern Canada. Eskers have been proposed to have existed in Argyre Planitia and around the southern polar cap according to images of long, anastomosed ridges that mimic terrestrial eskers (e.g Banks et al. 2009), suggesting that past glaciers were, at least locally, wet based from the higher past thermal flux and warmer climate (Fastook et al. 2012).

4.2.2 Episodic fluvial activity during the Amazonian period

Glacial landforms identified in Viking images were considered to be a common type of landform in the Amazonian period (Carr 1996). In contrast, only weak evidence for liquid water during this period was reported, such as the presence of local outflow channels, whose catastrophic origin does not require a warmer climate. In contrast, new high-resolution images display small, narrow valleys (<100 km long) that represent local fluvial activity scattered in various locations of Mars, but especially in the mid-latitudes. Some of these valleys occur in association with glacial landforms as supra-glacial flows (Fassett et al. 2010) or sub-glacial melting (Hobley et al. 2014). Many valleys are observed in the mid-latitudes (30°–45°) where ice is known to be present as a latitude-dependent mantle (Mangold 2012). While these valleys are clearly influenced by the presence of ground or surface-ice, the mechanism of melting is debated. Examples on the ejecta of craters point toward heating by impact warming (Jones et al. 2011), but episodic climate change has been invoked as well (Hobley et al. 2014). These observations may be connected to small valleys observed on volcanoes and may be related to volcanic/geothermal heating, especially on Alba Patera (Gulick and Baker 1990) which have Early Amazonian age and were a unique example of Amazonian valleys at the time of their discovery. While similar processes could have led to fluvial landforms previously in the past, ancient valley networks require several orders of magnitude more time and water volume to form than these small fluvial landforms.

4.3 Active processes

4.3.1 Seasonal and polar processes

Despite the low water vapor content of its atmosphere, Mars exhibits a seasonal water cycle in addition to the two other atmospheric cycles, the CO_2 cycle, and the dust cycle. As pointed out earlier (Sect. 2.1), these cycles are the result of both the obliquity of the planet and its eccentricity. All were revealed at the beginning of the space exploration era, in particular with the Mariner 9 and Viking data. At the northern summer solstice, the north seasonal ice cap completely sublimates, liberating water vapor content in the atmosphere reaches its maximum value (about 70 pr-μm), while water condensation takes place at the south pole. Around the equinox, the water content of the two hemispheres more or less equilibrates at a mean value of $\sim$15 pr-μm. The situation is reversed at southern summer solstice, although the maximum water vapor content is only $\sim$30 pr-μm (Jakosky and Haberle 1992). This asymmetry is due to the presence of a permanent CO_2 ice cap at the southern pole that acts as a cold trap and prevents the complete sublimation of the seasonal ice cap (Fig. 34).

A specific activity is related to the presence of the southern seasonal cap and to the defrosting of the seasonal CO_2 frost. Defrosting creates spectacular landforms, including dark spots, dark streaks, and *spiders*, i.e., a structure similar to a geyser related to the heating and pressure build-up beneath translucent ice (Piqueux et al. 2003; Piqueux and Christensen 2008; Kieffer et al. 2006; Thomas et al. 2010; Pilorget

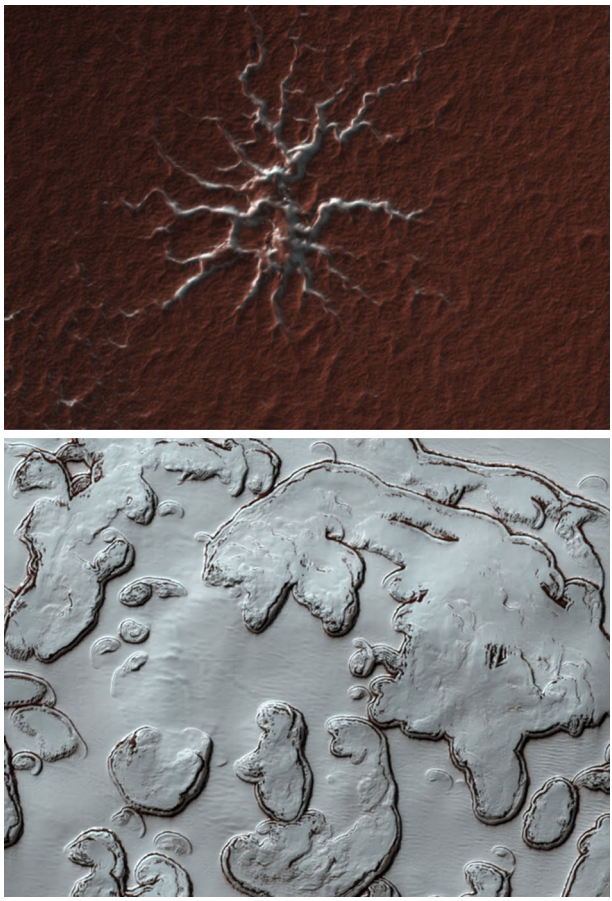

Fig. 34 *Top* spider on the south-polar cap. This activity is related to geyser activity due to translucent CO_2 ice (HiRISE images). *Bottom* "Swiss-cheese terrains" due to sublimation of the CO_2 cap (MRO/JPL/UA/LPL/HiRISE)

et al. 2011). The effect of defrosting is spectacular on dark sand dunes where the large decrease in albedo is huge and produces a sudden warming that enhances the process (Kossacki and Leliwa-Kopystynski 2004; Gardin et al. 2010; Hansen et al. 2010, 2013). Most of these features are seasonal and disappear after the surface is defrosted, but the long-term effect of CO_2 defrosting on martian landscape evolution is not yet fully understood.

4.3.2 Atmospheric dust and aeolian activity

Seasonal dust storms are associated with warming of the surface that influences seasonal frost at high-latitudes. Dust storms occasionally coalesce into planet-wide storms, as observed in ground-based observations. A famous global storm has occurred at the end of 1971 when Mariner 9 was entering into Mars orbit. Saltation of sand parti-

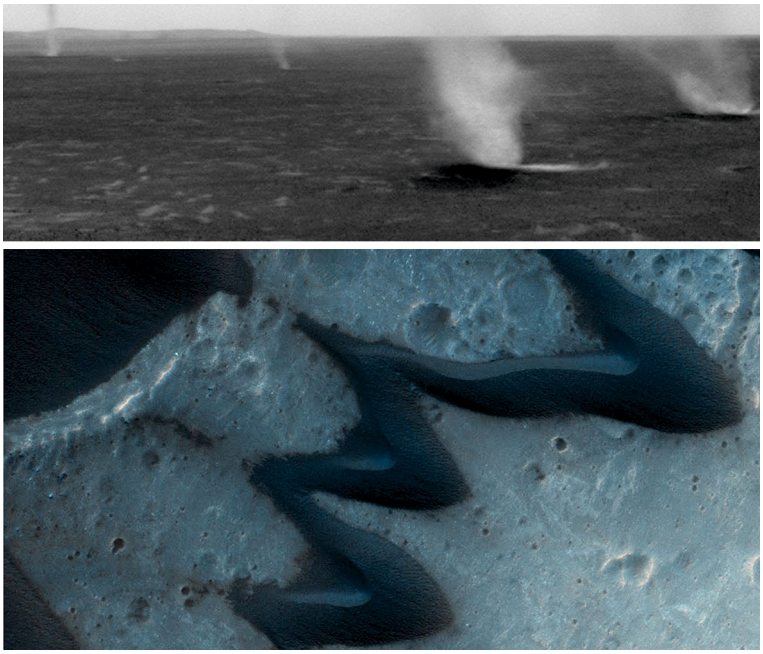

Fig. 35 Dust devils revealed by the Spirit rover (NASA/JPL/MER). Basaltic barkhane dunes imaged by HiRISE (MRO/JPL/UA/LPL/HiRISE)

cles removes the smaller dust particles from sand grains, lifting them in the atmosphere. On Earth, dust usually consists of particles <10 μm that can be a wide range of compositions, depending on the geological source region. On Mars, due to the thin atmosphere, dust particles lifted in the atmosphere are generally around or smaller than 1 μm. The dust has a homogeneous basaltic composition, with iron oxides giving its orange color (Hunten 1979). The characteristic orange/reddish color of Mars is due to dust deposits at the surface, usually in thin mantles (<1 mm), but with local sinks of thick deposits (e.g., >20 m in Arabia Terra). *Dust devils* are due to vortices created by thermal flux from daily surface heating, a process that is also observed on Earth (Fig. 35) (Balme et al. 2006). The Spirit rover has observed dust devils on Gusev crater floor. Many high-resolution images of the surface show dark streaks with local spirals formed by dust devil tracks. Dust accumulation and related avalanches are also involved in the formation of dark or bright slope streaks (Sullivan et al. 2001; Baratoux et al. 2006), which are specially observed in the dustiest regions of Mars.

The role of surface winds is also evidenced by numerous sand dunes present in many regions, including polar regions. Dark dunes composed of basaltic particles are predominant. Their dark, dust-poor surface suggests that they are active or were active recently. Movements of dunes have, indeed, been observed in repeated observations taken years after years (Bourke et al. 2008; Bridges et al. 2012). Light-toned dunes also exist and are either interpreted as dust-covered dunes or dunes composed of other particles. Transverse Aeolian Ridges (referred as TARs) are specific to Mars corresponding to ∼10 m small light-toned dunes transversal to the main wind regimes

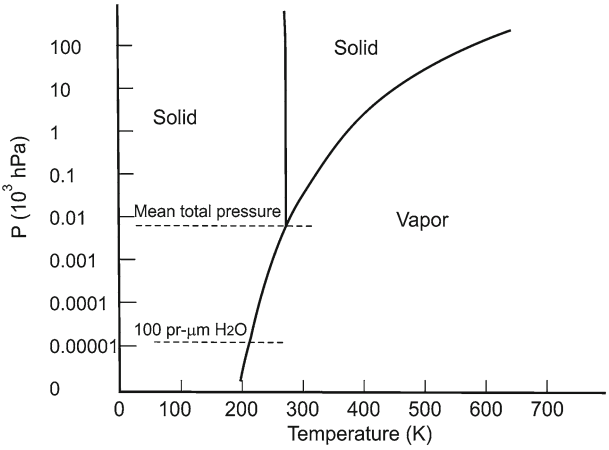

Fig. 36 Phase diagram of H_2O

and which origin is debated (dust clumps, dust-covered megaripples, see Balme et al. 2008; Geissler 2014, for discussions). Recent images from Curiosity show for the first time that dune slipface and large ripples may be a specific type of wind-drag ripples (Lapotre et al. 2016). Sedimentation and cementation of aeolian dunes create aeolian sandstones, usually containing cross-beddings with significant angles (up to ∼30°) as a consequence of the internal architecture of sand dunes. Examples of in situ-cemented dunes have been observed at Meridiani Planum by the Opportunity rover and at Gale Crater by the Curiosity rover.

4.3.3 Volatile-rich processes and transient melting

The phase diagram of water (Fig. 36) shows that the water content and the surface pressure are too low for water to be in liquid form in the temperature range found at the surface of Mars (typically 150–300 K). However, recent gullies have been observed by the Mars Orbiter Camera (MOC), perhaps, indicating the presence of liquid water in the most recent periods (Fig. 37a). Gullies have small channels that are 10–20 m wide and from 100 m to 2 km long (Malin and Edgett 2000a, b). They likely form through ephemeral flows, similar to debris flows-mud flows on Earth (Costard et al. 2002; Mangold et al. 2003). While they were initially thought to be due to subsurface water reservoirs (Malin and Edgett 2000a), their geologic setting and their relationship with insolation—polar facing slopes contain more gullies than any other slopes—favor surface/atmospheric processes (Costard et al. 2002; Balme and Greeley 2006). Recent periods of high obliquity phases may be responsible for snowmelt on polar facing slopes within mid-latitude regions (Costard et al. 2002). Dry flows, as studied on Earth, are unable to generate the sinuous patterns observed for many gullies, which is a characteristic of aqueous flows (Mangold et al. 2010b). Nevertheless, recent images suggest some form of gravity flows during defrosting periods, so under current obliquity conditions (Dundas et al. 2012). This observation has led to the development of new explanations for the recent gullies involving CO_2 frost, and solid or gaseous

flows (Cedillo-Flores et al. 2011; Dundas et al. 2012; Pilorget and Forget 2016). The current activity is relatively limited in extent and the exact physical process poorly understood given the lack of experimental constrains on such kind of slurries. It is currently unclear if such CO_2 enhanced defrosting activity was able to generate the larger gullies observed on the flanks of many mid-latitude craters or if the latter was generated by liquid water. As on Earth where gravity-related processes can generate debris flows, rockfalls, and snow avalanches, martian hillslopes are the location of various types of erosional activities.

A potential interpretation in parallel to the snow/ice melting process for gullies is the interpretation of landforms related to ice melting around gullies. Indeed, freeze–thaw cycles have strong effects on ice-rich permafrost, such as the development of solifluction lobes and sorted patterned grounds. These processes actually start well below 0 °C (and down to −20 °C depending on grain size) due to the presence of unfrozen water in the form of thin films at grain boundaries (e.g., French 1996). These films create a migration of liquid water, resulting in the segregation of ice and development of landforms, such as pingos and hummocky terrains. Growing evidence of the role of unfrozen water and/or freeze–thaw cycles is found from the identification of solifluction lobes and patterned ground, such as sorted polygons, sorted stripes, thermokarst, and hummocky patterns (Seibert and Kargel 2001; Mangold 2005; Soare et al. 2008; Johnsson et al. 2012). Several examples of recent retrogressive thaw slumps and sorted polygons were reported in equatorial regions (in the Cerberus Fossae region) where they may sign some unusual processes in regions previously expected to be devoid of water ice (Balme et al. 2011). The presence of unfrozen water may also be linked to the finding by the Phoenix Lander of small amount (<1%) of carbonates and perchlorates that may be related to local chemical alteration below 0 °C (Hecht et al. 2009). Another result from Phoenix was the detection of perchlorate salts. The mapping of the distribution of perchlorate salts has been explained with the presence of thin films of liquid water which are responsible for translocating perchlorates from the surface to the sub-surface (Cull et al. 2010), bringing into question their role in slope processes.

More recently, a type of potentially volatile-rich, active flow has been found on slopes in equatorial and mid-latitude regions (McEwen et al. 2011). Dark, 100–300-m-long elongated streaks called Recurrent Slope Lineae (RSL) form on 25°–40° steep slopes and are distinct from dust-related slope streaks. They present an elongated tongue shape with poor channeling usually typical of granular flows (Fig. 37b). However, RSLs form predominantly in springtime and the early summer on slopes that are heated by the sun, locally above melting point, indicating a role of volatiles, potentially liquid water (McEwen et al. 2011). Various processes are invoked to explain this activity, including brines, ephemeral water flows, or granular flows, triggered by sublimation. Recent observations of perchlorates in a few pixels on RSL slopes may indicate the role of these salts in lowering the water ice melting point (see discussion by Ojha et al. 2015 and references therein, Massé et al. 2016). Evidences for liquid water remain tenuous and debated, especially because there is no obvious water replenishment in the equatorial regions where these landforms are observed, although atmospheric water vapor could be favored given the specific properties of perchlorate salts to capture moisture.

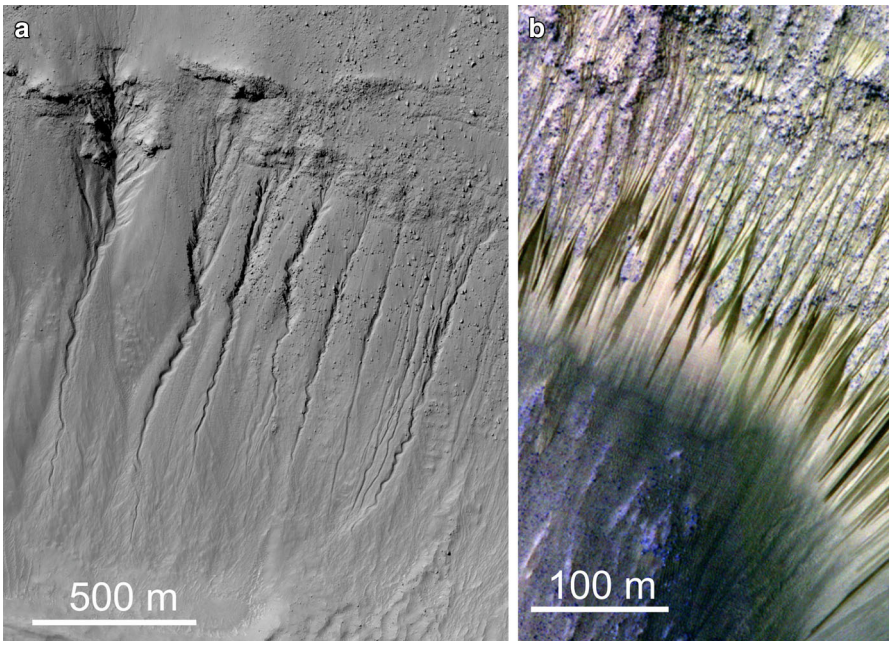

Fig. 37 **a** Gullies on the flank of a recent crater interpreted as debris flows triggered by either ice melting, CO_2 defrosting, or a combination of these processes. Note the sinuous shape of some of the channels that is different from straight volatile-free flows. **b** Recurrent Slope Linae (*RSL*) are landforms active in the springtime and summer season, possibly in relation with a liquid, perhaps briny water occurrence

4.4 Atmospheric escape as a key to atmosphere evolution

4.4.1 Atmospheric escape: observations from isotopic ratios

D/H ratio

Isotopic ratios in gaseous species are important tracers of the history and evolution of the Martian atmosphere. Indeed, thermal escape over the planet's lifetime induces a fractionation mechanism between the isotopic species, the heavier isotope being enriched over time as compared with the lighter one. The effect is especially sensitive for hydrogen and deuterium, as the D atom is twice as heavy as the H atom. Continuous escape of water vapor over the history of the planet is expected to lead to an enrichment of HDO with respect to H_2O, as the HDO molecule is heavier. Such an effect is especially strong in the case of Venus, where a D/H enrichment by a factor of more than 100 with respect to the terrestrial value has been measured in the lower atmosphere (Bézard et al. 1990). In the case of Mars, the first measurement of D/H indicated an enrichment six times the Standard Mean Ocean Water (SMOW). This effect was interpreted as the signature of a warmer and wetter early atmosphere (Owen et al. 1988), but the quantitative assessment of the early surface pressure remained uncertain (Owen 1992; Carr 1996).

HDO was first observed from ground-based high-resolution spectroscopy at 3.7 μm. By comparison with H_2O lines observed at 1.1 μm, Owen et al. (1988) derived an enrichment of the Martian D/H ratio by a factor of 6 ± 3 with respect to the SMOW. Subsequent measurements were obtained by Bjoraker et al. (1989) using the Kuiper Airborne Observatory ($D/H = 5.2 \pm 0.2$). Ground-based near-infrared spectroscopy was again used later for disk-integrated values by Krasnopolsky et al. (1997; $D/H = 5.5 \pm 2.0$) and Krasnopolsky (2015), and for D/H mapping in specific locations (Novak et al. 2011). Using the InfraRed Camera and Spectrograph (IRCS) at the Subaru telescope, Aoki et al. (2015) measured mean latitudinal values of D/H of 4.1 ± 1.4 SMOW and 4.4 ± 1.0 SMOW for $Ls = 62°$ and $Ls = 96°$, respectively. Villanueva et al. (2015, Figure 38) obtained maps of D/H with large latitude coverage for different seasons from spring equinox to northern summer solstice ($Ls = 335°$, 50°, 80 and 83°). They reported a global increase from equinox to solstice with, near $Ls = 80°$, a strong enrichment from south (about 3 around 50°S) to north (up to 10 around 60°N). The authors also reported an increase of D/H as a function of altitude. Another map of D/H was obtained by Encrenaz et al. (2015a, 2016) using simultaneous high-resolution spectroscopy of HDO and H_2O near 7.2 μm with the Echelon Cross Echelle Spectrograph (EXES) imaging spectrometer aboard the Stratospheric Observatory for Infrared Astronomy (SOFIA). The data, obtained shortly after northern summer solstice ($Ls = 113°$), are in remarkable agreement with the observations by Villanueva et al. (2015) for $Ls = 80°$–83°. They are also in excellent agreement with the results of Krasnopolsky (2015) and Aoki et al. (2015). Finally, D/H in the martian atmosphere was also measured by SAM/Curiosity; an enrichment by a factor 6 ± 1 was found at Gale crater (Webster et al. 2013), consistent with ground-based subsequent measurements.

The general trend of the D/H variation with season and location can be interpreted on the basis of the Vapor Pressure Isotope Effect (VPIE), by which fractionation is driven by condensation/sublimation effects. It is known that, at thermochemical equilibrium, the HDO/H_2O ratio in ice, as compared with the gas phase, decreases as a function of increasing temperature (Merlivat and Nief 1967). As a result, D/H is enriched in the ice phase compared with the gas phase. Near northern summer solstice, the massive outgassing of the northern water ice cap induces a D/H enrichment of the water vapor above it. D/H in the gas phase also shows a positive correlation with temperature and with the total water vapor content, because in this case, condensation effects are minimized. These correlations, described and predicted by the Global Climate Models (Fouchet and Lellouch 2000; Montmessin et al. 2005), were actually observed by Villanueva et al. (2015) and Encrenaz et al. (2016).

On a global scale, the measurement of the disk-integrated value of D/H in the Martian atmosphere, also integrated over the seasonal cycle, is an indicator of the total water content in the early history of Mars. As discussed by Owen et al. (1988) and Owen (1992), to produce a deuterium enrichment by a factor of 5, most of the water available at the surface would have to be destroyed with subsequent hydrogen escape. Owen (1992) pointed out the contradiction between this result and the very low hydrogen escape presently measured on Mars (McElroy et al. 1976), and suggested a much faster early hydrogen escape. Another paradox remains: the very large amount of liquid water required to account for the erosional features at the surface (Carr 1986).

This question was addressed in several analyses (Yung et al. 1988; Carr 1990, 1996; Jakosky 1990; Krasnopolsky et al. 1997).

In their latest analysis, Villanueva et al. (2015) give an estimate of the disk-integrated D/H of Mars, averaged over the seasons, by considering the D/H value measured during maximum outgassing, and they derive a deuterium enrichment of 8 with respect to the SMOW value. Using this result, they give an estimate of the initial reservoir M_P using the current reservoir M_C and the initial and current isotopic ratios I_P and I_C, using the relationship:

$$M_P/M_C = [I_C/I_P]^{[1/(1-f)]}$$

where f is the fractionation escape rate. Using $f = 0.02$, on the basis of HST measurements of D and H Ly α emissions (Krasnopolsky et al. 1998), and $I_C = 1.275$ from an SNC meteorite analysis (Usui et al. 2012), Villanueva et al. (2015) infer $M_P/M_C = 6.4$.

We note that the value used for f is very different from the one previously assumed by Carr (1996), on the basis of Yung et al. (1988) who assumed $f = 0.32$; this value would lead to $M_P/M_C = 15$. As a value for the current water reservoir M_C, Villanueva et al. (2015) use the estimate of Kurokawa et al. (2014) who obtain 21 m of Global Equivalent Layer (GEL) by summing the polar layer deposits at the northern and southern poles, based on radar estimates (Plaut et al. 2009). The estimate of the initial water content in Villanueva's analysis is then a GEL of 137m, corresponding to an ocean covering about 20% of the planet around the North pole in view of its topography, more in agreement with geological and geophysical estimations of water ice (Sect. 2.3). More information about the D/H ratio on Mars is expected to be provided by the instruments of the MAVEN spacecraft and the LAP (Ly Alpha Photometer) aboard the Mangalyaan mission.

In addition to the D/H measurement in the Martian atmosphere, information about D/H in minerals has recently been provided by the Curiosity rover (Mahaffy et al. 2015). The Sample Analysis at Mars (SAM) mass spectrometry experiment, operating in Gale crater, has measured D/H in ancient Martian clays including strongly bound water and/or hydroxyl minerals dating from Hesperian-era clay, aged of about 3 Gy. The measured D/H was 3.0 ± 0.2, an intermediate value between the expected value of the early Mars (close to 1) and the present enrichment (about 8). This result is consistent with a continuous hydrogen escape evolution, instead of a massive outgassing at the beginning of the planet's history. However, this result contradicts other analyses of D/H performed of SNC meteorites aged of 4.1 Gy, for which high D/H values were found (Boctor et al. 2003; Greenwood 2008). In particular, Greenwood (2008) measured D/H enrichments of 4 in ALH84001, aged over 4 Gy, and 5.6 in the young (0.17 Gy) Shergotty meteorite. These results show that there is still an open question about the history of water outgassing on Mars.

Other isotopic ratios

In addition to D/H, isotopes of C, N, and O are important tracers of atmospheric loss. The best example is provided by the $^{15}N/^{14}N$ ratio, which was first measured by the mass spectrometers of the Viking landers. Viking found an enrichment of 1.6 times

the terrestrial value ($^{14}N/^{15}N = 168 \pm 17$; Nier et al. 1976; Nier and McElroy 1977), recently confirmed by SAM aboard Curiosity ($^{14}N/^{15}N = 173 \pm 11$; Wong et al. 2013). This enrichment was interpreted as the signature of a differential escape of atomic nitrogen, following the dissociation of N_2 by energetic atoms. On the basis of this result, McElroy et al. (1976) inferred a primitive N_2 partial pressure in the range of 1.3–30 mbar. Owen (1992), by comparing the C/N ratio on Mars, Earth, and Venus, inferred an early surface pressure of a few hundred mbar (Owen and Bar-Nun 1995).

Several attempts have been made to measure isotopic ratios in carbon and oxygen using spectroscopic data of CO and CO_2 (Kaplan et al. 1969; Krasnopolsky et al. 1996; Encrenaz et al. 2005), as well as Viking mass spectrometry measurements (Nier and McElroy 1977). In view of the error bars, there was no definitive evidence for a departure of $^{13}C/^{12}C$ and $^{18}O/^{16}O$ with respect to the terrestrial values.

More precise measurements of C and O isotopic ratios in CO_2 have been obtained by SAM aboard Curiosity (Webster et al. 2013). Departures from terrestrial values are defined by δ where δ is given by

$$\delta = 1000 \times (R_{\text{sample}} - R_{\text{Earth}})/R_{\text{Earth}}.$$

The δ values measured by SAM were about 25 for ^{17}O, 50 for ^{18}O and ^{13}C, and 100 for $^{13}C^{18}O$. They are consistent with a mass-dependent fractionation for ^{17}O and ^{18}O, and also in agreement with SNC meteorites (Carr 1990).

In the case of noble gases, their isotopic ratios were first measured by the Viking mass spectrometers, then by SAM aboard Curiosity. The non-radiogenic isotopic ratios of Ar, Kr, and Xe were consistent with terrestrial values. In contrast, significant enrichments were measured in the case of radiogenic isotopes, ^{40}Ar (product of ^{40}K, enriched by a factor 10 with respect to Earth) and ^{129}Xe (product of ^{129}I, enriched by a factor 2.5 with respect to Earth). These enrichments were interpreted as the signature of large impacts in the early history of the planet (Melosh and Vickery 1989; Turcotte and Schubert 1988). The similarity of the $^{129}Xe/^{132}Xe$ ratio measured by Viking and recently confirmed by Curiosity (Conrad et al. 2015) with the value found in shergottite meteorites was considered as a proof of the martian origin of these meteorites (Bogard et al. 2001). Recent isotopic measurements by Curiosity have all confirmed the model of a massive hydrodynamical escape of the martian atmosphere soon after formation (Conrad et al. 2015).

In the case of the non-radiogenic isotopes ^{36}Ar and ^{38}Ar, SAM/Curiosity obtained a precise measurement of 4.2 ± 0.1 for the $^{36}Ar/^{38}Ar$ ratio (Atreya et al. 2013), significantly different from the solar value (5.5 ± 0.01; Pepin et al. 2012) and the terrestrial value (5.305 ± 0.008; Lee et al. 2006), but in agreement with the ratio measured in martian meteorites (3.5–4.6; Bogard 1997). This result implies a substantial loss of atmosphere from the exobase of Mars after the hydrodynamical escape phase, leading to an enrichment of the heavier isotope (e.g., Pepin 1994). A summary of isotopic ratio measurements is given in Table 5.

Table 5 Isotopic ratios in the martian atmosphere (see text for references)

Isotopic ratio	Comparison standard	Atmosphere Viking	Atmosphere Curiosity
D/H	%-terrestrial	450	495
$^{14}N/^{15}N$	ratio	168 ± 17	173 ± 11
$^{13}C/^{12}C$	%-terrestrial	2.3 ± 4.3	4.6 ± 0.4
$^{17}O/^{18}O$	%-terrestrial		2.4 ± 0.5
$^{18}O/^{16}O$	%-terrestrial	0.7 ± 4.4	4.8 ± 0.5
$^{13}C^{18}O/^{12}C^{16}O$	%-terrestrial		10.9 ± 3.1
$^{20}N/^{22}N$	Ratio		
$^{36}Ar/^{38}Ar$	Ratio	5.5 ± 1.5	4.2 ± 0.1
$^{40}Ar/^{36}Ar$	Ratio	3000 ± 500	
$^{86}Kr/^{84}Kr$			Conrad et al. (2015)
$^{129}Xe/^{130}Xe$	Ratio	2.5	Conrad et al. (2015)
$^{136}Xe/^{130}Xe$			Conrad et al. (2015)

4.4.2 Atmospheric escape: physical processes and exospheric observations

Atmospheric escape processes are thought to have played a major role in the evolution of the atmosphere and of the climate of Mars, because of its low gravity. In particular, the presence of geological features and mineralogical signatures in the infrared, indicative of the influence of liquid water, would be consistent with a denser atmosphere in the early history of the planet and with a strong atmospheric escape (e.g., Chassefiere and Leblanc 2004; Bibring et al. 2005). Chamberlain (1962) mentioned the possibility for oxygen to escape Mars (and Venus), and escape rates were first estimated by Chamberlain (1969). Many theoretical studies have been carried out to explore the different processes that lead to the loss of an atmosphere, which have been supported by measurements performed by Phobos-2, Mars Express, and more recently the MAVEN spacecraft.

The erosion of the Mars' atmosphere can be, in general terms, explained by the lack of an intrinsic magnetic field, which lead to a direct interaction between the atmosphere and the solar wind, and by the low gravity of the planet. Part of the past atmospheric loss could have been due to asteroid and comet impacts, although this process is not believed to be significant (Melosh and Vickery 1989; Binh San Pham and Karatekin 2013). In general, escape processes can be divided into thermal and non-thermal mechanisms (e.g., Chassefiere and Leblanc 2004). In thermal escape, light neutral components (like Hydrogen) from the far tail of their energy distribution function may reach escape velocity and leave the atmosphere, above the exobase. The escape of heavier species is due to non-thermal processes, resulting from the interaction of the upper atmosphere with solar photons and charged particles. Four types of non-thermal escape can occur: (1) dissociative recombination, which produces 2 neutrals from an ion and an electron. The best example is $O^2 + e^- \rightarrow O + O$, where oxygen atoms acquire energy above the escape threshold. (2) Ionospheric escape, where ions

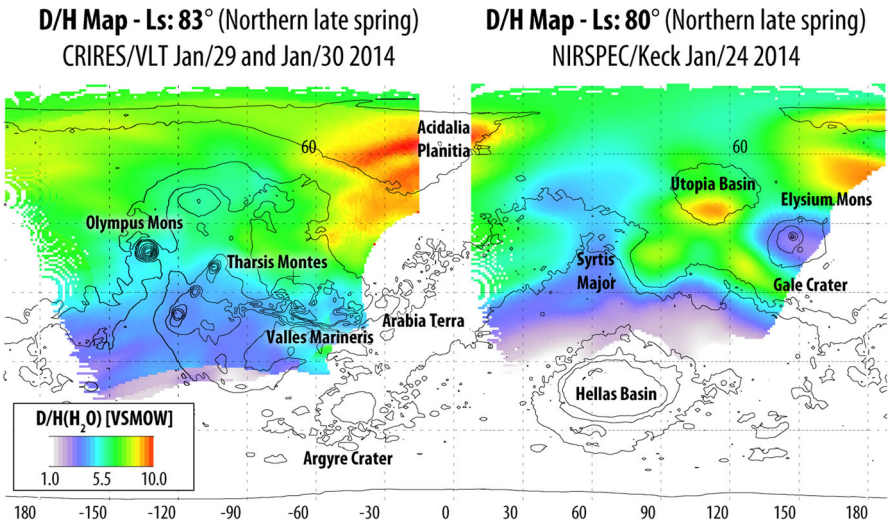

Fig. 38 Map of D/H on Mars inferred by near-infrared ground-based measurements of HDO and H_2O (from Villanueva et al. 2015)

are created in the atmosphere and leave it along the solar wind magnetic field lines or by solar wind electric field acceleration. (3) Ion sputtering, where the atmosphere is impacted by part of pick-up ions that transfer their energy to the neutral species, leading to neutral escape. (4) Energetic Neutral Atoms escape, which is the escape of hot neutral atoms produced by charge exchange between pick-up or solar wind ions and the neutral exosphere (Fig. 38).

Amongst all these non-thermal mechanisms, the ionospheric escape has been studied with Phobos-2 and Mars Express data. These space probes provide in situ measurements of ion fluxes as a function of energy, from which an escape rate is calculated. Many assumptions are behind this computation, such as observation geometry and interpolation between data, which lead to overall uncertainties of a factor of 2–3 (Barabash 2013). Figure 39 shows different estimations of the ion escape rate (Dubinin et al. 2011) from several of these assumptions. The ion escape rate typically ranges from 10^{22} to 10^{25} s^{-1}, which corresponds to a few grams per second (Barabash et al. 2007). These rates can be propagated backward over a period of 3.5 billion years, resulting in the total removal of 0.2–4 hPa of carbon dioxide and a few centimeters of GEL or water. Clearly, ion escape is a not a significant escape channel. Moreover, solar cycle effects on the heavy ion escape rate have been quantified by Lundin et al. (2013). They found that the average escape rate was increased by a factor of ≈10, from ≈10^{24} ions s^{-1} at the solar minimum to ≈10^{25} ion s^{-1} at the solar maximum, as illustrated in Fig. 40. The authors also derived an empirical expression for the Martian escape rate versus solar activity F10.7 index and the sunspot number, which is a useful tool to derive the accumulated ion escape rate from Mars based on historical records of solar activity, with big potentials to back to the young Sun epoch. More recently, Ramstad et al. (2015) have further quantified the ion escape rate with respect to upstream solar wind density, velocity, and EUV conditions. The most interesting trend is the decrease

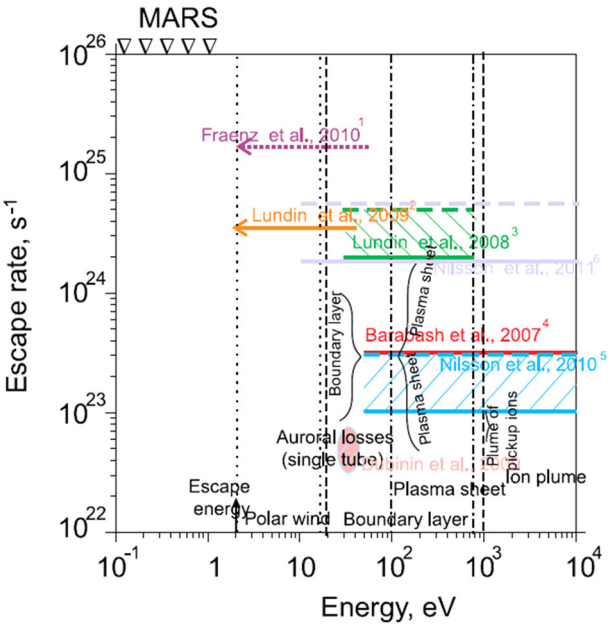

Fig. 39 Summary of ion loss fluxes at Mars evaluated by different authors on the base of Mars Express ASPERA-3 observations at different energies. The figures are taken from Dubinin et al. (2011)

of the atmospheric erosion with increasing solar wind density, in particular during low solar EUV intensity conditions. It is also important to mention the direct effect of co-rotating interaction regions and coronal mass ejections that increase the ion escape up to a factor of 2.5 (Edberg 2010).

When the escape rate data from Mars Express are compared with Earth and Venus, the ion escape at Earth is found to be similar or even higher than in the Venus and Mars cases (Barabash et al. 2009; Luhmann 2009). A possible reason for this could be the size of the Earth's magnetosphere, which is larger, and, therefore, intercepts more energy from the solar wind than Mars and Venus (Barabash et al. 2009). This observation could lead to a possible paradigm shift: Are non-magnetized bodies better protected against solar wind? Could the escape rates at Mars be much higher in the distant past, when Mars' internal dynamo was active, and there was a larger solar forcing from the early Sun?

It is obvious that to understand the evolution of Mars, we need information on the atmospheric escape over time. At this stage, it must be understood that the estimation of this quantity with the current data is still carried out with large uncertainties. First, there is not yet a clear picture of which processes are the drivers. Recent data show that the ion escape channel is not very efficient. The escape rate is low, and thus, one has to continue searching for water reservoirs and carbon dioxide stores on or beneath the planetary surface and also to investigate other escape channels (e.g. Barabash et al. 2007). Furthermore, large uncertainties are associated with the measurements and computation. The next steps are in the line of better understanding all the processes to minimize the corresponding uncertainties. The ion escape rate variability is also

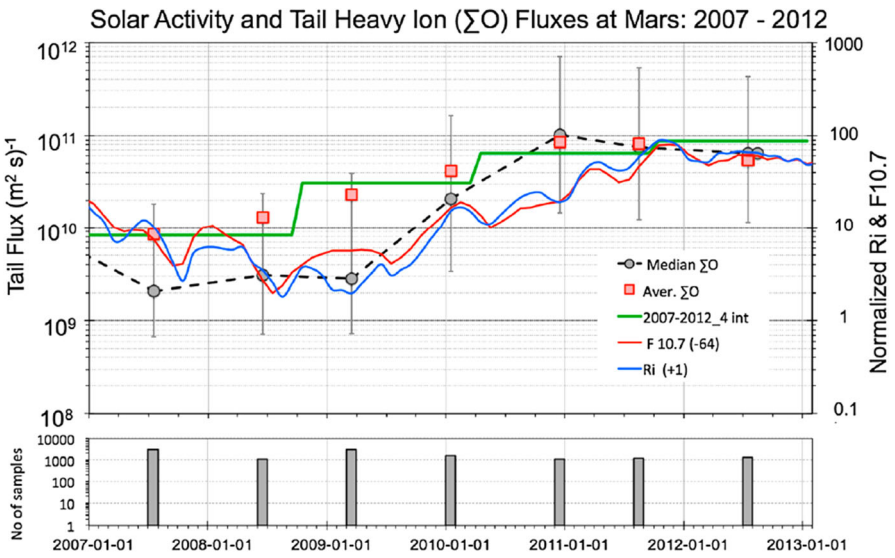

Fig. 40 From Lundin et al. (2013). Ion fluxes as function of time, illustrating the effect of the solar cycle activity. The average escape rate increased by at least a factor of ≈10 from solar minimum to solar maximum

a critical parameter to assess, and studies over a complete solar cycle are needed to assess the full range of fluctuations. Then, the challenging exercise of extrapolating previous estimations over a few billion years, from a current larger time dataset, may be improved. It is also necessary to link these results with the D/H measurements and interpretation (e.g., Chassefiere and Leblanc 2004; Mahaffy et al. 2015) for consistency. Certainly, MAVEN (Jakosky et al. 2015a, b) will bring much more information and constraints to the atmospheric escape, and thus on the evolution of the red planet. MAVEN observations have recently shown a major impact of interplanetary coronal mass ejections on atmospheric erosion (Jakosky et al. 2015a, b). The effects through the entire upper atmosphere system produced substantially disturbed conditions and appeared to have a major impact on the instantaneous rates of loss of ions to space. Given the likely prevalence of interplanetary coronal mass ejections like conditions earlier in solar system history, it is possible that ion escape rates at that time were dominated by storm events. As these early periods may have been the dominant times at which the martian atmosphere experienced loss, the inferred climate change on Mars may have been driven to a large extent by these solar storms (Jakosky et al. 2015a, b).

4.5 The fate of volatiles and their link to climate evolution

The carbon cycle

The current carbon cycle is strongly related to the seasonal CO_2 frost deposition, inducing strong seasonal flux. While current variations of climate were thought to be related mainly to astronomical parameters (eccentricity, obliquity), recent observations from the SHARAD radar have shown the presence of a buried deposit of CO_2 ice within the south-polar layered deposits which could have enhanced the total atmosphere

pressure by almost a factor of two in recent high obliquity phases (Phillips et al. 2011). In addition, clathrates/hydrates are theoretically stable at depth and could contribute to the carbon cycle (Prieto-Ballesteros et al. 2006; Chastain and Chevrier 2007; Gainey and Elwood Madden 2012; Mousis et al. 2013; Chassefière et al. 2013), including the sporadic presence of methane in the atmosphere. These examples show how the poor knowledge of the deep cryosphere is a limitation to current understanding of the current carbon cycle.

In parallel to the current reservoir of CO_2, carbonates could have trapped part of the potentially thicker early atmosphere. Recent studies concluded that carbonates observed at Nili Fossae represent a limited CO_2 reservoir unable to explain a thicker atmosphere (Edwards and Ehlmann 2015). Nevertheless, more carbonates exhumed by craters are progressively found by orbital data (Wray et al. 2016) linking to estimation of several 100 ppm of equivalent CO_2 gas trapped in these carbonates (Hu et al. 2015). An unavoidable problem is that the detection of possible buried reservoirs remains limited by the local role of impact craters which excavate these carbonates only locally. Therefore, it is currently difficult to conclude definitively regarding the total amount of carbon stored as sub-surface carbonates.

The "early Mars paradox"

As discussed above, the deuterium enrichment and other isotopic ratios, such as $^{36}Ar/^{38}Ar$, strongly suggest the presence of a large proportion of water (100s m of global equivalent layer) and a thicker atmosphere in the Noachian (above 100 mbar, but likely below 1 bar). This diagnostic comes in addition with many other geological and spectroscopic signatures (see Sect. 4.1), so there seems to be converging evidence for a warmer and wetter early Mars. However, recent attempts to model this early Mars using global climate models have failed to reproduce warm and wet conditions. Forget et al. (2013) and Wordsworth et al. (2013) have performed 3D simulations of the early martian climate assuming a faint young sun (consistent with stellar evolution models), under a wide range of surface pressures and various conditions of obliquity, orbital parameters, and atmospheric and surface properties. In most of the cases, CO_2 ice was found to cover a major part of the planet, implying a high surface albedo. As a consequence, a cold early Mars model was favored: the mean surface temperature could not have risen above 0 °C anywhere on the planet (implying no possibility for liquid water to flow). To explain observations, episodic melting of ice might have occurred following meteoritic impacts or volcanic activity. However, those conditions are currently not able to explain the lack of U-shaped glacial valleys that would form as a consequence cold and wet conditions neither to reproduce the widespread signature of surface alteration (e.g., Carter et al. 2013, 2015). The early Mars history illustrates the need for understanding Mars evolution as a whole from multiple disciplines.

5 Conclusions, outstanding questions, and future missions

5.1 Major questions

Although Mars has been the target of multiple space missions in the two last decades, many questions remain unsolved, and several have been raised after new observations

from these missions. This situation is due to the fact that Mars is probably as complex as the Earth system, with a rich and prolonged geological history, which is itself a fascinating result and a statement that can be made after these two decades of exploration.

The sub-surface structure of Mars is underconstrained due to the lack of seismological data, as is the thermal budget from the lack of knowledge of the heat flow. However, both are keys to the understanding of the energy budget of the planet, and the volcano-tectonic evolution through time, just as knowing the size of the core is important to understand of past dynamo(s) and its cessation.

The age of the surface of Mars is constrained relatively by crater densities, but retrieval of absolute ages requires isotopic dating of well-characterized surface units, for instance, by dating a well-defined surface unit by isotopic chronometers, as it was done for the Moon with the Apollo program.

The composition of the upper crust has been largely documented and relatively well understood, but the origin, proportion, and significance of felsic rocks such as those identified at Gale crater and in recently found martian meteorites remain unclear. The diversity of the composition and the structure of the crust need to be better understood: first, to be able to identify if remnants of magma ocean crystallization phase have survived until present time and, second, to understand the various processes of crustal growth after the initial differentiation.

The presence, distribution, and nature of volatile species (including H_2O, CO_2, CH_4, and various types of clathrates, and hydrates) in the upper crust remain also an unsolved question. Such a reservoir could contribute significantly to the volatile budget. Buried methane (in clathrate or other geological reservoirs) remains central in questions related to its detection in the atmosphere (Lyons et al. 2005; Atreya et al. 2007; Chassefière et al. 2013). Whether the origin of Mars' methane is biotic or not, its presence will play a central role in future science and exploration efforts, and is also of relevance to the carbon cycle.

Studies of the carbon cycle are generally related to the fundamental question of the "missing carbonates". Indeed, if the past atmosphere was denser, how would the atmosphere lost carbon, i.e., by atmospheric escape, or by the formation of carbonates at depth, or another process?

While the early Mars conditions were clearly different from the present, as deduced from various observations (aqueous mineralogy and fluvial landforms, D/H ratio, and Ar isotopes), the exact conditions under which liquid water was stable at the surface are still controversial. Was water liquid seasonally, or episodically over short periods geologically speaking? Only detailed investigations in situ as performed by rovers can help to further decipher the paleoclimate of the first billion years recorded in the ancient sediments. The precise timing and causes for the climatic transition are not well-established, but there is a general consensus that the loss of the magnetic field has strongly influenced surface conditions.

This synthesis did not focus on organics and related chemistry, but we cannot end this section without highlighting that the question of life is still the main fundamental interest for Mars researches and is the predominant question driving mission selection and design. The present dry and cold conditions are relatively uninhabitable for terrestrial life, but the presence of local niches with transient liquid water such, as RSLs

(although these landforms are also an ongoing topic of research) or sub-surface contexts, is potential habitats that may be investigated in situ in the future. Traces of past life have a higher probability than present biological activity explaining that the rover missions are focused on the analysis of >3.5 Gy old aqueous sediments. While various domains of Mars science have been greatly improved, the fundamental question of life on Mars is still far from being solved from in situ observations. Curiosity main objective is "follow the carbon", but it is not able to detect life directly, although it could do so from macroscopic observations (e.g., stromatolites). Even with samples returned on Earth and with detailed analyses by the most sophisticated laboratory instruments, we may not be able to detect or discard a past life form in rocks, as evidenced by the controversy surrounding the observation of putative bacteria fossils in the meteorite ALH84001 (McKay 1996). Nevertheless, if we can once prove that life never started on Mars, trying to understand why Mars evolved differently than the Earth may be of great interest to understand the necessary conditions for the emergence of life, a knowledge that can be applied to the increasing amount of observations that constrain surface conditions on exoplanets.

5.2 Future missions

To address some of the issues described above, several missions have been scheduled by national agencies, including two rovers. After the successful Mars Express mission launched in 2004, ExoMars is ESA's next step in Mars scientific exploration. ExoMars consists of two missions (Vago et al. 2015). The first includes two elements: the Trace Gas Orbiter (TGO) and the Entry, Descent, and Landing Demonstrator Module (EDM). The orbiter will investigate atmospheric trace gases and their sources, and serve as a communication relay orbiter, while the EDM will test new key landing technologies and will study the environment at the landing site. The second mission will deliver a rover to the surface of Mars, to search for signs of life, past and present. These two missions are being conducted as a collaboration between ESA and the Russian space agency, Roscosmos.

The orbiter and EDM were launched together on March 14th 2016 on a Proton rocket. The TGO orbiter was successfully inserted into orbit on October 19th 2016 and will start in March 2017 an aerobraking phase to reach its final circular $\sim$400-km altitude orbit, leading to a start of the nominal science phase scheduled for March 2018. The spacecraft carries four instruments from Europe and Russia that are expected to perform during at least one Martian year detailed and remote observations of the martian atmosphere, searching for evidence of gases of possible biological or geological importance. The location of sources that produce these gases will be studied by an imager. Three days before TGO orbit insertion, the EDM was ejected from the Orbiter towards the red planet, in a location named Meridiani Planum. Unfortunately, the contact with the EDM was lost shortly before the expected touchdown, suggesting a major failure during the last steps of its descent. At the time of writing of this article, there is no explanation about this failure.The goal of the EDM was to enhance Europe's expertise and enable the testing of key technologies which could be used in subsequent missions to Mars. A science package (called DREAMS) would have

operated on the surface of Mars for a few days. DREAMS would have conducted atmospheric measurements at the landing site and provided measurements of electric fields on the surface. An investigation called AMELIA (Atmospheric Mars Entry and Landing Investigation and Analysis) was also set up to study the atmosphere during the entry and descent by using the probe engineering sensors and the tracking data, recorded by Mars orbiters and by the Giant Metrewave Radio Telescope (GMRT) near Pune, India. Fortunately, most of the data of this experience were collected on time; they will enable scientists to improve atmospheric models.

The ExoMars rover mission is planned to be launched in August 2020 on a Proton rocket, with a landing on Mars in April 2021. The rover will carry a comprehensive suite of instruments dedicated to exobiology and geology research named after Louis Pasteur. It will be able to travel several kilometers searching for traces of past and present signs of life. The rover will collect and analyze samples from within rocky outcrops, and from the sub-surface, down to 2-m depth. The very powerful combination of mobility with the ability to access locations where organic molecules can be well preserved is unique to this mission. It is also planned to include instruments on the landing platform with the goal to study the surface environment. At the time of writing, three possible landing sites are being studied: Oxia Planum, Mawrth Vallis, and Aram Dorsum. For the mission to achieve high-quality scientific results regarding the possible existence of biosignatures, the rover must be delivered safely to a scientifically appropriate setting: ancient (older than 3.6 billion years), having abundant morphological and mineral evidence for long-term water activity, including numerous outcrop targets distributed in the landing ellipse (to make sure that the rover can get at least to some of them), and with a little dust coverage.

Following the success of the two Mars Exploration Rovers Opportunity and Spirit and Mars Science Laboratory Curiosity rover, the next step for NASA's robotic exploration of Mars is the Mars 2020 rover, which is planned to be launched in 2020. Within the current science theme "Seek Signs of Life", the mission would explore a site likely to have been habitable, seek signs of past life, fill a returnable cache with the most compelling samples, and demonstrate technology needed for the future human and robotic exploration of Mars. The rover will carry seven scientific projects, including an exploration technology investigation, that will produce oxygen from atmospheric carbon dioxide. The caching system will be used to store samples for potential return to Earth by a future mission not currently planned. Despite the huge technology of martian rovers, ancient sediments would be better analyzed using sophisticated terrestrial laboratories, especially looking for traces of life.

The NASA Discovery program has selected the InSight mission as the 12th Discovery mission. This mission, which is not part of the NASA Mars Program, will be the first to explore the interior of a planet by means of seismology and heat-flow probes. The evolution of the seismometers in the last 10 years allowed the InSight team to convince the scientific panels that one state-of-the-art broadband seismometer will provide information on the interior structure and the tectonics at least as good, if not better, than a network of three seismometers as it has been proposed in the past by the MESURE and NETLANDER projects. The broadband seismometer will be carried onto the Martian surface by a Phoenix-type lander. A robotic arm will delicately put the seismometer on the surface in the vicinity of the lander. The lander will also carry

a heat-flow probe that will measure the temperature gradient and the thermal conductivity of the Martian sub-surface down to 5 m. This value will bring key information on the amount of heat flux being expelled from the Martian interior, a key parameter to understand the thermal evolution of the red planet. After a delay due to technical issues, the InSight mission has been postponed to mid-2018.

While the current NASA orbiters (MRO, Mars Odyssey, MAVEN) may become old in the next decade, NASA also aims to launch another orbiter in the next decade with several instruments, including high-resolution cameras intended to track rover activities at the surface. These upcoming missions to Mars demonstrate the constant interest of this planet for the scientific community. These missions pave the way for future sample return missions and possibly crewed missions for which there is an increasing interest, although no firm schedule has been defined yet.

Acknowledgements We greatly appreciated detailed reviews from Mike Carr and anonymous reviewer. We wish to warmly thank Eliott Sefton-Nash for his detailed comments. Authors are funded by the Centre National d'Etudes Spatiales (CNES).

References

Acuna MH et al (1999) Global distribution of crustal magnetization discovered by the Mars Global Surveyor MAG/ER experiment. Science 284(5415):790–792

Agee CB et al (2013) Unique meteorite from early Amazonian Mars: water-rich basaltic breccia Northwest Africa 7034. Science 339:780–785

Agee CB, Draper DS (2004) Experimental constraints on the origin of Martian meteorites and the composition of the Martian mantle. Earth Planet Sci Lett 224:415–429

Altieri F et al (2009) O_2 1.27 micron emission maps as derived from OMEGA/MEx data. Icarus 204:499–511

Amit H, Christensen UR, Langlais B (2011) The influence of degree-1 mantle heterogeneity of the past dynamo of Mars. Physics Earth Planet Interiors 189:63–79

Anderson RC, Dohm JM, Golombek MP, Haldebamm AFC, Franklin BJ, Tanaka KL, Lias J, Brian B (2001) Primary centers and secondary concentrations of tectonic activity through time in the western hemisphere of Mars. J Geophys Res 106:20,563–20,586

Andrews DJ, Edberg NJT, Eriksson AI, Gurnett DA, Morgan D, Němec F, Opgenoorth HJ (2015) Control of the topside Martian ionosphere by crustal magnetic fields. J Geophys Res Space Phys 120(4):3042–3058

Andrews DJ et al (2014) Oblique reflections in the Mars Express MARSIS data set: stable density structures in the Martian ionosphere. J Geophys Res Space Phys 119(5):3944–3960

Andrews-Hanna J, Zuber M, Banerdt B (2008) The Borealis basin and the origin of the martian crustal dichotomy. Nature 453:1212–126

Andrews-Hanna JC, Phillips RJ (2007) Hydrological modeling of outflow channels and chaos regions on Mars. J Geophys Res 112:E08001

Andrews-Hanna JC (2012) The formation of Valles Marineris: 1. Tectonic architecture and the relative roles of extension and subsidence. J Geophys Res 117:E03006. doi:10.1029/2011JE003953

Ansan V, Mangold N (2006) New observations of Warrego Valles, Mars: evidence for precipitation and surface runoff. Planet Space Sci 54:219–242

Ansan V, Mangold N, Masson P, Gailhardis E, Neukum G (2008) Topography of valley networks on Mars from the Mars Express High Resolution Stereo Camera digital elevation models. J Geophys Res Planets 113:E07006. doi:10.1029/2007JE002986

Ansan V, Mangold N (2013) 3D morphometry of valley networks on Mars from HRSC/MEX DEMs implications for climatic evolution through time. J Geophys Res 118:1–22. doi:10.1002/jgre.20117
Ansan V et al (2011) Stratigraphy, mineralogy, and origin of layered deposits inside Terby crater, Mars. Icarus 211:273–304. doi:10.1016/j.icarus.2010.09.011
Aoki S, Nakagawa H, Sagawa H, Giuranna M, Sindoni G, Aronica A, Kasaba Y (2015) Seasonal variations of the HDO/H2O ratio in the atmosphere of Mars at the middle of northern spring and beginning of northern summer. Icarus 260:7–22
Arfstrom J, Hartmann WK (2005) Martian flow features, moraine-like ridges, and gullies: terrestrial analogs and interrelationships. Icarus 174:321–335
Arkani-Hamed J, Olson P (2010) Giant impacts, core stratification, and failure of the martian dynamo. J Geophys Res 115:E07012. doi:10.1029/2010JE003579
Arvidson R et al (2006) Overview of the spirit Mars exploration rover mission to Gusev Crater: landing site to Backstay Rock in the Columbia Hills. J Geophys Res Planets 111:E02S01
Atreya SK, Blamont JE (1990) Stability of the Martian atmosphere–possible role of heterogeneous chemistry. Geophys Res Lett 17:287–290
Atreya SK, Gu ZG (1994) Stability of the Martian atmosphere: is heterogeneous catalysis essential? J Geophys Res 99:13133–13145
Atreya SK, Mahaffy PR, Wong AS (2007) Methane and related trace species on Mars: origin, loss, implications for life, and habitability. Planet Space Sci 55:358–369
Atreya SK et al (2011) Methane on Mars: current observations, interpretation, and future plans. Planet Space Sci 59:133–136
Atreya SK et al (2013) Primordial argon isotope fractionation in the atmosphere of Mars measured by the SAM instrument on Curiosity and implications for atmospheric loss. Geophys Res Let 40:5605–5609
Baker VR, Kochel RC (1979) Martian channel morphology: Maja and Kasei Valles. J Geophys Res 84:7961–7983
Baker VR, Strom RG, Gulick VC, Kargel JS, Komatsu G, Kale VS (1991) Ancient oceans, ice sheets and the hydrological cycle on Mars. Nature 352:589–594
Baker VR, Maruyama S, Dohm J (2007) Tharsis superplume and the geological evolution of early Mars. In: Yuen et al (eds) Superplumes: beyond plate tectonics. Springer, Berlin, pp 507–522
Balme M, Mangold N, Baratoux D, Costard F, Gosselin M, Masson P, Pinet P, Neukum G (2006) Orientation and distribution of recent gullies in the southern hemisphere of Mars: observations from HRSC/MEX and MOC/MGS data. J Geophys Res 111(E5):E05001
Balme M, Greeley R (2006) Dust devils on Earth and Mars. Rev Geophys 44:RG3003. doi:10.1029/2005RG000188
Balme M, Berman DC, Bourke MC, Zimbelman JR (2008) Transverse aeolian ridges (TARs) on Mars. Geomorphology 101:703–720. doi:10.1016/j.geomorph.2008.03.011
Balme MR et al (2011) Fill and spill in Lethe Vallis: a recent flood-routing system in Elysium Planitia, Mars. Geol Soc Lond Spec Publ 356:203–227. doi:10.1144/SP356.11
Balta JB, McSween HY (2013) Water and the composition of Martian magmas. Geology 41(10):1115–1118. doi:10.1130/G34714.1
Bandfield JL, Hamilton VE, Christensen PR (2000) A global view of Martian surface composition from MGS-TES. Science 287:1626–1629
Bandfield JL (2006) Extended surface exposures of granitoid composition in Syrtis Major Mars. Geophys Res Lett 33:L06203
Bandfield JL, Edwards CS, Montgomery DR, Brand B (2013) The dual nature of the martian crust: young lavas and old clastic materials. Icarus 222:188–199
Banerdt WB, Golombek MP, Tanaka KL (1992) Stress and tectonics on Mars. In: Kieffer HH et al (eds) Mars. University of Ariz Press, Tucson, pp 249–297
Banks ME et al (2009) An analysis of sinuous ridges in the southern Argyre Plantitia. Mars. J Geophys Res 114:E09003
Barabash S et al (2007) Martian atmospheric erosion rates. Science 315:501–503
Barabash S et al. (2009) Venus, Earth, Mars: comparative ion Espace rates. 43rd ESLAB symposium, comparative planetology: Venus-Earth-Mars, ESTEC
Barabash S (2013) Ion escape from Mars and Venus. American Geophysical Union, Fall Meeting 2013, abstract #P13C-04
Baratoux D, Delacourt C, Allemand P (2002) An instability mechanism in the formation of the Martian lobate craters and the implications for the rheology of the ejecta. Geophys Res Let 29:1210

Baratoux D, Mangold N, Pinet P, Costard F (2005) Thermal Properties of Lobate Ejecta in Syrtis Major, Mars: Implications for the Mechanisms of Formation. J Geophys Res 110(E4):E04011
Baratoux D, Mangold N, Forget F, Cord A, Pinet P, Daydou Y, Jehl A, Masson P, Neukum G (2006) The role of the wind-transported dust in slope streaks activity: Evidence from the HRSC data. Icarus 183:30–45
Baratoux D, Pinet P, Toplis MJ, Mangold N, Greely R, Baptista AR (2009) Shape, rheology and emplacement times of small martian shield volcanoes. J Volcanol Geotherm Res 185:47–68
Baratoux D, Toplis MJ, Monnereau M, Gasnault O (2011) Thermal history of Mars inferred from orbital geochemistry of volcanic provinces. Nature 472:338–341
Baratoux D, Toplis MJ, Monnereau M, Sautter V (2013) The petrological expression of early Mars volcanism. J Geophys Res Planets 118: doi:10.1029/2012JE004234
Baratoux D, Samuel H, Michaut C, Toplis MJ, Monnereau M, Wieczorek M, Garcia R, Kurita K (2014) Petrological constraints on the density of the Martian crust. J Geophys Res Planets 119:1707–1727
Barker ES (1972) Detection of molecular oxygen in the Martian atmosphere. Nature 238:447–448
Barker ES (1976) Martian atmospheric water vapor observations–1972-74 apparition. Icarus 28:247–268
Barlow NG (1994) Sinuosity of Martian rampart ejecta deposits. J Geophys Res 99:10927–10935
Barlow NG (2004) Martian subsurface volatiles concentrations as a function of time: clues from layered ejecta craters. Geophys Res Let 31: doi:10.1029/2003GRL19025
Barnhart CJ et al (2009) Long-term precipitation and late-stage valley network formation: landform simulations of Parana Basin. Mars. J Geophys Res 114:E01003
Barnouin-Jha OS, Schultz PH (1996) Ejecta entertainment by impact-generated ring vortices: theory and experiments. J Geophys Res 101(E9):21,099–21,115
Barnouin-Jha OS (1998) Lobateness of impact ejecta deposits from atmospheric interactions. J Geophys Res 103(E11):25,739–25,756
Barnouin-Jha OS, Baloga S, Glaze L (2005) Comparing landslides to fluidized crater ejecta on Mars. J Geophys Res 110(E04010) doi:10.1029/2003JE002214
Barth CA, Hord CW, Stewart AI, Lane AL (1972) Mariner 9 ultraviolet spectrometer experiment: initial results. Science 175:309–312
Barth CA, Hord CW, Stewart AI et al (1973) Mariner 9 ultraviolet spectrometer experiment: seasonal variation of ozone on Mars. Science 179:795–796
Barth CA, Stewart AI, Hord CW, Lane AL (1972) Mariner 9 ultraviolet spectrometer experiment: Mars airglow spectroscopy and variations in Lyman alpha. Icarus 17(2):457–468
Beer R, Norton RH, Martonchik JV (1971) Astronomical infrared spectroscopy with a Connes-type interferometer: II-Mars, 2500–3500 cm $^{-1}$. Icarus 15:1–10
Belleguic V, Lognonné P, Wieczorek MA (2005) Constraints on the Martian lithosphere from gravity and topography data. J Geophys Res 110:E11005
Benna M (2015) Metallic ions in the upper atmosphere of Mars from the passage of comet C/2013 A1 (Siding Spring). Geophys Res Lett 42: doi:10.1002/2015GL064159
Benna M, Mahaffy PR, Grebowsky JM, Fox JL, Yelle RV, Jakosky BM (2015) First measurements of composition and dynamics of the Martian ionosphere by MAVEN's neutral gas and ion mass spectrometer. Geophys Res Lett 42: doi:10.1002/2015GL066146
Bertaux J-L et al (2005a) Nightglow in the upper atmosphere of Mars and implications for atmospheric transport. Science 307(5709):566–569
Bertaux J-L et al (2005b) Discovery of an aurora on Mars. Nature 435(7043):790–794
Bertaux J-L et al (2006) SPICAM on Mars Express: observing modes and overview of UV spectrometer data and scientific results. J Geophys Res 111:E10S90
Bertka CM, Fei Y (1997) Mineralogy of the Martian interior up to core-mantle boundary pressures. J Geophys Res 102:5251–5264
Beuthe M (2010) E-W faults due to planetary contractions. Icarus. doi:10.1016/j.icarus.2010.04.019
Bézard B, de Bergh C, Crisp D, Maillard J-P (1990) The deep atmosphere of Venus revealed by high-resolution nightside spectra. Nature 345:508–511
Bibring J-P, the OMEGA team, (2004) Perennial water ice identified around the Mars South pole. Nature 428:627–630
Bibring J-P et al (2005) Mars surface diversity as revealed by the OMEGA/Mars Express observations. Science 307(5715):1576–1581
Bibring J-P et al (2006) Global mineralogical and aqueous Mars history derived from OMEGA/Mars Express data. Science 312:400–404

Binh San Pham L, Karatekin Ö (2013) Effects of impacts on the atmospheric evolution. EGU General Assembly, Vienna, Austria, EGU2013-11758
Birck JL, Allègre CL (1994) Contrasting Re/Os magmatic fractionation in planetary basalts. Earth Planet Sci Lett 124:139–148
Bishop JL et al (2013) What the ancient phyllosilicates at Mawrth Vallis can tell us about possible habitability on early Mars. Planet Space Sci 86:130–149. doi:10.1016/j.pss.2013.05.006
Bjoraker GL, Mumma MJ, Larson HP (1989) Isotopic abundance ratios for hydrogen and oxygen in the Martian atmosphere. Bull Am Astron Soc 21:991
Boctor NZ, Alexander CM, Wang J, Hauri E (2003) The sources of water in Martian meteorites: clues from hydrogen isotopes. Geochim Cosmochim Acta 67:3971–3989
Bogard DD, Johnson P (1983) Martian gases in an Antarctic meteorite? Science 221:651–654
Bogard DD (1997) A reappraisal of the martian $^{36}Ar/^{38}Ar$ ratio. J Geophys Res 102:1653–1661
Bogard DD, Clayton RN, Marti K, Owen T, Turner G (2001) Martian volatiles: isotopic composition, origin and evolution. Chronol Evol Mars Space Sci Rev 96:425–458
Boqueho V, Blelly P-L (2005) Contributions of a multimoment multispecies approach in modeling planetary atmospheres: example of Mars. J Geophys Res 110:A01313. doi:10.1029/2004JA010414
Bougher S et al (2014) The aeronomy of Mars: characterization by MAVEN of the upper atmosphere reservoir that regulates volatile escape. Space Sci Rev. doi:10.1007/s11214-014-0053-7
Bougher S et al (2015) Early MAVEN Deep Dip campaign reveals thermosphere and ionosphere variability. Science 350(6261): doi:10.1126/science.aad0459
Bouley S, Craddock RC, Mangold N, Ansan A (2010) Characterization of fluvial activity in Parana Valles using different age-dating techniques. Icarus 207(2):686–698
Bouley S, Baratoux D, Matsuyama I, Forget F, Séjourné A, Turbet M, Costard F (2016) Late Tharsis formation and implications for early Mars. Nature. doi:10.1038/nature17171
Bourke MC, Edgett KS, Cantor BA (2008) Recent aeolian dune change on Mars. Geomorphology 94:247–255. doi:10.1016/j.geomorph.2007.05.012
Boutin D, Arkani-Hamed J (2006) Polar wandering of Mars: evidence from paleomagnetic poles. Icarus 181:13–25
Boyce J, Barlow N, Mouginis-Mark P, Stewart S (2010) Rampart craters on Ganymede: their implications for fluidized ejecta emplacement. Meteorit Planet Sci 45:638–661
Boynton WV, Feldman WC, Squyres SW et al (2002) Distribution of hydrogen in the near surface of Mars: evidence for subsurface ice deposits. Science 297:81–85
Boynton WV et al (2007) Concentration of H, Si, Cl, K, Fe, and Th in the low- and mid-latitude regions of Mars. J Geophys Res 112:E12S99
Boynton WV et al (2009) Evidence for calcium carbonate at the Mars Phoenix landing site. Science 325(5936):61–64
Brain DA et al (2006) On the origin of aurorae on Mars. Geophys Res Lett 33(1):L01201
Brakenridge GR, Newsom HE, Baker VR (1985) Ancient hot springs on Mars: origins and paleoenvironmental significance of small Martian valleys. Geology 13:859–862
Brandon AD, Walker RJ, Morgan J, Goles GG (2000) Re-Os isotopic evidence for early differentiation of the Martian mantle. Geochim Cosmochim Acta 64:4083–4095
Brandon AD, Puchtel IS, Walker RJ, Day JMD, Irving AJ, Taylor LA (2012) Evolution of the Martian mantle inferred from 187Re-187Os isotope and highly siderophile element abundance systematics of shergottite meteorites. Geochim Cosmochim Acta 76:206–235
Brasser R (2012) The formation of Mars: building blocks and accretion time scale. Space Sci Rev. doi:10.1007/s11214-012-9904-2
Breuer D, Spohn T (2006) Viscosity of the martian mantle and its initial temperature: constraints from crust formation history and the evolution of the magnetic field. Planet Space Sci 54:153–169
Bridges NT, Ayoub F, Avouac JP, Leprince S, Lucas A, Mattson S (2012) Earth-like sand fluxes on Mars. Nature 485(7398):339–342. doi:10.1038/nature11022
Bultel B, Quantin C, Andreani M, Clenet H (2015) Deep alteration between Hellas and Isidis basins. Icarus 260:141–160
Burr DM, Grier JA, McEwen AS, Keszthelyi LP (2002) Repeated aqueous flooding from the Cerberus Fossae: evidence for very recently extant, deep groundwater on Mars. Icarus 159:53–73. doi:10.1006/icar.2002.6921
Cabrol NA, Grin EA (1999) Distribution, classification and ages of martian impact crater lakes. Icarus 142:160–172

Cabrol NA, Grin EA (2010) 1–Searching for lakes on Mars: four decades of exploration. In: Nathalie AC, Grin EA (eds) Lakes on Mars. Elsevier, Amsterdam, pp 1–29
Canup RM, Asphaug E (2001) Origin of the Moon in a giant impact near the end of the Earth's formation. Nature 412:708–712
Carleton NP, Traub WA (1972) Detection of molecular oxygen on Mars, in Trauger Lunine 83. Science 177:988–992
Carr MH (1973) Volcanism on Mars. J Geophys Res 78:4049–4062
Carr MH, Crumpler L, Cutts J, Greeley R, Guest J, Masursky H (1977) Martian impact craters and emplacement of ejecta by surface flow. J Geophys Res 82:4055–4065
Carr MH (1979) Formation of martian flood features by release of water from confined aquifers. J Geophys Res 84:2995–3007
Carr MH (1986) Mars–a water-rich planet? Icarus 68:187–216
Carr MH (1990) D/H on Mars–effects of floods, volcanism, impacts, and polar processes. Icarus 87:210–227
Carr MH (1995) The Martian drainage system and the origin of valley networks and fretted channels. J Geophys Res 100:7479–7507. doi:10.1029/95JE00260
Carr MH (1996) Water on Mars. Oxford University Press, Oxford
Carr MH, Chuang FC (1997) Martian drainage densities. J Geophys Res 102:9145–9152
Carr MH, Malin MC (2000) Meter-scale characteristics of martian channels and valleys. Icarus 146(2):366–386
Carr MH, Head JW (2015) Martian surface/near-surface water inventory: sources, sinks, and changes with time. Geophys Res Lett 42(3):726–732
Carter J et al (2010) Detection of hydrated silicates in crustal outcrops in the northern plains of Mars. Science 328:1682–1686
Carter J, Poulet F (2013) Ancient plutonic processes on Mars inferred from the detection of possible anorthosite terrains. Nat Geosci 6:1008–1012
Carter J, Poulet F, Bibring J-P, Mangold N, Murchie SL (2013) Hydrous minerals on Mars as seen by the CRISM and OMEGA imaging spectrometers: updated global view. J Geophys Res 118(4):831–858
Carter J, Loizeau D, Mangold N, Poulet F, Bibring J-P (2015) Widespread surface weathering on early Mars: a case for a warmer and wetter climate. Icarus 248:373–382. doi:10.1016/j.icarus.2014.11.011
Cedillo-Flores Y, Treiman AH, Lasue J, Clifford SM (2011) CO_2 gas fluidization in the initiation and formation of martian polar gullies. Geophys Res Lett 38:L21202. doi:10.1029/2011GL049403
Chamberlain JW (1962) Upper atmospheres of the planets. Astrophys J 136:582
Chamberlain JW (1969) Escape rate of hydrogen from a carbon dioxide atmosphere. Astrophys J 155:711
Chambers JE, Wetherill GW (1998) Making the terrestrial planets: N-body integrations of planetary embryos in three dimensions. Icarus 136:304–327
Chapman MG et al (2010) Noachian-Hesperian geologic history of the Echus Chasma and Kasei Valles system on Mars: new data and interpretations. Sci Lett Earth Planet. doi:10.1016/j.epsl.2009.11.032
Chassefiere E, Leblanc F (2004) Mars atmospheric escape and evolution: interaction with the solar wind. Planet Space Sci 52:1039–1058
Chassefière E, Dartois E, Herri JM, Tian F, Schmidt F, Mousis O, Lakhlifi A (2013) CO_2-SO_2 clathrate hydrate formation on early Mars. Icarus 223:878–891
Chastain BK, Chevrier V (2007) Methane clathrate hydrates as a potential source for martian atmospheric methane. Planet Space Sci 55:1246–1256
Chaufray JY, Leblanc F, Quémerais E, Bertaux JL (2009) Martian oxygen density at the exobase deduced from O I 130.4-nm observations by spectroscopy for the investigation of the characteristics of the atmosphere of Mars on Mars Express. J Geophys Res 114:E02006
Chaufray JY, Bertaux JL, Leblanc F, Quémerais E (2008) Observation of the hydrogen corona with SPICAM on Mars Express. Icarus 195(2):598–613
Chen Y et al (2015) Evidence in Tissint for recent subsurface water on Mars. Earth Planet Sci Lett 425:55–63
Chevrel O, Gordano D, Potuzak M, Courtial P, Dingwell DB (2013a) Physical properties of $CaAl_2Si_2O_8$-$CaMgSi_2O_6$-FeO-Fe_2O_3 melts: analogues for extra-terrestrial basalt. Chem Geol 346:93–105. doi:10.1016/j.chemgeo.2012.09.004
Chevrel O, Platz T, Hauber E, Baratoux D, Lavallee Y, Dingwell DB (2013b) Lava flow rheology: a comparison of morphological and petrological methods. Earth Planet Space Sci 384:109–120
Chevrier V, Poulet F, Bibring J-P (2007) Early geochemical environment of Mars as determined from thermodynamics of phyllosilicates. Nature 448:60–63

Chevrier V, Ostrowski DR, Sears DWG (2008) Experimental study of the sublimation of ice through an unconsolidated clay layer: implications for the stability of ice on Mars and the possible diurnal variations in atmospheric water. Icarus 196:459–476
Chicarro AF, Schultz PH, Masson P (1985) Global and regional ridge patterns on Mars. Icarus 63:153–174
Chojnacki M, Hynek BM (2008) Geological context of water-altered minerals in Valles Marineris. Mars. J Geophys Res Planets 113:E12
Christensen PR, Banfield JL, Hamilton VE et al (2001) Mars Global Surveyor Thermal Emission Spectrometer experiment: investigation description and surface science results. J Geophys Res 106:23823–23872
Christensen PR, McSween JL Jr, Bandfield SW, Rogers AD, Hamilton VE, Gorelick N, Wyatt MB, Jakosky BM, Kieffer HH, Malin MC, Moersch JE (2005) Evidence for magmatic evolution and diversity on Mars from infrared observations. Nature 436:504–509
Chuang FC, Crown DA (2005) Surface characteristics and degradational history of debris aprons in the Tempe Terra/Mareotis fossae region of Mars. Icarus 179:24–42
Clancy RT, Grossman AW, Muhleman DO (1992) Mapping Mars water vapor with the VLA array. Icarus 100:48–59
Clancy RT, Grossman AW, Wolff MJ, James PB et al (1996) Water vapor saturation at low altitudes around Mars aphelion: a key to Mars climate? Icarus 122:36–62
Clancy RT, Sandor BJ, Moriarty-Schieven GH (2004) A measurement of the 362 GHz absorption line of Mars atmospheric H_2O_2. Icarus 168:116–121
Clancy RT, Wolff MJ (2001) Whitney BA (2010) Extension of atmospheric dust loading at high latitudes during the. Mars dust storm: MGS TES limb observations 207:98–109
Clifford SM (1993) A model for the hydrologic and climatic behavior of water on Mars. J Geophys Res 98:10,973–11,016
Colaprete A, Toon OB, Magalhaes JA (1999) Cloud formation under Mars Pathfinder conditions. J Geophys Res 104:9043–9054
Collinet M, Medard E, Charlier B, Vander Auwera J, Grove T (2015) Melting of the primitive martian mantle at 0.5-2.2 GPa and the origin of basalts and alkaline rocks on Mars. Earth Planet Sci Lett 427:83–84
Connerney JEP et al (1999) Magnetic lineations in the ancient crust of Mars. Science 84:794–798
Connerney JEP et al (2001) The global magnetic field of Mars and implications for crustal evolution. Geophys Res Lett 28:4015–4018. doi:10.1029/2001GL013619
Conrad PG et al (2015) In situ measurements of Kr and Xe in the atmosphere of Mars. AGU Fall Meeting, abstract # P53F-08
Conrath BJ, Curran R, Hanel R et al (1973) Atmospheric and surface properties of Mars obtained by infrared spectroscopy on Mariner 9. J Geophys Res 78:4267–4278
Conrath BJ, Pearl JC, Sith MD et al (2000) Mars Global Surveyor Thermal Emission Spectrometer (TES) observations: atmospheric temperatures during aerobraking and science phasing. J Geophys Res 105:9509–9520
Conway R (1981) Spectroscopy of the Cameron bands in the Mars airglow. J Geophys Res 86:4767–4775
Costard FM (1989) The spatial distribution of volatiles in the Martian hydrolithosphere. Earth Moon Planets 45:265–290
Costard F, Forget F, Mangold N, Peulvast J-P (2002) Formation of recent Martian debris flows by melting of near-surface ground ice at high obliquity. Science 295:110–112
Courtillot V, Allegre CJ, Mattauer M (1975) On the existence of lateral relative motion on Mars. Earth Planet Sci Lett 25:279–285
Cox C, Saglam A, Gérard J-C, Bertaux J-L, González-Galindo F, Leblanc F, Reberac A (2008) Distribution of the ultraviolet nitric oxide Martian night airglow: observations from Mars Express and comparisons with a one-dimensional model. J Geophys Res 113:E08012
Craddock RA, Howard AD (2002) The case for rainfall on a warm wet early Mars. J Geophys Res 107: doi:10.1029/2001JE001505
Craddock RA, Greeley R (2009) Minimum estimates of the amount and timing of gases released into the martian atmosphere from volcanic eruptions. Icarus 204:512–526
Cui J, Galand M, Zhang SJ, Vigren E, Zou H (2015) The electron thermal structure in the dayside Martian ionosphere implied by the MGS radio occultation data. J Geophys Res Planets 120:278–286. doi:10.1002/2014JE004726
Cull SC et al (2010) Concentrated perchlorate at the Mars Phoenix landing site: evidence for thin film liquid water on Mars. Geophys Res Let 37:L22203. doi:10.1029/2010GL045269

Dauphas N, Pourmand A (2011) Hf-W-Th evidence for rapid growth of mars and its status as a planetary embryo. Nature 473:489–491
Debaille V, Brandon A, Yin Q, Jacobsen B (2007) Coupled ^{142}Nd-^{143}Nd evidence for a protracted magma ocean in Mars. Nature 450:525–528
Debaille V, Brandon A, O'Neill C, Yin QZ, Jacobsen B (2009) Early martian mantle overturn inferred from isotopic composition of nakhlite meteorites. Nat Geosci. doi:10.1038/ngeo579
Dehouck E, Mangold N, Le Mouélic S, Ansan V, Poulet F (2010) Ismenius Cavus, Mars: a deep paleolake with phyllosilicate deposits. Planet Space Sci 58(6):941–946
Dehouck E, Chevrier V, Gaudin A, Mangold N, Rochette P, Mathé P-Y (2012) Evaluating the role of sulfide-weathering in the formation of sulfates or carbonates on Mars. Geochem Cosmochem Acta 90:47–63
Di Achille G, Hynek B (2010) Ancient ocean on Mars supported by global distribution of deltas and valleys. Nat Geo 3:459–462
Di Biase R, Limaye AB, Scheingross JS, Fischer WW, Lamb M (2013) Deltaic deposits at Aeolis Dorsa: sedimentary evidence for a standing body of water on the northern plains of Mars. J Geophys Res Planets. doi:10.1002/jgre.20100
Dickson JL, Fassett CI, Head JW (2009) Amazonian-aged fluvial valley systems in a climatic microenvironment on Mars: melting of ice deposits on the interior of Lyot Crater. Geophys Res Let 36:L08201
Dietrich W, Montgomery D (1998) Hillslopes, channels, and landscape scale. In: Sposito G (ed) Scale dependence and scale invariance in hydrology. Cambridge University Press, Cambridge, pp 30–60
Dreibus G, Wänke H (1985) Mars, a volatile-rich planet. Meteoritics 20:367–381
Dubinin E et al (2011) Ion energization and escape on Mars and Venus. Space Sci Rev 162:173–211
Dubinin E et al (2012) Upper ionosphere of Mars is not axially symmetrical. Earth Planets Space 64:113–120
Dubinin E, Fraenz M, Woch J, Barabash S, Lundin R (2009) Long-lived auroral structures and atmospheric losses through auroral flux tubes on Mars. Geophys Res Let 36:L08108
Durham WB, Pathare AV, Stern LA, Lenferink HJ (2009) Mobility of icy sand packs, with application to Martian permafrost. Geophys Res Let 36:L23203. doi:10.1029/2009GL040392
Dundas CM, Diniega S, Hansen CJ, Byrne S, McEwen AS (2012) Seasonal activity and morphological changes in martian gullies. Icarus 38(11):1047–1050
Dunlop D, Arkani-Hamed J (2005) Magnetic minerals in the martian crust. J Geophys Res 110: doi:10.1029/2005JE002404
Duru F, Gurnett DA, Frahm RA, Winningham JD, Morgan DD, Howes G (2009) Steep, transient density gradients in the Martian ionosphere similar to the ionopause at Venus. J Geophys Res 114:A12310
Edberg N (2010) Pumping out the atmosphere of Mars through solar wind pressure pulses. Geophys Res Lett 37(3):CiteID L03107. doi:10.1029/2009GL041814
Edwards CS, Ehlmann BL (2015) Carbon sequestration on Mars. Geology 43:863–866. doi:10.1130/G36983.1
Ehlmann BL et al (2008) Orbital identification of carbonate-bearing rocks on Mars. Science 322:1828–1832. doi:10.1126/science.1164759
Ehlmann BL et al (2011) Subsurface water and clay mineral formation during the early history of Mars. Nature 479:53–60
Ehlmann BL et al (2013) Geochemical consequences of widespread clay mineral formation in Mars' ancient crust. Space Sci Rev 174:329–364. doi:10.1007/s11214-012-9930-0
Ehlmann BL, Edwards CS (2014) Mineralogy of the Martian surface. Annu Rev Earth Planet Sci 42:291–315. doi:10.1146/annurev-earth-060313-055024
Elkins-Tanton LT, Parmentier EM, Hess PC (2003) Magma ocean fractional crystallization and cumulate overturn in terrestrial planets: implications for Mars. Meteorit Planet Sci 38:1753–1771
Elkins-Tanton LT, Hess PC, Parmentier EM (2005) Possible formation of ancient crust on Mars through magma ocean processes. J Geophys Res 110:E12S01. doi:10.1029/2005/E002480
Elkins-Tanton LT (2008) Linked magma ocean solidification and atmospheric growth for Earth and Mars. Earth Plan Sci Lett 271:181–191
Elkins-Tanton L (2012) Magma oceans in the inner solar system. Ann Rev Earth Planet Sci 40:113–139
Encrenaz T et al (1991) The atmospheric composition of Mars–ISM and ground-based observational data. Ann Geophys 9:797–803
Encrenaz T, Lellouch E, Paubert G, Gulkis S (2001) The water vapor vertical distribution on Mars from millimeter transitions of HDO and $H_2^{18}O$. Plan Space Sci 49:731–741

Encrenaz T et al (2004) Hydrogen peroxide on Mars: evidence for spatial and seasonal variations. Icarus 170:424–429
Encrenaz T et al (2005) Infrared imaging spectroscopy of Mars: H_2O mapping and determination of CO_2 isotopic ratios. Icarus 179:43–54
Encrenaz T et al (2006) Seasonal variations of the Martian CO over Hellas as observed by OMEGA/Mars Express. Astron Astrophys 459:265–270
Encrenaz T et al (2011) A stringent upper limit of SO_2 in the Martian atmosphere. Astron Astrophys 530:id.A37
Encrenaz T, Greathouse TK, Lefèvre F, Atreya SK (2012) Hydrogen peroxide on Mars: observations, interpretation and future plans. Plan Space Sci 68:3–17
Encrenaz T et al (2015a) A map of D/H on Mars using high-resolution spectroscopy with EXES aboard SOFIA. European Planetary Science Congress, Nantes, France
Encrenaz T et al (2015b) Seasonal variations of hydrogen peroxide and water vapor on Mars: further indications of heterogeneous chemistry. Astron Astrophys 578:A127
Encrenaz T et al (2016) A map of D/H on Mars in the thermal infrared using EXES aboard SOFIA. Astron Astrophys 586A:A62
Espenak F, Mumma MJ, Kostiuk T, Zipoy D (1991) Ground-based infrared measurements of the global distribution of ozone in the atmosphere of Mars. Icarus 92:252–262
Farmer CB et al (1977) Water vapor observations from the Viking orbiters. J Geophys Res 82:4225–4248
Farrell WM et al (2009) Is the Martian water table hidden from radar view? Geophys Res Lett 36:L15206. doi:10.1029/2009GL038945
Fassett CI, Head JW (2008) The timing of Martian valley network activity: constraints from buffered crater counting. Icarus 195:61–89. doi:10.1016/j.icarus.2007.12.009
Fassett CI, Dickson JL, Head JW, Levy JS, Marchant DR (2010) Supraglacial and proglacial valleys on Amazonian Mars. Icarus 208:86–100. doi:10.1016/j.icarus.2010.02.021
Fast KE et al (2006) Ozone abundance on Mars from infrared heterodyne spectra. II. Validating photochemical models. Icarus 183:396–402
Fast KE et al (2009) Comparison of HIPWAC and Mars Express SPICAM observations of ozone on Mars 2006–2008 and variation from 1993 IRHS observations. Icarus 203:20–27
Fastook JL, Head JW, Marchant DR, Forget F (2008) Tropical mountain glaciers on Mars: altitude-dependence of ice accumulation, accumulation conditions, formation times, glacier dynamics, and implications for planetary spin-axis/orbital history. Icarus 198:305–317
Fastook JL, Head JW, Marchant DR, Forget F, Madeleine J-B (2012) Early Mars climate near the Noachian-Hesperian boundary: independent evidence for cold conditions from basal melting of the south polar ice sheet (Dorsa Argentea Formation) and implications for valley network formation. Icarus 219:25–40
Fedorova A et al (2006) Mars water vapor abundance from SPICAM IR spectrometer: seasonal and geographic distributions. J Geophys Res 111:E09S08
Feldman WC et al (2002) Global distribution of neutrons from Mars: results from Mars Odyssey. Science 297:75–78
Feldman WC, Prettyman TH et al (2004) Global distribution of near-surface hydrogen on Mars. J Geophys Res 109:E09006. doi:10.1029/2003JE002160
Feldman P et al (2011) Rosetta-Alice observations of exospheric hydrogen and oxygen on Mars. Icarus 214:394–399
Filiberto J, Dasgupta R (2011) Fe^{2+}-Mg partitioning between olivine and basaltic melts: applications to genesis of olivine-phyric shergottites and conditions of melting in the Martian interior. Earth Planet Sci Lett 304:527–537
Filiberto J, Dasgupta R (2015) Constraints on the depth and thermal vigor of melting in the Martian mantle. J Geophys Res 120:109–122
Filiberto J et al (2016) A review of volatiles in the Martian interior. Meteorit Planet Sci (in revision)
Flahaut J, Quantin C, Clenet H, Allemand P, Mustard JF, Thomas P (2012) Pristine Noachian crust and key geologic transitions in the walls of Valles Marineris: insights into early igneous processes on Mars. Icarus 221:420–435. doi:10.1016/j.icarus.2011.12.027
Flahaut J, Quantin C, Allemand P, Thomas P, Le Deit L (2010) Identification, repartition and possible origins of sulfates in Capri Chasma (Mars), inferred from CRISM data. J Geophys Res 115:E11007. doi:10.1029/2009JE003566
Folkner WM, Yoder CF, Yuan DN, Standish EM, Preston RA (1997) Interior structure and seasonal mass redistribution of Mars from radio tracking of Mars Pathfinder. Science 278:1749–1752

Foley CN, Economou TE, Clayton RN, Dietrich W (2003) Calibration of the Mars Pathfinder alpha proton X-ray spectrometer. J Geophys Res 108(E12):8095. doi:10.1029/2002JE002018
Foley BJ, Driscoll PE (2016) Whole planet coupling between climate, mantle, and core: implications for rocky planet evolution. Geochem Geophys Geosyst 17:1885–1914. doi:10.1002/2015GC006210
Fonti S, Marzo GA (2010) Mapping the methane on Mars. Astron Astrophys 512:A51
Fonti S, Mancarella F, Liuzzi G, Roush TL, Chizek Frouard M, Murphy J, Blanco A (2015) Revisiting the identification of methane on Mars using TES data. Astron Astrophys 581:A136
Forget F, Haberle RM, Montmessin F et al (2006) Formation of glaciers on Mars by atmospheric precipitation at high obliquity. Science 311:368–371
Forget F et al (2009) Density and temperatures of the upper Martian atmosphere measured by stellar occultations with Mars Express SPICAM. J Geophys Res 114:E01004
Forget F et al (2013) 3D modeling of the early Martian climate under a denser CO_2 atmosphere: temperatures and CO_2 ice clouds. Icarus 222:81–99
Formisano V, Atreya SK, Encrenaz T, Ignatiev N, Giuranna M (2004) Detection of methane in the atmosphere of Mars. Science 306:1758–1761
Fouchet T, Lellouch E (2000) Vapor pressure isotope fractionation effects in planetary atmospheres: application to deuterium. Icarus 144:114–123
Fouchet T et al (2007) Martian water vapor: Mars Express PFS/LW observations. Icarus 190:32–49
Fox J, Dalgarno A (1979) Ionization, luminosity, and heating of the upper atmosphere of Mars. J Geophys Res 84:7315–7333
Fraeman AA, Korenaga J (2010) The influence of mantle melting on the evolution of Mars. Icarus 210:43–57. doi:10.1016/j.icarus.2010.06.030
Franz H et al (2015) Reevaluated martian atmospheric mixing ratios from the mass spectrometer on the Curiosity rover. Plan Space Sci 109:154–158
French HM (1996) The periglacial environment, 2nd edn. Longman, London
Fressinet C et al (2015) Organic molecules in the Sheepbed Mudstone Gale Crater, Mars. J Geophys Res 120:495–514. doi:10.1002/2014JE004737
Frey H, Schultz RA (1988) Large impact basins and the mega-impact origin for the crustal dichotomy on Mars. Geophys Res Lett 15:229–232
Frey HV (2006) Impact constraints on, and a chronology for, early events is the history of Mars. J Geophys Res 111(29):E08S91. doi:10.1029/2005JE002449
Frey H (2008) Ages of very large impact basins on Mars: implications for the late heavy bombardment in the inner solar system. Geophys Res Lett 35:L13203. doi:10.1029/2008GL033515
Gainey SR, Elwood Madden ME (2012) Kinetics of methane clathrate formation and dissociation under Mars relevant conditions. Icarus 218:513–524
Gardin E, Allemand P, Quantin C, Thollot P (2010) Defrosting, dark flow and dune activity on Mars. J Geophys Res 115:E06016
Gaudin A, Dehouck E, Mangold N (2011) Evidence for weathering on early Mars from a comparison with terrestrial weathering profiles. Icarus 216:257–268
Geissler PE (2014) The birth and death of transverse aeolian ridges on Mars. J Geophys Res 119:2583–2599
Geminale A, Formisano V, Giuranna M (2008) Methane in Martian atmosphere: average spatial, diurnal and seasonal behavior. Planet Space Sci 56:1194–1203
Geminale A, Formisano V (2009) Study of the oxygen dayglow in Martian atmosphere with the Planetary Fourier Spectrometer on board Mars Express. EGU General Assembly, 19–24 April 2009, Vienna, Austria
Geminale A, Formisano V, Sindoni G (2011) Mapping methane with PFS-MEx data. Planet Space Sci 59:137–158
Gendrin A et al (2005) Sulfates in martian layered terrains: the OMEGA/Mars Express view. Science 307:1587–1591
Gerard J-C et al (2015) Concurrent observations of ultraviolet aurora and energetic electron precipitation with Mars Express. J Geophys Res 120 (2015). doi:10.1002/2015JA021150
Gillmann C, Lognonné P, Moreira M (2011) Volatiles in the atmosphere of Mars: the effects of volcanism and escape constrained by isotopic data. Earth Planet Sci Lett 303:299–309
Girazian Z, Withers P (2013) The dependence of peak electron density in the ionosphere of Mars on solar irradiance. Geophys Res Lett 40:1960–1964
Golombek MP, Tanaka KL, Franklin BJ (1996) Extension across Tempe Terra, Mars, from measurements of fault scarp widths and deformed craters. J Geophys Res 101:26119–26130

Golombek MP, Anderson FS, Zuber MT (2001) Martian wrinkle ridge topography: evidence for subsurface faults from MOLA. J Geophys Res 106:23811–23821
Golombek MP, Phillips RJ (2009) Mars tectonics. In: Watters TR, Schultz RA (eds) Planetary tectonics. Cambridge University Press, Cambridge, pp 180–232
Gómez-Elvira J et al (2012) REMS: the environmental sensor suite for the Mars Science Laboratory Rover. Space Sci Rev 170:583–640
Gooding JL, Wentworth SJ, Zolensky ME (1991) Aqueous alteration of the Nakhla meteorite. Meteoritics 26:135–143
Goudge TA, Head JW, Mustard JF, Fassett CI (2012) An analysis of open-basin lake deposits on Mars: evidence for the nature of associated lacustrine deposits and post-lacustrine modification processes. Icarus 219:211–229. doi:10.1016/j.icarus.2012.02.027
Goudge TA, Fassett CI, Head JW, Mustard JF, Aureli KL (2016) Insights into surface runoff on early Mars from paleolake basin morphology and stratigraphy. Geology 44:419–422
Grant JA (2000) Valley formation in Margaritifer Sinus Mars by precipitation-recharged ground-water sapping. Geology 28:223–226
Grant JA, Wilson SA, Mangold N, Calef F, Grotzinger JP (2014) The timing of alluvial activity in Gale Crater, Mars. Geophys Res Lett 41:1142–1149
Grimm RE, Solomon SC (1986) Tectonic tests of proposed polar wander paths for Mars and the Moon. Icarus 65:110–121
Greeley R, Schneid BD (1991) Magma generation and comparisons with Earth, Moon, and Venus. Science 254:996–998
Greeley R, Spudis PD (1981) Volcanism on Mars. Rev Geophys 19:13–41. doi:10.1029/RG019i001p00013
Greeley R, Schneid BD (1991) Magma generation on Mars: amounts, rates, and comparisons with Earth, Moon, and Venus. Science 254:996–998
Greenwood (2008) Hydrogen isotope evidence for loss of water from Mars through time. Geophys Res Let 35:L05203
Grima C et al (2009) North polar deposits of Mars: extreme purity of the water ice. Geophys Res Lett 36:L03203. doi:10.1029/2008GL036326
Grott M (2005) Late crustal growth on Mars: evidence from lithospheric extension. Geophys Res Lett 32:L23201
Grott M, Breuer D (2010) On the spatial variability of the martian elastic lithosphere thickness: evidence for mantle plumes? J Geophys Res 115:E03005
Grott M et al (2013) Long-term evolution of the Martian crust-mantle system. Space Sci Rev 174:49–111
Grotzinger JP, Milliken, RE (2012) The sedimentary rock record of Mars: distribution, origins, and global stratigraphy. In: Grotzinger JP, Milliken RE (eds) Sedimentary geology of Mars SEPM Special Publication 102, pp 1–48
Grotzinger JP, the MSL Science Team, (2014) A Habitable fluvio-lacustrine environment at Yellowknife Bay. Gale Crater. Mars. Science 343: doi:10.1126/science.1242777
Grotzinger JP et al (2015) Deposition, exhumation, and paleoclimate of an ancient lake deposit. Gale crater. Mars. Science 350: doi:10.1126/science.aac7575
Gulick VC, Baker VR (1990) Origin and evolution of valleys on Martian volcanoes. J Geophys Res 95:14325–14344
Gulick VC (1993) Magmatic intrusions and hydrothermal systems: implications for the formation of small Martian valleys. Ph.D. Thesis, University of Arizona, Tucson
Gulick VC, Tyler D, McKay CP, Haberle RM (1997) Effects and lifetimes of ocean-induced CO_2 pulses on Mars: implications for fluvial valley formation. Icarus 130:68–86
Gurnett DA et al (2005) Radar soundings of the ionosphere of Mars. Science 310:1929–1933
Gurnett DA et al (2008) An overview of radar soundings of the Martian ionosphere from the Mars Express spacecraft. Adv Space Res 41:1335–1346. doi:10.1016/j.asr.2007.01.062
Gurnett DA et al (2015) An ionized layer in the upper atmosphere of Mars caused by dust impacts from comet Siding Spring. Geophys Res Lett 42: doi:10.1002/2015GL063726
Gurwell MA et al (2000) Submillimeter wave astronomy satellite observations of the Martian atmosphere: temperature and vertical distribution of water vapor. Astrophys J 539:L143–L146
Gurwell MA, Bergin EA, Melnick GJ, Tolls V (2005) Mars surface and atmospheric temperature during the 2001 global dust storm. Icarus 175:23–31
Grassi D, Fiorenza C, Zasova LV (2005) The Martian atmosphere above great volcanoes: Early Planetary Fourier spectrometer observations. Plan Space Sci 53:1053–1064

Grassi D, Formisano V, Forget F et al (2007) The Martian atmosphere in the region of Hellas basin as observed by the Planetary Fourier spectrometer (PFS-MEX). Plan Space Sci 55:1346–1357
Gronoff G et al (2014) The precipitation of keV energetic oxygen ions at Mars and their effects during the comet Siding Spring approach. Geophys Res Lett 41:4844–4850
Haberle RM et al (1999) General circulation model simulations of the Mars Pathfinder atmospheric structure investigation/meteorology data. J Geophys Res 104:8957–8974
Halliday AN, Wanke H, Birck J-L, Clayton RN (2001) The accretion, composition and early differentiation of Mars. Space Sci Rev 96:197–230
Hamilton VE, Christensen PR (2005) Evidence for extensive, olivine-rich bedrock on Mars. Geology 33:433–436
Hanna JC, Phillips RJ (2006) Tectonic pressurization of aquifers in the formation of Mangala and Athabasca Valles. J Geophys Res 111:E03003
Hanel R et al (1972) Investigation of the Martian environment by infrared spectroscopy on Mariner 9. Icarus 17:423–442
Hahn BC et al (2007) Mars Odyssey Gamma Ray Spectrometer elemental abundances and apparent relative surface age: implications for Martian crustal evolution. J Geophys Res 112:E03S11. doi:10.1029/2006JE002821
Halevy I, Fischer WW, Eiler JM (2011) Carbonates in the Martian meteorite Allan Hills 84001 formed at $18+/-4\,^{\circ}C$ in a near-surface aqueous environment. Proc Natl Acad Sci USA 108(41):16895–16899
Hansen CJ et al (2010) HiRISE observations of gas sublimation-driven activity in Mars' southern polar regions: I. Erosion of the surface. Icarus 205:283–295
Hansen CJ et al (2013) Observations of the northern seasonal polar cap on Mars: I. Spring sublimation activity and processes. Icarus 225:881–897
Hanson W et al (1977) The Martian ionosphere as observed by the Viking retarding potential analyzers. J Geophys Res 82:4351–4363
Hanson WB, Mantas GP (1988) Viking electron temperature measurements–evidence for a magnetic field in the Martian ionosphere. J Geophys Res 93:7538–7544
Harper CL, Nyquist LE, Bansal B, Wiesmann H, Shih C-Y (1995) Rapid accretion and early differentiation of Mars indicated by 142Nd/144Nd in SNC meteorites. Science 267:213–217
Harrison KP, Grimm RE (2005) Groundwater controlled valley networks and the decline of surface runoff on early Mars. J Geophys Res 110:E12S16. doi:10.1029/2005JE002455
Hartmann WK (2005) Martian cratering 8: isochron refinement and the chronology of Mars. Icarus 174:294–320
Hartmann WK, Neukum G (2001) Cratering chronology and the evolution of Mars. Space Sci Rev 96:165–194
Hartmann WK, Ansan V, Berman DC, Mangold N, Forget F (2014) Comprehensive analysis of glaciated Martian Crater Greg. Icarus 228:96–120. doi:10.1016/j.icarus.2013.09.016
Hartogh P et al (2010) Herschel/HIFI observations of Mars: first detection of O_2 at submillimetre wavelengths and upper limits on HCl and H_2O_2. Astron Astrophys 521:49–52
Hauber E et al (2005) Discovery of a flank caldera and very young glacial activity at Hecates Tholus, Mars. Nature 434:356–361
Hauber E, van Gasselt S, Chapman MG, Neukum G (2008) Geomorphic evidence for former lobate debris aprons at low latitudes on Mars: Indicators of the Martian paleoclimate. J Geophys Res-Planets 113:E02007
Hauber E, Bleacher J, Gwinner K, Williams D, Greeley R (2009) The topography and morphology of low shields and associated land- forms of plains volcanism in the Tharsis region of Mars. J Volcanol Geotherm Res 185:69–95
Hauber E, Brož P, Jager F, JodłowskiP PT (2011) Very recent and wide-spread basaltic volcanism on Mars. Geophys Res Lett 38:L10201
Hauber E et al (2014) Asynchronous formation of Hesperian and Amazonian-aged deltas on Mars and implications for climate. J Geophys Res 118: doi:10.1002/jgre.20107
Hauck SA, Phillips RJ (2002) Thermal and crustal evolution of Mars. J Geophys Res 107(E7):5052. doi:10.1029/2001JE001801
Head JW, Hiesinger H, Ivanov MA, Kreslavsky MA, Pratt S, Thomson BJ (1999) Possible ancient oceans on Mars: evidence from Mars Orbiter Laser Altimeter data. Science 286:2134–2137

Head JW, Kreslavsky MA, Pratt S (2002) Northern lowlands of Mars: evidence for widespread volcanic flooding and tectonic deformation in the Hesperian Period. J Geophys Res 107(E1):5003. doi:10.1029/2000JE001445
Head JW, Marchant DR (2003) Cold-based mountain glaciers on Mars: Western Arsia Mons. Geology 31:641
Head JW, Mustard JF, Milliken RE, Marchant DR (2003) Recent ice ages on Mars. Nature 426:797–802
Head JW, Neukum G, Jaumann R et al (2005) Tropical to mid-latitude snow and ice accumulation, flow and glaciation on Mars. Nature 434:346–351
Head JW, Marchant DR, Dickson JL, Kress AM, Baker DM (2010) Northern mid-latitude glaciation in the Late Amazonian period of Mars: criteria for the recognition of debris-covered glacier and valley glacier land system deposits. Earth Planet Space Sci 294:306–320
Head JW, Marchant DR (2014) The climate history of early Mars: insights from the Antarctic McMurdo Dry Valleys hydrologic system. Antarct Sci 26:774–800. doi:10.1017/S0954102014000686
Hecht MH et al (2009) Detection of perchlorate and the soluble chemistry of martian soil at the Phoenix Lander Site. Science 325:64–67
Herkenhoff KE, Plaut JJ, Nowicki SA (1997) Surface age and resurfacing rate of the north polar layered terrain on Mars. Lunar Planet Sci Conf XXVIII:551–552
Herzberg C, Condie K, Corenaga K (2010) Thermal history of the Earth and its petrological expression. Earth Plan Sci Lett 292:79–88
Hess PC, Parmentier EM (1995) A model for the thermal and chemical evolution of the Moon's interior: implications for the onset of mare volcanism. Earth Planet Sci Lett 134:501–514
Hiesinger H, Head JW (2004) The Syrtis Major volcanic province, Mars: synthesis from Mars Global Surveyor data. J Geophys Res 109:E01004
Hinson DP, Wilson RJ (2004) Temperature inversions, thermal tides, and water ice clouds in the Martian tropics. J Geophys Res 109:E01002
Hinson DP et al (1999) Initial results from radio occultation measurements with Mars Global Surveyor. J Geophys Res 104:26997–27012
Hobley DEJ, Howard AD, Moore JM (2014) Fresh shallow valleys in the martian midlatitudes as features formed by meltwater flow beneath ice. J Geophys Res 119:128–153
Hofmann AW, Jochum KP, Seufert M, White WM (1986) Nb and Pb in oceanic basalts: new constraints on mantle evolution. Earth Planet Sci Lett 79:33–45
Holt JW et al (2008) Radar sounding evidence for buried glaciers in the southern mid-latitudes of Mars. Science 322:1235–1238
Hood LL, Zakharian A (2001) Mapping and modeling of magnetic anomalies in the northern polar region of Mars. J Geophys Res 106:14601–14619
Hood LL, Richmond NC, Pierazzo E, Rochette P (2003) Distribution of crustal magnetic fields on Mars: shock effects of basin-forming impacts. Geophys Res Lett 30:1281–1284. doi:10.1029/2002GL016657
Hood LL, Young CY, Richmond NC, Harrison KP (2005) Modeling of major martian magnetic anomalies: further evidence for polar reorientations during the Noachian. Icarus 177:144–173
Hood LL, Kiefer WS, Langlais B (2010) Parallel modeling of the Apollinaris Patera magnetic and gravity anomalies. In: Lunar and Planetery Science Conference, vol. XXXXI abstract #1533, p. 2006
Howard AD (1988) Introduction: groundwater sapping on Mars and Earth. In: Howard AD, Kochel RC, Holt HE (eds) Sapping features of the Colorado Plateau. NASA SP-491, USA, pp 1–5
Hu R, Kass DM, Ehlmann BL, Yung Y (2015) Tracing the fate of carbonate and the atmospheric evolution of Mars. Nat Commun 6. id. 10003. doi:10.1038/ncomms10003
Hudson TL et al (2009) Laboratory experiments and models of diffusive emplacement of ground ice on Mars. J Geophys Res 114(E1):E01002. doi:10.1029/2008JE003149
Humayun M et al (2013) Origin and age of the earliest Martian crust from meteorite NWA7533. Nature 503:513–517
Hunten DM (1979) Possible oxidant sources in the atmosphere and surface of Mars. J Mol Evol 14:71–78
Hynek BM, Phillips RJ (2001) Evidence for extensive denudation of the Martian highlands. Geology 29(5):407–410. doi:10.1130/0091-7613
Hynek BM, Beach M, Hoke MR (2010) Updated global map of Martian valley networks. J Geophys Res 115(E9):E09008
Irwin RP, Howard AD (2002) Drainage basin evolution in Noachian Terra Cimmeria. Mars. J Geophys Res 107(E7):5056. doi:10.1029/2001JE001818

Irwin RP, Craddock RA, Howard AD (2005) Interior channels in Martian valley networks: discharge and runoff production. Geology 33(6):489–492. doi:10.1130/G21333.1
Ivanov BA (2001) Mars/Moon cratering rate ratio estimates. Space Sci Rev 96:87–104
Jaeger WL, Keszthelyi LP, McEwen AS, Dundas CM, Russel RS (2007) Athabasca Valles, Mars: a lava-draped channel system. Science 317:1709. doi:10.1126/science.1143315
Jain SK et al (2015) The structure and variability of Mars upper atmosphere as seen in MAVEN/IUVS dayglow observations. Geophys Res Lett 42: doi:10.1002/2015GL065419
Jakosky BM (1990) Mars atmospheric D/H–consistent with polar volatile theory? J Geophys Res 95:1475–1480
Jakosky BM, Haberle RM (1992) The seasonal behavior of water on Mars. In: Kieffer HH et al (eds) Mars. University of Arizona Press, Tucson
Jaskosky B, Jones JH (1997) The history of Martian volatiles. Rev Geophys 35:1–16
Jakosky BM et al (2015) The Mars atmosphere and volatile evolution (MAVEN) mission. Space Sci Rev 195:3–48
Jakosky B et al (2015) MAVEN observations of the response of Mars to an interplanetary coronal mass ejection. Science 350(6261):id0210
Jaumann R et al (2005) Interior channels in Martian valleys: constraints on fluvial erosion by measurements of the Mars Express High Resolution Stereo Camera. Geophys Res Lett 32:L16203. doi:10.1029/2005GL023415
Jaumann R et al (2015) Quantifying geological processes on Mars–results of the high resolution stereo camera (HRSC) on Mars Express. Planet Space Sci 112:53–97
Johnsson A et al (2012) Periglacial mass wasting landforms on Mars suggestive of transient liquid water in the recent past: insights from solifluction lobes on Svalbard. Icarus 218:489–505
Jones AP, McEwen AS, Tornabene LL, Baker VR, Melosh HJ, Berman DC (2011) A geomorphic analysis of Hale crater, Mars: the effects of impact into ice-rich crust. Icarus 211:259–272
Jones JH, Neal CR, Ely JC (2003) Signatures of the highly siderophile elements in the SNC meteorites and Mars: A review and petrologic synthesis. Chem Geol 196:21–41
Jöns H-P (1984) Sedimentary basins and mud flows in the northern lowlands of Mars. Lunar Planet Sci XV:417–418
Khan A, Connolly JAD (2008) Constraining the composition and thermal state of Mars from inversion of geophysical data. J Geophys Res 113:E07003
Kakar RK, Walters JW, Wilson WJ (1977) Mars–microwave detection of carbon monoxide. Science 196:1090–1091
Kaplan LD, Connes J, Connes P (1969) Carbon monoxide in the Martian atmosphere. Astrophys J 157:L187–L190
Karunatillake S et al (2009) Chemically striking regions on Mars and Stealth revisited. J Geophys Res 114:E12001
Keating GM et al (1998) The structure of the upper atmosphere of Mars: in situ accelerometer measurements from Mars Global Surveyor. Science 279(5357):1672–1674
Kerber L, Head JW, Madeleine J-B, Forget F, Wilson L (2012) The dispersal of pyroclasts from ancient explosive volcanoes on Mars: implications for the friable layered deposits. Icarus 219:358–381
Kieffer HH (1979) Mars south polar spring and summer temperatures–residual CO_2 frost. J Geophys Res 84:8263–8288
Kieffer HH, Christensen PR, Titus T (2006) CO_2 jets formed by sublimation beneath translucent slab ice in Mars' seasonal south polar ice cap. Nature 442:793–796
King PL, McLennan SM (2010) Sulfur on Mars. Elements 6:107–112
Kite ES, Matsuyama I, Manga M, Taylor Perron J, Mitrovica JX (2009) True Polar Wander driven by late-stage volcanism and the distribution of paleopolar deposits on Mars. Earth Planet Sci Lett 280:254–267
Kite ES, Lewis KW, Lamb MP, Newman CE, Richardson MI (2013) Growth and form of the mound in Gale Crater, Mars: slope-wind enhanced erosion and transport. Geology 41:543–546. doi:10.1130/G3309.1
Kleine T, Mezger K, Münker C, Palme H, Bischoff A (2004) ^{182}Hf-^{182}W isotope systematics of chondrites, eucrites, martian meteorites: chronology of core formation and early mantle differentiation in Vesta and Mars. Geochim Cosmochim Acta 68:5150–5188
Kletetschka G, Wasilewski PJ, Taylor PT (2000) Unique thermoremanent magnetization of multidomain sized hematite: implications for magnetic anomalies. Earth Planet Sci Lett 176:469–479

Kliore AJ, Fjeldbo G, Seidel BL et al (1973) S band radio occultation measurements of the atmosphere and topography of Mars with Mariner 9: extended mission coverage of polar and intermediate latitudes. J Geophys Res 78:4331–4351
Koeppen WC, Hamilton VE (2008) Global distribution, composition, and abundance of olivine on the surface of Mars from thermal infrared data. J Geophys Res 113:E05001
Komar PD (1979) Comparisons of the hydraulics of water flows in Martian outflow channels with flows of similar scale on Earth. Icarus 37:156–181
Komatsu G, Baker VR (1997) Paleohydrology and flood geomorphology of Ares Vallis. J Geophys Res 102:4151–4160
Komatsu G et al (2009) Paleolakes, paleofloods, and depressions in Aurorae and Ophir Plana, Mars: connectivity of surface and subsurface hydrological systems. Icarus 201:474–491
Kopf et al (2008) Transient layers in the topside ionosphere of Mars. Geophys Res Lett 35:L17102. doi:10.1029/2008GL034948
Korablev OI, Ackerman M, Krasnopolsky VA et al (1993) Tentative identification of formaldehyde in the Martian atmosphere. Planet Space Sci 41:441–451
Kossacki KJ, Leliwa-Kopystynski J (2004) Non uniform seasonal defrosting of subpolar dune field on Mars. Icarus 168:201–204
Kraal ER et al (2008) Martian stepped-delta formation by rapid water release. Nature 451:973–972. doi:10.1038/nature06615
Krasnopolsky VA (2015) Variations of the HDO/H_2O ratio in the martian atmosphere and loss of water from Mars. Icarus 257:377–385
Krasnopolsky VA, Mumma MJ, Bjoraker GL, Jennings DE (1996) Oxygen and carbon isotope ratios in Martian carbon dioxide: measurements and implications for atmospheric evolution. Icarus 124:553–568
Krasnopolsky VA, Bjoraker GL, Mumma MJ, Jenning DE (1997) High-resolution spectroscopy of Mars at 3.7 and 8 μm: a sensitive search of H_2O_2, H_2CO, HCl, and CH_4, and detection of HDO. J Geophys Res 102:6525–6534
Krasnopolsky VA, Mumma MJ, Gladstone RG (1998) Detection of atomic deuterium in the upper atmosphere of Mars. Science 280:1576
Krasnopolsky VA, Maillard J-P, Owen T (2004) Detection of methane in the martian atmosphere: evidence for life? Icarus 172:537–547
Krasnopolsky VA (2009) Seasonal variations of photochemical tracers at low and middle latitudes on Mars: observations and models. Icarus 201:564–569
Kreslavsky MA, Head JW III (2002) Mars: nature and evolution of young latitude-dependent water-ice-rich mantle. Geophys Res Lett 29:1719. doi:10.1029/2002GL015392
Kurokawa H, Sato M, Ushioda M et al (2014) Evolution of water reservoirs on Mars: constraints from hydrogen isotopes in martian meteorites. Earth Plan Sci Lett 394:179–185
Lammer H (2013) Outgassing history and escape of the martian atmosphere and water inventory. Space Sci Rev 174:113–154
Langevin Y, Poulet F, Bibring J-P, Gondet B (2005) Sulfates in the north polar region of Mars detected by OMEGA/Mars Express. Science 307:1584–1586
Langlais B, Purucker M (2007) A polar magnetic paleopole associated with Apollinaris Patera, Mars. Planet Space Sci 55:270–279
Langlais B, Lesur V, Purucker M, Connerney J, Mandea M (2010) Crustal magnetic fields of terrestrial planets. Space Sci Rev 152: doi:10.1007/s11214-009-9557-y
Lanza NL et al (2014) High manganese concentrations in rocks at Gale crater. Mars. Geophys Res Let 41: doi:10.1002/2014GL060329
Laskar J, Levrard B, Mustard JF (2002) Orbital forcing of the martian polar layered deposits. Nature 419:375–377
Laskar J et al (2004) Long term evolution and chaotic diffusion of the insolation quantities of Mars. Icarus 170:343–364
Lapotre et al (2016) Large wind-ripples on Mars: a record of atmospheric evolution. Science 353:55–58
Lasue J et al (2013) Quantitative assessments of the martian hydrosphere. Space Sci Rev 174:155–212. doi:10.1007/s11214-012-9946-5
Leblanc F et al (2008) Observations of aurorae by SPICAM ultraviolet spectrograph on board Mars Express: simultaneous ASPERA-3 and MARSIS measurements. J Geophys Res Space Phys 113:A08311

Leblanc F et al (2007) On Martian nitrogen dayglow emission observed by SPICAM UV spectrograph/Mars Express. Geophys Res Lett 34:L02206
Leblanc F, Chaufray JY, Lilensten J, Witasse O, Bertaux J-L (2006) Martian dayglow as seen by the SPICAM UV spectrograph on Mars Express. J Geophys Res 111:E09S11
Leblanc F et al (2006) Origins of the Martian aurora observed by spectroscopy for investigation of characteristics of the atmosphere of Mars (SPICAM) on board Mars Express. J Geophys Res Space Phys 111:A09313
Lebonnois S et al (2006) Vertical distribution of ozone on Mars as measured by SPICAM/Mars Express using stellar occultations. J Geophys Res 111:ID E09S05
Le Deit L et al (2012) Extensive surface pedogenic alteration of the Martian Noachian crust suggested by plateau phyllosilicates around Valles Marineris. J Geophys Res Planets 117: doi:10.1029/2011JE003983
Lee DC, Halliday AN (1997) Core formation on Mars and differentiated Asteroids. Nature 388:854–857
Lee JY, Marti K, Severinghaus P, Kawamura K, Yoo HS, Lee JB, Kim JS (2006) A redetermination of the isotopic abundances of atmospheric Ar. Geochim Cosmochim Acta 70:4507–4512
Lefèvre F, Perrier S, Quemerais E, Montmessin F, Bertaux J-L, Lebonnois S, Forget F, Clancy RT, Fast K (2006) Toward a quantitative understanding of Martian ozone. In: Forget F et al (eds) Second workshop on Mars atmosphere modelling and observations. Granada, Spain, p 522
Lefèvre F, Forget F (2009) Observed variations of methane on Mars unexplained by known atmospheric chemistry and physics. Nature 460:720–723
Lefèvre F, Bertaux J-L, Clancy RT et al (2008) Heterogeneous chemistry in the atmosphere of Mars. Nature 454:971–975
Lefort A, Russell PS, Thomas N, McEwen AS, Dundas CM, Kirk RL (2009) Observations of periglacial landforms in Utopia Planitia with the high resolution imaging science experiment (HiRISE). J Geophys Res 114:E04005
Leopold LB, Wolman MG, Miller JP (1972) Fluvial processes in geomorphology. Dover, Mineola
Léveillé RJ et al (2014) Chemistry of fracture-filling raised ridges in Yellowknife Bay, Gale Crater: window into past aqueous activity and habitability on Mars. J Geophys Res 119:2398–2415. doi:10.1002/2014JE004620
Leverington DW (2004) Volcanic rilles, streamlined islands, and the origin of outflow channels on Mars. J Geophys Res 109:E10011
Levrard B, Forget F, Montmessin F, Laskar J (2007) Recent formation and evolution of northern Martian polar layered deposits as inferred from a Global Climate Model. J Geophys Res 112:E06012
Levy JS, Head JW, Marchant DR (2007) Lineated valley fill and lobate debris aprons stratigraphy in Nilosyrtis Mensae, Mars: evidence for phases of glacial modification of the dichotomy boundary. J Geophys Res 112:E08004. doi:10.1029/2006JE002852
Levy JS et al (2009) Concentric crater fill in Utopia Planitia: timing and transitions between glacial and periglacial processes. Icarus 202: doi:10.1016/j.icarus.2009.1002.1018
Levy JS et al (2010) Thermal contraction crack polygons on Mars: a synthesis from HiRISE, Phoenix, and terrestrial analog studies. Icarus 206:229–252
Lewis KW et al (2008) Quasi-periodic bedding in the sedimentary rock record of Mars. Science 322:1532–1535
Lewis KW, Aharonson O (2014) Occurrence and origin of rhythmic sedimentary rocks on Mars. J Geophys Res Planets 119:1432–1457
Li H, Robinson MS, Jurdy DM (2005) Origin of martian northern hemisphere mid-latitude lobate debris aprons. Icarus 176:382–394
Liemohn MW et al (2007) Numerical modeling of the magnetic topology near Mars auroral observations. Geophys Res Lett 34:L24202
Lillis RJ, Frey HV, Manga M (2008) Rapid decrease in Martian crustal magnetization in the Noachian era: implications for the dynamo and climate of early Mars. Geophys Res Lett 35
Lillis RJ, Manga M, Mitchell D, Lin R, Acuna MA (2006) Unusual magnetic signature of the Hadriaca Patera volcano: implications for early Mars. Geophys Res Lett 33: doi:10.1029/2005GL024905
Lillis R, Fang X (2015) Electron impact ionization in the Martian atmosphere: interplay between scattering and crustal magnetic field effects. J Geophys Res. doi:10.1002/2015JE004841
Lindal GF, Hotz HB, Sweetnam DN et al (1979) Viking radio occultation measurements of the atmosphere and topography of Mars–data acquired during 1 Martian year of tracking. J Geophys Res 84:8443–8456
Liu SC, Donahue TM (1976) Regulation of hydrogen and oxygen escape from Mars. Icarus 28:231–246

Lodders K (1998) A survey of SNC meteorite whole-rock compositions. Meteorit Planet Sci Suppl 33:183–190
Loizeau D et al (2010) Stratigraphy in the Mawrth Vallis region through OMEGA, HRSC color imagery and DTM. Icarus 205:396–418
Loizeau D, Werner SC, Mangold N, Bibring J-P, Vago JL (2012) Chronology of deposition and alteration in the Mawrth Vallis region. Planet Space Sci, Mars. doi:10.1016/j.pss.2012.06.023
Loizeau D et al (2012) Characterization of hydrated silicate-bearing outcrops in Tyrrhena Terra, Mars: implications to the alteration history of Mars. Icarus 219:476–497
Loizeau et al (2007) Phyllosilicates in the Mawrth Vallis region of Mars. J Geophys Res 112:E08S08
Longhi JE, Knittle JR, Holloway H, Wänke H (1992) The bulk composition, mineralogy and internal structure of Mars. In: Kieffer HH et al (eds) Mars. University of Arizona Press, Tucson
Lucchitta BK (1984) Ice and debris in the fretted terrain, Mars. J Geophys Res 89:B409–B418 (Proceedings of 14th lunar planetery science conference)
Lucchitta BK, McEwen AS, Clow CD, Geissler RB, Singer RB, Schultz RA, Squyres SW (1992) The canyon system on Mars. In: Kieffer HH et al (eds) Mars. University of Arizona Press, Tucson
Luhmann J (2009) Do magnetospheres really shield planetary atmospheres from solar wind interaction-related erosion? 43rd ESLAB symposium. Venus-Earth-Mars, ESTEC, Comparative planetology
Lundin R et al (2004) Solar wind-induced atmospheric erosion at Mars: first results from ASPERA-3 on Mars Express. Science 305:1933–1936
Lundin R et al (2006) Auroral plasma acceleration above Martian magnetic anomalies. Space Sci Rev 126:333–354
Lundin R et al (2013) Solar cycle effects on the ion escape from Mars. Geophys Res Lett 40:6028–6032
Lyons JR, Manning C, Nimmo F (2005) Formation of methane on Mars by fluid-rock interaction in the crust. Geophys Res Lett 32:L13201
Ma Y et al (2014) Effects of crustal field rotation on the solar wind plasma interaction with Mars. Geophys Res Lett 41:6563–6569
Madeleine J-B, Forget F, Millourd E et al (2012) The influence of radiatively active water ice clouds on the Martian climate. Geophys Res Lett 39:L23202
Maguire WC (1977) Martian isotopic ratios and upper limits for possible minor constituents as derived from Mariner 9 infrared spectrometer data. Icarus 32:85–97
Mahaffy P et al (2013) Abundance and isotopic composition of gases in the Martian atmosphere from the Curiosity Rover. Science 341:260–263
Mahaffy PR, Webster CR, Stern JC (2015) The imprint of atmospheric evolution in the D/H of Hesperian clay minerals on Mars. Science 347:412–414
Maltagliati L, Montmessin F, Fedorova A et al (2011) Evidence of water vapor in excess of saturation in the atmosphere of Mars. Science 333:1868–1871
Malin MC, Edgett KS (2000a) Sedimentary rocks of early Mars. Science 290:1927–1937
Malin MC, Edgett KS (2000b) Evidence for recent groundwater seepage and surface runoff on Mars. Science 288:2330–2335
Malin MC, Edgett KS (2003) Evidence for persistent flow and aqueous sedimentation on early Mars. Science 302:1931–1934
Manga M (2004) Martian floods at Cerberus Fossae can be produced by groundwater discharges. Geophys Res Lett 31:L02702
Mangold N, Allemand P, Thomas P, Vidal G (2000) Chronology of compressional deformation on Mars: evidence for a single and global origin. Planet Space Sci 48:1201–1211
Mangold N, Allemand P, Thomas P (1998) Wrinkle ridges on Mars: structural analysis and evidence for shallow deformation controlled by icy decollements. Planet Space Sci 46:345–356
Mangold N, Allemand P (2001) Topographic analysis of features related to ice on Mars. Geophys Res Lett 28:407–411
Mangold N, Allemand P, Thomas P, Duval P, Géraud Y (2002) Experimental and theoretical deformation of ice-rock mixtures: implications on rheology and ice content of Martian permafrost. Planet Space Sci 50:385–401
Mangold N (2003) Geomorphic analysis of lobate debris aprons on Mars at MOC scale: evidence for ice sublimation initiated by fractures. J Geophys Res 108: doi:10.1029/2002001885
Mangold N, Costard F, Forget F (2003) Debris flows over sand dunes on Mars: evidence for liquid water. J Geophys Res 108: doi:10.1029/2002JE001958

Mangold N, Maurice S, Feldman W, Costard F, Forget F (2004a) Spatial relationships between patterned ground and ground ice detected by the Neutron Spectrometer on Mars. J Geophys Res Planet 109:E08001. doi:10.1029/2004JE002235
Mangold N, Quantin C, Ansan V, Delacourt C, Allemand P (2004b) Evidence for precipitation on Mars from dendritic valleys in Valles Marineris area. Science 305:78–81
Mangold N (2005) High latitude patterned ground on Mars: classification, distribution and climatic control. Icarus 174:336–359
Mangold N (2012) Fluvial landforms on fresh ejecta craters. Planet Space Sci 62:69–85
Mangold N, Ansan V (2006) Detailed study of an hydrological system of valleys, a delta and lakes in Thaumasia region, Mars. Icarus 180:75–87
Mangold N et al (2007) Mineralogy of the Nili Fossae region with OMEGA/MEx data: 2. Aqueous alteration of the crust. J Geophys Res 112:E08S04
Mangold N, Ansan V, Masson P, Quantin C, Neukum G (2008a) Geomorphic study of fluvial landforms on the northern Valles Marineris plateau. Mars. J Geophys Res 113:E08009. doi:10.1029/2007JE002985
Mangold N et al (2008b) Spectral and geological study of the sulfate rich region of West Candor Chasma, Mars. Icarus 194:519–543
Mangold N et al (2010a) Mineralogy of recent volcanic plains in the Tharsis region, Mars, and implications for platy-ridged flow composition. Earth Planet Sci Lett. doi:10.1016/j.epsl.2009.07.036
Mangold N, Mangeney A, Migeon V, Ansan V, Lucas A, Baratoux D, Bouchut F (2010b) Sinuous gullies on Mars: frequency, distribution, and implications for flow properties. J Geophys Res 115:E11001. doi:10.1029/2009JE003540
Mangold N, Adeli S, Conway S, Ansan V, Langlais B (2012a) A chronology of early Mars climatic evolution from impact crater degradation. J Geophys Res Planets 117: doi:10.1029/2011JE004005
Mangold N et al (2012b) The origin and timing of fluvial activity at the Eberswalde crater, Mars. Icarus 220:530–551
Mangold N, Howard AD (2013) Outflow channels with deltaic deposits in Ismenius Lacus. Icarus, Mars. doi:10.1016/j.icarus.2013.05.040
Martin TZ (1981) Mean thermal and albedo behavior of the Mars surface and atmosphere over a Martian year. Icarus 45:427–446
Martin-Torres, FJ et al. (2015a) Highlights on the Rover Environmental Monitoring Station (REMS) on board the Mars Science Laboratory: new windows for atmospheric research on Mars. In: Forget F, Millour M (ed) The fifth international workshop on the Mars atmosphere: modelling and observation, id. 1103, Oxford, U.K
Martín-Torres FJ et al (2015b) Transient liquid water and water activity at Gale crater on Mars. Nat Geosci 8:357–361
Marzo G et al (2010) Evidence for hydrothermal impact-induced hydrothermalism on Mars. Icarus 208:667–683
Massé et al (2008) Mineralogical composition, structure, morphology, and geological history of Aram Chaos crater fill on Mars derived from OMEGA Mars Express data. J Geophys Res 113:E12
Massé M, Bourgeois O, Le Mouélic S, Verpoorter C, Le Deit L, Bibring J-P (2010) Martian polar and circum-polar sulfate-bearing deposits: sublimation tills derived from the North Polar Cap. Icarus. doi:10.1016/j.icarus.2010.04.017
Massé M et al (2016) Transport processes induced by metastable boiling water under martian surface conditions. Nat Geosci 9:425–428
Masson P (1977) Structure pattern analysis of the Noctis Labyrinthus-Valles Marineris regions of Mars. Icarus 30:49–62. doi:10.1016/0019-1035(77)90120-8
Matsuyama I, Manga M (2010) Mars without the equilibrium rotational figure, Tharsis, and the remnant rotational figure. J Geophys Res 115:E12020
Matta M, Mendillo M, Withers P, Morgan D (2015) Interpreting Mars ionospheric anomalies over crustal magnetic field regions using a 2-D ionospheric model. J Geophys Res Space Phys 120:766–777
McCleese DJ, Schofield JT, Taylor FW (2007) Mars climate sounder: an investigation of thermal and water vapor structure, dust and condensate distributions in the atmosphere, and energy balance of the polar regions. J Geophys Res 112:E05S06
McCleese DJ, Schofield JT, Taylor FW et al (2008) Intense polar temperature inversion in the middle atmosphere on Mars. Nat Geosci 1:745–749
McElroy MB, Donahue TM (1972) Stability of the Martian atmosphere. Science 177:986–988

McElroy MB, Kong TY, Yung YL, Nier AO (1976) Composition and structure of the Martian upper atmosphere–analysis of results from Viking. Science 194:1295–1298
McEwen et al (2011) Seasonal flows on warm martian slopes. Science 333:740–743
McGovern PJ, Solomon SC, Smith DE, Zuber MT, Simons M, Wieczorek MA, Phillips RJ, Neumann GA, Aharonson O, Head JW (2002) Localized gravity/topography admittance and correlation spectra on Mars: implications for regional and global evolution. J Geophys Res 107(E12):5136
McKay D et al (1996) Search for past life on Mars : Possible relic biogenic activity in Martian meteorite ALH84001. Science 273:924–930
McKeown NK et al (2009) Characterization of phyllosilicates observed in the central Mawrth Vallis region, Mars, their potential formational processes, and implications for past climate. J Geophys Res 114:E00D10. doi:10.1029/2008JE003301
McLennan SM et al (2014) Elemental geochemistry of sedimentary rocks in Yellowknife Bay, Gale Crater. Mars. Science 343: doi:10.1126/science.1244734
McSween HY et al (2006) Characterization and petrologic interpretation of olivine-rich basalts at Gusev Crater. Mars. J Geophys Res 111:E02S10
McSween HY, Taylor GJ, Wyatt MB (2009) Elemental composition of the Martian crust. Science 324:736–739
Médard E, Grove TL (2006) Early hydrous melting and degassing of the Martian interior. J Geophys Res 111:E11003
Mège D, Masson P (1996) Amounts of crustal stretching in Valles Marineris, Mars. Planet Space Sci 44:749–781. doi:10.1016/0032-0633(96)00013-X
Mège D, Bourgeois O (2011) Equatorial glaciations on Mars revealed by gravitational collapse of valles Marineris wallslopes. Earth Planet Sci Let 310:182–191
Melchiorri R et al (2006) A simulation of the OMEGA/Mars Express observations: analysis of the atmospheric contribution. Planet Space Sci 54:774–783
Mellon MT, Jakosky BM (1993) Geographic variations in the thermal and diffusive stability of ground ice on Mars. J Geophys Res Planets 98:3345–3364
Mellon MT (1997) Small-scale polygonal features on Mars: seasonal thermal contraction cracks in permafrost. J Geophys Res 102:25617–25628
Mellon MT, Feldman WC, Prettyman TH (2004) The presence and stability of ground ice in the southern hemisphere of Mars. Icarus 169:324–340
Mellon MT et al (2009) Ground ice at the Phoenix landing site: stability state and origin. J Geophys Res 114:E00E07. doi:10.1029/2009JE003417
Melosh HJ, Vickery AM (1989) Impact erosion of the primordial atmosphere of Mars. Nature 338:487–489
Mendillo M et al (2006) Effects of solar flares on the ionosphere of Mars. Science 311:1135–1138
Meresse S, Costard F, Mangold N, Baratoux D, Boyce JM (2006) Martian perched craters and large ejecta volume: evidence of episodes of deflation of the northern lowlands. Meteorit Planet Sci 41:147–1658
Merlivat L, Nief G (1967) Fractionnement isotopique lors des changementns d'état solide-vapeur et liquid-vapeur de l'eau à des temperatures inférieures à 0° Celsius. Tellus 19:122–127
Mezger K, Debaille V, Kleine Y (2012) Core formation and mantle differentiation on Mars. Space Sci Rev 174(1):27–48
Michalski JR, Niles PB (2010) Deep crustal carbonate rocks exposed by meteor impact on Mars. Nat Geosci 3:751–755. doi:10.1038/ngeo971
Michalski JR, Cuadros J, Niles PB, Parnell J, Rogers AD, Wright SP (2013) Groundwater activity on Mars and implications for a deep biosphere. Nat Geosci 6:133–138. doi:10.1038/ngeo1706
Milbury CAE, Schubert G (2010) Search for the global signature of the Martian dynamo. J Geophys Res 115: doi:10.1029/2010JE003617
Milton DJ (1973) Water and processes of degradation in the Martian landscape. J Geophys Res 78:4037–4047
Milliken RE, Grotzinger JP, Thomson BJ (2010) Paleoclimate of Mars as captured by the stratigraphic record in Gale Crater. Geophys Res Lett 37:L04201. doi:10.1029/2009GL041870
Milliken RE, Bish DL (2010) Sources and sinks of clay minerals on Mars. Philos Mag 90:2293–2308. doi:10.1080/14786430903575132
Molina-Cuberos GJ, Witassec O, Lebreton J-P, Rodrigo R, López-Moreno JJ (2003) Meteoric ions in the atmosphere of Mars. Planet Space Sci 51(3):239–249. doi:10.1016/S0032-0633(02)00197-6
Montmessin F, Forget F, Rannous P et al (2004) Origin and role of water ice clouds in the Martian water cycle as inferred from a general circulation model. J Geophys Res 109:E10004

Montmessin F, Fouchet T, Forget F (2005) Modeling the annual cycle of HDO in the Martian atmosphere. J Geophys Res 110:E03006
Monteux J, Jellinek AM, Johnson CL (2013) Dynamics of core merging after a mega-impact with applications to Mars' early dynamo. Icarus 226:20–32
Monteux J, Arkani-Hamed J (2014) Consequences of giant impacts in early Mars: core merging and Martian dynamo evolution. J Geophys Res Planets 119:480–505. doi:10.1002/2013JE004587
Moore JM, Howard AD (2005) Large alluvial fans on Mars. J Geophys Res 110:E04005. doi:10.1029/2004JE002352
Morschhauser A, Grott M, Breuer D (2011) Crustal recycling, mantle dehydration, and the thermal evolution of Mars. Icarus 212:541–558
Moreno F et al (2009) Wind measurements in Mars' middle atmosphere: IRAM Plateau de Bure interferometric CO observations. Icarus 201:549–563
Morgan D et al (2010) Radar absorption due to a corotating interaction region encounter with Mars detected by MARSIS. Icarus 206:95–103
Morgan D et al (2013) The processing of electron density profiles from the Mars Express MARSIS topside sounder. Radio Sci 48:197–207
Morgan D et al (2014) Effects of a strong ICME on the Martian ionosphere as detected by Mars Express and Mars Odyssey. J Geophys Res Space Phys 119:5891–5908
Morris RV et al (2010b) Identification of carbonate-rich outcrops on Mars by the Spirit Rover. Science 329:421–424. doi:10.1126/science.1189667
Mouginis-Mark PJ (1979) Martian fluidized crater morphology: variations with crater size, latitude, altitude and target material. J Geophys Res 84:8011–8022
Mouginis-Mark PJ, Baloga SM (2006) Morphology and geometry of the distal ramparts of Martian impact craters. Meteorit Planet Sci 41:1469–1482
Mouginot J, Kofman W, Safaeinili A, Herique A (2008) Correction of the ionospheric distortion on the MARSIS surface sounding echoes. Planet Space Sci 56:917–926
Mouginot J et al (2010) The 3–5 MHz global reflectivity map of Mars by MARSIS/Mars Express: implications for the current inventory of subsurface H_2O. Icarus 210:612–625
Mouginot J, Pommerol A, Beck P et al (2012) Dielectric map of the Martian northern hemisphere and the nature of plain filling materials. Geophys Res Lett 39:L02202
Mousis O et al (2013) Volatile trapping in Martian clathrates. Space Sci Rev 174:213–250
Mumma MJ, Novak RE, DiSanti MA et al (2004) Detection and mapping of methane and water on Mars. In: AAS-DPS annual conference, BAAS, vol 36, p 1127
Mumma MJ et al (2009) Strong release of methane on Mars in northern summer 2003. Science 323:1041–1044
Musselwhite DS, Dalton HA, Kiefer WS, Treiman AH (2006) Experimental petrology of the basaltic shergottite Yamato-980459: implications for the thermal structure of the Martian mantle. Meteorit Planet Sci 41:1271–1290
Mustard JF, Poulet F, Bibring JP, Langevin Y, Gondet B, Mangold N, Belluci G, Altieri F (2005) Olivine and pyroxene diversity in the curst of Mars. Science 307(5515):1595–1597
Mustard JF et al (2008) Hydrated silicate minerals on Mars. Nature 454:305–309
Murchie SM et al (2009) A synthesis of Martian aqueous mineralogy after one Mars year of observations from the Mars Reconnaissance Orbiter. J Geophys Res 114:E00D06. doi:10.1029/2009JE003342
Nachon M et al (2014) Calcium sulfate veins characterized by the ChemCam instrument at Gale Crater. Mars. J Geophys Res 119(9):1991–2016. doi:10.1002/2013JE004588
Nagy AF, Gregobowsky JM (2015) Current understanding of the aeronomy of Mars. Geosci Lett 2:5
Nahm AL, Schultz SR (2010) Magnitude of global contraction on Mars from analysis of surface faults: implications for martian thermal history. Icarus 211:389–400
Navarro T, Madeleine J-B, Forget F et al (2014) Global climate modeling of the Martian water cycle with improved microphysics and radiatively active water ice clouds. J Geophys Res 119:1479–1495
Nedell SS, Squyres SW, Andersen DW (1987) Origin and evolution of the layered deposits in the Valles Marineris, Mars. Icarus 70:409–441
Neukum G et al (2004) Recent and episodic volcanic and glacial activity on Mars revealed by the High Resolution Stereo Camera. Nature 432:971–979
Nier AO, McElroy MB (1977) Composition and structure of Mars' upper atmosphere–results from the neutral mass spectrometers on Viking 1 and 2. J Geophys Res 82:4341–4349

Nier AO, Hanson WB, Seiff A et al (1976) Composition and structure of the Martian atmosphere–preliminary results from Viking 1. Science 193:786–788
Nimmo F (2000) Dike intrusion as a possible cause of linear martian magnetic anomalies. Geology 28:391–394
Nimmo F, Kleine T (2007) How rapidly did Mars accrete? Uncertainties in the HF-W timing for core formation. Icarus 191:497–504
Nimmo F, Stevenson DJ (2001) Estimates of Martian crustal thickness from viscous relaxation of topography. J Geophys Res 106:5085–5098
Nimmo F, Tanaka K (2005) Early crustal evolution of Mars. Annu Rev Earth Planet Sci 33:133–161. doi:10.1146/annurev.earth.33.092203.122637
Norman MD (1999) The composition and thickness of the crust of Mars estimated from rare earth elements and neodymium isotopic compositions of Martian meteorites. Meteorit Planet Sci 34:439–449
Novak RE, Mumma MJ, Villanueva GL (2011) Measurement of the isotopic signatures of water on Mars: Implications for studying mlethane. Planet Space Sci 59:163–168
Oehler D, Allen CC (2012) Giant polygons and mounds in the lowlands of Mars: signatures of an ancient ocean? Astrobiology 12:601–615
Ody A, Poulet F, Bibring J-P, Loizeau D, Carter J, Gondet B, Langevin Y (2013) Global investigation of olivine on Mars: insights into crust and mantle compositions. J Geophys Res Planets 118:234–262
Ojha LA et al (2015) HiRISE observations of recurring slope lineae (RSL) during southern summer on Mars. doi:10.1016/j.icarus.2013.12.021
Opgenoorth H et al (2013) Mars ionospheric response to solar wind variability. J Geophys Res Space Phys 118(10):6558–6587
Orosei R et al (2015) Mars Advanced Radar for Subsurface and Ionospheric Sounding (MARSIS) after nine years of operation: A summary. Planet Space Sci 112:98–114
Owen T (1992) The composition and early history of the atmosphere of Mars. In: Kieffer HH et al (eds) Mars. University of Arizona Press, Tucson
Owen T, Bar-Nun A (1995) Comets, impacts, and atmospheres. Icarus 116:215–226
Owen T, Biemann K, Biller JE et al (1977) The composition of the atmosphere at the surface of Mars. J Geophys Res 82:4635–4639
Owen T, Maillard J-P, de Bergh C, Lutz BL (1988) Deuterium on Mars–the abundance of HDO and the value of D/H. Science 240:1767–1770
Oyama VI, Berdahl BJ (1977) Preliminary findings of the Viking gas exchange experiment and a model for Martian surface chemistry. Nature 265:110–114
Paige DA, Herkenhoff KE, Murray BC (1990) Mariner-9 observations of the south polar-cap of Mars–evidence for residual CO_2 frost. J Geophys Res 95:1319–1335
Paige DA, Wood SE (1991) Modeling the martian seasonal CO_2 cycle. Icarus 99:15–27
Pan C, Rogers AD, Michalski JR (2015) Thermal and near-infrared analyses of central peaks of Martian impact craters: evidence for a heterogeneous Martian crust. J Geophys Res Planets 120:662–688
Parkinson TD, Hunten DM (1972) Spectroscopy and aeronomy of O_2 on Mars. J Atmos Sci 29:1380–1390
Parker TJ, Gorsline DS, Saunders RS, Pieri DC, Schneeberger DM (1993) Coastal geomorphology of the martian northern plains. J Geophys Res 98:11061–11078
Pätzold M et al (2005) A sporadic third layer in the ionosphere of Mars. Science 310(5749):837–839
Pätzold M et al (2009) The structure of the lower Mars ionosphere. In: European Planetary Science Congress, Postdam, Germany
Paxton LJ, Vervack RJ (2001) The hot atom Coronae of Venus, Mars and the Earth: current understanding and challenges. American Geophysical Union Fall Meeting 2001, abstract #SA51A-0775
Pepin RO (1994) Evolution of the Martian atmosphere. Icarus 111(2):289–304
Pepin RO, Schlutter J, Becker RH, Reisenfeld DB (2012) Helium, neon and argon composition of the solar wond as recorded in gold and other Genesis collector materials. Geochim Cosmochim Acta 89:62–80
Perrier S et al (2006) Global distribution of total ozone on Mars from SPICAM/MEX UV measurements. J Geophys Res 111:E09S06
Perron JT, Mitrovica JX, Manga M, Matsuyama I, Richards MA (2007) Evidence for an ancient martian ocean in the topography of deformed shorelines. Nature 447:840–843
Peter K et al (2014) The dayside ionospheres of Mars and Venus: comparing a one-dimensional photochemical model with MaRS (Mars Express) and VeRa (Venus Express) observations. Icarus 233:66–82
Pesnell WD, Grebowsky JM (2000) Meteoric magnesium ions in the Martian atmosphere. J Geophys Res 105:1695–1707

Phillips RJ et al (2008) Mars north polar deposits: stratigraphy, age, and geodynamical response. Science 320(5880):1182–1185
Phillips RJ et al (2001) Ancient geodynamics and global-scale hydrology on Mars. Science 291:2587–2591
Phillips RJ et al (2011) Massive CO_2 ice deposits sequestered in the south polar layered deposits of Mars. Science 332:838–841
Picardi G et al (2005) Radar soundings of the subsurface of Mars. Science 310(5756):1925–1928
Piqueux SS, Byrne PK, Richardson MI (2003) Sublimation of Mars's southern seasonal CO_2 ice cap and the formation of spiders. J Geophys Res 108(E8):5084
Piqueux S, Christensen PR (2008) North and south sub-ice gas flow and venting of the seasonal caps of Mars: a major geomorphological agent. J Geophys Res 113:E06005
Pilorget C, Forget F, Millour E, Vincendon M, Madeleine JB (2011) Dark spots and cold jets in the polar regions of Mars: new clues from a thermal model of surface CO_2 ice. Icarus 213:131–149
Pilorget C, Forget F (2016) Formation of gullies on Mars by debris flows triggered by CO_2 sublimation. Nat Geosci 9:65–69
Platz T, Michael G (2011) Eruption history of the Elysium volcanic province, Mars. Earth Plan Sci Lett 312:140–151
Plaut JJ, Frigeri A, Orosei R (2012) Compositional constraints on the Martian North Polar Basal Unit from MARSIS radar sounding data. In: Lunar and planetary science conference, vol 43, The Woodlands, Texas, abstract# 2458
Plaut JJ et al (2009) Radar evidence for ice in lobate debris aprons in the mid-northern latitudes of Mars. Geophys Res Lett 36:L02203
Plescia J (1990) Recent flood lavas in the Elysium regions of Mars. Icarus 88:465–490
Plescia JB (2004) Morphometric properties of Martian volcanoes. J Geophys Res 109:E03003
Poulet F et al (2008) Spectral variability of the Martian high latitude surfaces. Geophys Res Lett 35:L20201
Poulet F et al (2005) Phyllosilicates on Mars and implications for the early Mars history. Nature 438:623–628
Prieto-Ballesteros O et al (2006) Interglacial clathrate destabilization on Mars: possible contributing source of its atmospheric methane. Geology 34:149–152
Purucker M et al (2000) An altitude normalized magnetic map of Mars and its interpretation. Geophys Res Lett 27:2449–2452
Quantin C, Allemand P, Mangold N, Dromart G, Delacourt C (2005) Fluvial and lacustrine activity on layered deposits in Melas Chasma, Valles Marineris. Mars. J Geophys Res 110(E12):E12S19
Quantin C, Flahaut J, Clenet H, Allemand P, Thomas P (2012) Composition and structure of the subsurface in the vicinity of Valles Marineris as revealed by central uplift of impacts craters. Icarus 221(1):436–452
Quesnel Y et al (2009) Serpentinization of the martian crust during Noachian. Earth Planet Sci Lett 277:184–193
Ramstad R et al (2015) The Martian atmospheric ion escape rate dependence on solar wind and solar EUV conditions I: seven years of Mars Express observations. J Geophys Res Planets 120:1298–1309
Restano M et al (2015) Effects of the passage of Comet C/2013 A1 (Siding Spring) observed by the Shallow Radar (SHARAD) on Mars Reconnaissance Orbiter. Geophys Res Lett 42:4663–4669
Richardson MI, Wilson RJ (2002) Investigation of the nature and stability of the Martian seasonal water cycle with a general circulation model. J Geophys Res 107:E5
Rieder R et al (1997) Determination of the chemical composition of Martian soil and rocks: APXS. J Geophys res 102:4027–4044
Rivoldini A, Van Hoolst T, Verhoeven O, Mocquet A, Dehant V (2011) Geodesy constraints on the interior structure of Mars. Icarus 213(2):451–472
Roberts JH, Zhong S (2006) Degree-1 convection in the martian mantle and the origin of the hemispheric dichotomy. J Geophys Res 111:E06013
Rochette P, Lorand J-P, Fillion G, Sautter V (2001) Pyrrhotite and the remanent magnetization of SNC meteorites: a changing perspective on martian magnetism. Earth Planet Sci Lett 190:1–12
Rodriguez JAP et al (2005) Outflow channel sources, reactivation, and chaos formation, Xanthe Terra, Mars. Icarus 175:36–57
Rodriguez JAP et al (2015) Martian outflow channels: how did their source aquifers form, and why did they drain so rapidly? Sci Rep 5:13404
Rodriguez JP et al (2016) Tsunami waves extensively resurfaced the shorelines of an early Martian ocean. Nature Scientific Reports 6:25106
Rogers AD, Fergason RL (2011) Regional-scale stratigraphy of surface units in Tyrrhena and Iapygia Terrae, Mars: insights into highland crustal evolution and alteration history. J Geophys Res 116:E08005

Rosenqvist J, Chassefière E (1995) A reexamination of the relationship between eddy mixing and O_2 in the Martian middle atmosphere. J Geophys Res 100:5541–5551
Rubie DC et al (2007) Formation of the Earth's core. In: Treatise of geophysics, vol 9. Elsevier, pp 51–90
Ruff SW et al (2011) Characteristics, distribution, origin and significance of opaline silica observed by the Spirit rover in Gusev crater. Mars. J Geophys Res 116:E00F23
Ruiz J et al (2008) Ancient heat flow, crustal thickness, and lithospheric mantle rheology in the Amenthes region, Mars. Earth Planet Sci Lett 270:1–12
Ruiz J, Williams JP, Dohm J, Fernández C, López V (2009) Ancient heat flow and crustal thickness at Warrego rise, Thaumasia highlands, Mars: implications for a stratified crust. Icarus 203:47–57
Ruiz J et al (2011) The thermal evolution of Mars as constrained by paleo-heat flows. Icarus 215:508–517
Safaeinili A et al (2007) Impact of Mars ionosphere on orbital radar sounder operation and data processing. Planet Space Sci 51(7–8):505–515
Salvatore MR, Mustard JF, Wyatt MB, Murchie SL (2010) Definitive evidence of Hesperian basalt in Acidalia and Chryse planitiae. J Geophys Res 115:E07005
Sanchez-Cano B et al (2015) Evidence of scale height variations in the Martian ionosphere over the solar cycle. J Geophys Res (Space Phys) 120(12):10,913–10,925
Sánchez-Lavega A et al (2015) An extremely high-altitude plume seen at Mars' morning terminator. Nature 518(7540):525–528
Sandel B et al (2015) Altitude profiles of O_2 on Mars from SPICAM stellar occultations. Icarus 252:154–160
Sanloup CA, Jambon A, Gillet P (1999) A simple chondritic model of Mars. Phys Earth Planet Int 112:43–54
Sautter V et al (2014) Igneous mineralogy at Bradbury Rise: the first ChemCam campaign at Gale crater. J Geophys Res 119:30–46
Sautter V et al (2015) In situ evidence for continental crust on early Mars. Nat Geosci 8:605–609
Sautter V et al (2016) Magmatic complexity on early Mars as seen through a combination of orbital, in-situ and meteorite data. Lithos 254–255:36–52
Schmidt ME et al (2014) Geochemical diversity in first rocks examined by the Curiosity Rover in Gale Crater: evidence for and significance of an alkali and volatile-rich igneous source. J Geophys Res 119:64–81
Schneider NM et al (2015) Discovery of diffuse aurora on Mars. Science 350(6261):
Schneider NM et al (2015) MAVEN IUVS observations of the aftermath of the Comet Siding Spring meteor shower on Mars. Geophys Res Lett 42:4755–4761
Schultz PH, Gault DE (1979) Atmospheric effects on martian ejecta emplacement. J Geophys Res 84:7669–7687
Schultz RA (1998) Multiple-process origin of Valles Marineris basins and troughs. Planet Space Sci 46:827–834
Schultz RA (2000) Localization of bedding-plane slip and backthrust faults above blind thrust faults: keys to wrinkle ridge structure. J Geophys Res 105:12,035–12,052
Schultz RA, Watters TR (2001) Forward mechanical modeling of the Amenthes Rupes thrust fault on Mars. Geophys Res Lett 28(24):4659–4662
Schumacher S, Breuer D (2007) An alternative mechanism for recent volcanism on Mars. Geophys Res Lett 34:L14202
Schunk R, Nagy F (2009) Ionospheres, 2nd edn. Cambridge University Press, Cambridge, p 628
Schwenzer SP, Kring DA (2009) Impact-generated hydrothermal systems capable of forming phyllosilicates on Noachian Mars. Geology 37:1091–1094
Sefton-Nash E, Catling DC, Wood SE, Grindrod PM, Teanby NA (2012) Topographic, spectral and thermal inertia analysis of interior layered deposits in Iani Chaos, Mars. Icarus 221:20–42
Seibert NM, Kargel JS (2001) Small-scale martian polygonal terrain: implications for liquid surface water. Geophys Res Lett 28(5):899–902
Seiff A (1982) Post-Viking models for the structure of the summer atmosphere of Mars. Adv. Space Res. 2:3–17
Séjourné et al (2011) Scalloped depressions and small-sized polygons in western Utopia Planitia, Mars: a new formation hypothesis. Planet Space Sci 59:412–422
Selvans MM, Plaut JJ, Aharonson O, Salfaeinili A (2010) Internal structure of Planum Boreum, from Mars advanced radar for subsurface and ionospheric sounding data. J Geophys Res 115:E09003
Shahnas H, Arkani-Hamed J (2007) Viscous and impact demagnetization of Martian crust. J Geophys Res 112:E02009

Shaheen R et al (2015) Carbonate formation events in ALH84001 trace the evolution of the martian atmosphere. 112(2):336–341
Simon C, Witasse O, Leblanc F, Gronoff G, Bertaux J-L (2009) Dayglow on Mars: kinetic modelling with SPICAM UV limb data. Planet Space Sci 57(8–9):1008–1021
Sizemore HG (2010) In situ analysis of ice table depth variations in the vicinity of small rocks at the Phoenix landing site. J Geophys Res 115:E00E09
Skok JR et al (2010) Silica deposits in the Nili Patera caldera on the Syrtis Major volcanic complex on Mars. Nat Geosci 3:838–841
Sleep NH (1994) Martian plate tectonics. J Geophys Res 99(E3):5639–5655
Smith JV et al (1970) Petrologic history of the Moon inferred from petrography, mineralogy, and petrogenesis of Apollo 11 rocks. In: Proceedings of the Apollo 11 lunar science conference. Pergamon Press, pp 897–925
Smith MD (2002) The annual cycle of water vapor on Mars as observed by the Thermal Emission Spectrometer. J Geophys Res 107:5115
Smith MJ (2004) Interannual variability in TES atmospheric observations of Mars during 1999–2003. Icarus 167:148–165
Smith MD et al (2009) Compact reconnaissance imaging spectrometer observations of water vapor and carbon monoxide. J Geophys Res 114:E00D03
Smith MD, Bougher S, Encrenaz T, Forget F, Kleinböhl A (2016) Thermal structure and composition. In: Haberle RM (ed) The Mars atmosphere and climate book. Cambridge University Press (in press)
Soare RJ, Osinksi GR, Roehm RL (2008) Themokarst lakes and ponds on Mars in the very recent (late Amazonian) past. Earth Planet Sci Lett 272(1–2):382–393
Sohl F, Spohn T (1997) The interior structure of Mars: implications from SNC meteorites. J Geophys Res 102:1613–1635
Sohl F, Schubert G, Spohn T (2005) Geophysical constraints on the composition and structure of the Martian interior. J Geophys Res 110:E12008
Solomatov VS (2000) Fluid dynamics of a terrestrial magma ocean. In: Canup RM, Righter K (eds) Origin of the Earth and Moon. University of Arizona Press, Tucson, pp 323–338
Spinrad H, Richardson EH (1963) High dispersion spectra of the outer planets. II. A new upper limit for the water vapor content of the Martian atmosphere. Icarus 2:49–53
Spohn et al (2000) Geophysical constraints of the evolution of Mars. Space Sci Rev 96:231–262
Sprague AL et al (1996) Martian water vapor, 1988–1995. J Geophys Res 101:23,229–23,254
Sprague AL et al (2006) Mars atmospheric water vapor abundance: 1991–1999, emphasis 1998–1999. Icarus 184:372–400
Squyres SW (1978) Martian fretted terrain: flow of erosional debris. Icarus 34:600–613
Squyres SW, Carr MH (1986) Geomorphic evidence for the distribution of ground ice on Mars. Science 231:249–252
Squyres SW, Kasting JF (1994) Early Mars: how warm and how wet? Science 265:744–749
Squyres SW et al (2004) The opportunity rover's Athena Science inverstigation at Meridiani Planum. Mars. Science 306(5702):1698–1703
Squyres SW, Knoll AH (2005) Sedimentary rocks at Meridiani Planum: origin, diagenesis, and implications for life on Mars. Earth Planet Sci Lett 240:1–10
Squyres SW et al (2006) Overview of the Opportunity Mars Exploration Rover mission to Meridiani Planum: Eagle Crater to purgatory ripple. J Geophys Res (Planets) 111:E12S12
Squyres SW et al (2012) Ancient impact and aqueous processes at Endeavour crater. Mars. Science 336(6081):570–576
Stepinski TF, Stepinski AP (2005) Morphology of drainage basins as an indicator of climate on early Mars. J Geophys Res 110:E12S12
Stewart AI (1972) Mariner 6 and 7 ultraviolet spectrometer experiment: implications of CO^{2+}, CO and O airglow. J Geophys Res 77(1):54
Stack KM, Grotzinger JP, Milliken RE (2013) Bed thickness distributions on Mars: an orbital perspective. J Geophys Res Planets 118:1323–1349
Stock JW et al (2011) Analyzing O_2 and O_3 production and destruction pathways in the martian atmosphere. European planetary science conference, Nantes, France
Stolper EM et al (2013) The Petrochemistry of Jake_M: A Martian Mugearite. Science 341: doi:10.1126/science.1239463

Sullivan R, Thomas P, Veverka J, Malin M, Edgett K (2001) Mass movement slope streaks imaged by the Mars Orbiter Camera. J Geophys Res 106(E10):23607–23633

Sun VZ, Milliken RE (2014) The geology and mineralogy of Ritchey crater, Mars: evidence for post-Noachian clay formation. J Geophys Res 119:810–836

Tanaka KL (1986) The stratigraphy of Mars. Proceedings of the 17th lunar planet science conference, part 1. J Geophys Res 91(suppl.):E139–E158

Tanaka KL, Golombek MP, Banerdt WB (1991) Reconciliation of stress and structural histories of the Tharsis region of Mars. J Geophys Res 96:15,617–15,633

Tanaka KL et al (2014) The digital geologic map of Mars: Chronostratigraphic ages, topographic and crater morphologic characteristics and updated resurfacing history. Planet Space Sci 95:11–24

Thollot P et al (2012) Most Mars minerals in a nutshell: various alteration phases formed in a single environment in Noctis Labyrinthus. J Geophys Res Planets 117:E00J06

Thomas N, Hansen CJ, Portyankina G, Russell PS (2010) HiRISE observations of gas sublimation-driven activity in Mars' southern polar regions: II. Surficial deposits and their origins. Icarus 205:296–310

Tillman JE, Johnson NC, Guttorp P, Percival DB (1993) The Martian annual atmospheric pressure cycle–years without great dust storms. J Geophys Res 98:10963–10971

Tonks WB, Melosh HJ (1993) Magma ocean formation due to giant impacts. J Geophys Res (Planets) 98:5319–5333

Tosi N, Plesa AC, Breuer D (2013) Overturn and evolution of a crystallized magma ocean: a numerical parameter study for Mars. J Geophys Res Planets 118:1–17

Touboul M, Kleine T, Bourdon B, Palme H, Wieler R (2007) Late formation and prolonged differentiation of the Moon inferred from W isotopes in lunar metals. Nature 450:1206–1209

Treiman AH, Drake MJ, Janssens M-J, Wolf R, Ebihara M (1986) Core formation in the Earth and shergottite parent body (SPB): chemical evidence from basalts. Geochim Cosmochim Acta 50:1071–1091

Tschimmel M et al (2008) Investigation of water vapor on Mars with PFS/SW of Mars Express. Icarus 195:557–575

Tuff J, Wade J, Wood BJ (2013) Volcanism on Mars controlled by early oxidation of the upper mantle. Nature 498:342–345

Turcotte DL, Schubert G (1988) Tectonic implications of radiogenic noble gases in planetary atmospheres. Icarus 74:36–46

Usui et al (2012) Origin of water and mantle-crust interactions on Mars inferred from hydrogen isotopes and volatile element abundances of olivine-hosted melt inclusions of primitive shergottites. Earth Planet Sci Letters 357:119–129

Vago JL et al (2015) ESA ExoMars program: the next step in exploring Mars. Sol Syst Res 49:518–528

Valeille A et al (2009) Three-dimensional study of Mars upper thermosphere/ionosphere and hot oxygen corona: 2. Solar cycle, seasonal variations and evolution over history. J Geophys Res 114:E11006

Vaucher J, Baratoux D, Mangold N, Pinet P, Kurita K, Grégoire M (2009) The volcanic history of central Elysium Planitia: implications for martian magmatism. Icarus 204:418–442

Villanueva GL, Mumma MJ, Novak RE (2013) A sensitive search for organics (CH_4, CH_3OH, H_2CO, C_2H_6, C_2H_2, C_2H_4), hydroperoxyl (HO_2), nitrogen compounds (N_2O, NH_3, HCN) and chlorine species (HCl, CH3Cl) on Mars using ground-based high-resolution infrared spectroscopy. Icarus 223:11–27

Villanueva GL et al (2015) Strong water isotopic anomalies in the martian atmosphere: probing current and ancient reservoirs. Science 348:218–221

Viviano CE, Moersch JE, McSween HY (2013) Implications for early hydrothermal environments on Mars through the spectral evidence for carbonation and chloritization reactions in the Nili Fossae region. J Geophys Res (Planets) 118:1858–1872

Viviano-Beck CE (2015) Early hydrothermal environments on Mars: Tyrrhena Terra. In: 46th Lunar planetary science conference, The Woodlands, TX, UDA. Abstract #2756

Walker D, Longhi J, Hays JF (1975) Differentiation of a very thick magma body and implications for the source region of mare basalts. 6th Lunar science conference. Houston, TX, USA, pp 1103–1120

Walker RJ (2009) Highly siderophile elements in the Earth, Moon and Mars: update and implications for planetary accretion and differentiation. Chemie der Erde Geochemistry 69:101–125

Walsh KJ, Morbidelli A, Raymond SN, O'Brien DP, Mandell AM (2011) A low mass for Mars from Jupiter's early gas-driven migration. Nature 475:206–209

Wang J-S, Nielsen E (2003) Behavior of the Martian dayside electron density peak during global dust storms. Planet Space Sci 51(4–5):329–338

Wang YC et al (2016) Cometary sputtering of the Martian atmosphere during the Siding Spring encounter. Icarus 272:301–308
Watters TR (1993) Compressional tectonism on Mars. J Geophys Res 98:17049–17060
Watters TR (2003) Thrust faults along the dichotomy boundary in the eastern hemisphere of Mars. J Geophys Res 108(E6):5054
Webster CR et al (2013) Measurements of Mars methane at Gale Crater by the SAM tunable laser spectrometer on the Curiosity Rover. In: 44th Lunar planetary science conference, The Woodlands, TX, USA, abstract #1366
Webster CR et al (2015) Mars methane detection and variability at Gale crater. Science 347:415–417
Weiss BP, Elkins-Tanton LT (2013) Differentiated planetesimals and the parent bodies of chondrites. Annu Rev Earth Planet Sci 41:529–560
Weitz CM, Bishop JL, Thollot P, Mangold N, Roach LH (2011) Diverse mineralogies in two troughs of Noctis Labyrinthus, Mars. Geology 39:899–902
Werner SC (2008) The early martian evolution–constraints from basin formation ages. Icarus 195(1):45–60
Werner SC, Tanaka KL (2010) Redefinition of the crater-density and absolute-age boundaries for the chronostratigraphic system of Mars. Icarus 215:603–607
Wieczorek MA, Zuber MT (2004) Thickness of the Martian crust: improved constraints from geoid-to-topography ratios. J Geophys Res 109:E01009
Williams RME, Phillips RJ (2001) Morphometric measurements of martian valley networks from Mars Orbiter Laser Altimeter (MOLA) data. J Geophys Res 106(E10):23,737–23,751
Williams D et al (2009) The Circum-Hellas volcanic province, Mars: overview. Planet Space Sci 57:895–916
Williams RME et al (2013) Martian fluvial conglomerates at Gale Crater. Science 340:1068–1072
Wilhelms DE, Squyres SW (1984) The martian hemispheric dichotomy may be due to a giant impact. Nature 309:138–140
Wilson L, Head JW (1994) Review and analysis of volcanic-eruption theory and relationships to observed landforms. Review of Geophysics 32:221–263
Wilson SA, Howard AD, Moore JM, Grant JA (2007) Geomorphic and stratigraphic analysis of Crater Terby and layered deposits north of Hellas basin. Mars. J Geophys Res 112:E08009
Withers P et al (2012) A clear view of the multifaceted dayside ionosphere of Mars. Geophys Res Lett 39:L18202
Withers P, Pratt R (2013) An observational study of the response of the upper atmosphere of Mars to lower atmospheric dust storms. Icarus 225(1):378–389
Withers P et al (2013) Meteoric ion layers in the ionospheres of venus and mars: early observations and consideration of the role of meteor showers. Adv Space Res 52(7):1207–1216
Withers P (2014) Predictions of the effects of Mars's encounter with Comet C/2013 A1 (Siding Spring) upon metal species in its ionosphere. Geophys Res Lett 41:6635–6643
Wittmann A et al (2015) Petrography and composition of Martian regolith breccia meteorite Northwest Africa 7475. Meteorit Planet Sci 50:326–352
Wong M et al (2013) Isotopes of nitrogen on Mars : atmospheric measurements by Curiosity's mass spectrometer. Geophys Res Lett 40:6033–6037
Wood JA, Dickey JS, Marvin UB, Powell BN (1970) Lunar anorthosites and a geophysical model of the Moon. In: Proceedings of the Apollo 11 lunar science conference. Pergamon Press, pp 965–988
Wordsworth R, Forget F, Millour E, Head J, Madeleine J-B, Charnay B (2013) Global modelling of the early Martian climate under a denser CO_2 atmosphere: water cycle and ice evolution. Icarus 222:1–19
Wray et al (2008) Compositional stratigraphy of clay-bearing layered deposits at Mawrth Vallis. Mars. Geophys Res Lett 35:L12202
Wray JJ, Murchie SL, Squyres SW, Seelos FP, Tornabene LL (2009) Diverse aqueous environments on ancient Mars revealed in the southern highlands. Geology 37:1043–1046
Wray J et al (2013) Prolonged magmatic activity on Mars inferred from the detection of felsic rocks. Nat Geosci 6:1013–1018
Wray et al (2016) Orbital evidence for more widespread carbonate-bearing rocks on Mars. J Geophys Res 121:652–677
Xiao L, He Q et al (2012) Ancient volcanism and its implication for thermal evolution of Mars. Earth Planet Sci Lett 323–324:9–18
Yelle R, Mahieux A, Morrison S, Vuitton V, Hörst SM (2014) Perturbation of the Mars atmosphere by the near-collision with comet C/2013 A1 (Siding Spring). Icarus 237:202–210
Yoder et al (2003) Fluid core size of Mars from detection of the solar tide. Science 300:299–303

Yokoyama E, Nédélec A, Baratoux D, Trindade RIF, Fabre S, Berger G (2015) Hydrothermal alteration in the Vargeão impact structure (South Brazil): implications for recognition of impact-induced hydrothermalism on Mars. Icarus 252:347–365

Yung YL et al (1988) HDO in the Martian atmosphere–implications for the abundance of crustal water. Icarus 76:146–159

Yung-Ching W et al (2016) Cometary sputtering of the Martian atmosphere during the Siding Spring encounter. Icarus 272:301–308

Zahnle K, Freedman RS, Catlin D (2011) Is there methane on Mars? Icarus 412:493–503

Zharkov VN, Gudkova TV (2005) Construction of martian interior model. Sol Syst Res 39:387

Zhong S, Zuber MT (2001) Degree-1 mantle convection and the crustal dichotomy on Mars. Earth Planet Sci Lett 189:75–84

Zhong S (2009) Migration of Tharsis volcanism on Mars caused by differential rotation of the lithosphere. Nat Geosci 2:19–23

Zuber MT (2001) The crust and mantle of Mars. Nature 412:237–244

Zurek RW (1981) Inference of dust opacities for the 1977 Martian great dust storms from Viking Lander 1 pressure data. Icarus 45:202–215